Design and Teleoperative Control of Humanoid Robot Upper Body for Task-driven Assistance

MICHAEL ALEXANDER DONOVAN STEVENS

Thesis submitted to the faculty of the Virginia Polytechnic Institute and State University in partial fulfillment of the requirements for the degree of

Master of Science
In
Mechanical Engineering

Shashank Priya, Chair
Dennis W. Hong
Andrew J. Kurdila

April 29th, 2013
Blacksburg, Virginia

Keywords: Humanoid, Teleoperation, Kinect, Skeletal Control

Design and Teleoperative Control of Humanoid Robot Upper Body for Task-driven Assistance

Michael Alexander Donavan Stevens

ABSTRACT

Both civilian and defense industry rely heavily on robotics which continues to gain a more prominent role. To exemplify, defense strategies in Middle East have relied upon robotic drones and teleoperative assistant robots for mission oriented tasks. These operations have been crucial in saving the lives of soldiers and giving us the edge in mitigating disasters. Future assistive robotics will have direct human interaction and will reside in normal human environments. As the advancement in technology continues to occur, there will be a focus towards eliminating the direct human control and replacing it with higher level autonomy. Further, advancements in electronics and electromechanical components will reduce the cost and makes the assistive robotics accessible to the masses. This thesis focuses on robotic teleoperation technology and the future high level control of assistant robotics. A dexterous 16 degree of freedom hand with bend sensors for precise joint positions was designed, modeled, fabricated and characterized. The design features a unique motor actuation mechanism that was 3D printed to reduce the cost and increase the modularity. The upper body was designed to be biomimetic with dimensions similar to that of a typical six foot tall male. The upper body of the humanoid consists of a 4 degree of freedom shoulder and upper arm with direct feedback at each joint. A theoretical nonlinear switching controller was designed to control these 4 degrees of freedom. The entire system was teleoperative controlled with an Xbox Kinect that tracks the skeletal points of a user and emulates these 3D points to the joints of humanoid upper body. This allows for a direct user control over a robotic assistive upper body with nothing more than a human emulating the desired movements.

Acknowledgments

I would like to thank my peers, undergraduate students and importantly my advisor, Dr. Priya, for all the assistance I have received over the past few years. I would also like to thank my close friends and family for their understanding of my dedication to my education first over other commitments. Without your love and support, I would not be where I am today.

Table of Contents

List of Figures

List of Tables

Chapter 1: Introduction, Motivation, and Applications

The robotics industry has been growing over the last two decades addressing the emerging needs of a multitude of different sectors. From industrial automation in manufacturing plants to surgical robotics in the healthcare industry and unmanned vehicle systems in the government sector, the demand for robotics will continue to increase in the 21St century (Shukla, 2012). In 2012, the robotics market in North America recorded its strongest year according to Robotics Industry Association with an increase by 17% in robotic units and 27% in total sales which ranks the US second in robotic supplier worldwide (RIA, 2013). As industrial robotics continues to achieve a steady growth, innovation on many fronts is expanding the market including home, medical, government and public sectors. The use of a robot that can operate in a human living environment safely and accurately seems to be the common goal between all these sectors. Hardware and software that are cost-effective for mass production with simple maintenance will allow these systems to enter the competitive marketplace faster. In parallel, technological advancement in related fields such as electronics and open source software will set the conditions for the next phase of robotics. The reality of achieving flexible humanoid robot to care for the elderly, perform hazardous material experiments, assemble factory products around human workers and operate in outer-space will continue to motivate the research and engineering in this field.

Research Motivation

Low cost robotic solutions are limited in current industrial environment. This is typical for any evolving technology that is in the early phases. For example, computer technology in its early phases was cumbersome and reserved for large research facilities before it became a household commodity. The example of the cellphone is another illustration of how a complex machine has now become a user-friendly, common device all around the world. The robotics industry is undergoing similar transformation that began about a decade ago. There are few examples that are worth citing here to provide an overview of promising robotic technologies. Baxter, a low cost assembly line alternative, is capable of working alongside of human operators and can be taught

numerous functions by physically interacting with humans instead of pre-programmed planned operations. It has two dexterous arms with 14 degrees of freedom (DOF) and is capable of lifting five lbs. Sensing modalities include a 360-degree sonar, IR range sensors and five cameras. The entire system comes with a pre-installed robotic operating system (ROS) and takes less than two hours to implement. The cost of Baxter is reported to be in the vicinity of $22,000 (Landry, 2012). PR2 is an academic research platform from Willow Garage that is priced at about $200,000 and comes with only one arm. An additional arm can be acquired for extra $85,000 (Smith, 2011). The robot is equipped with stereo cameras, a tilting plane LIDAR scanner and a stationary plane LIDAR scanner object tracking and navigating around the dynamic human environment. The software is free and is available through the open source community with large repositories of usable code. According to the CEO of Willow Garage, Steve Cousins, "the arms are the most expensive part of the robot" (Engadget, 2013). Hence there is now a joint venture called Redwood Robotics that is solely focusing on the development of a low cost arm. Both robots are shown in Figure 1.1

Figure 1.1 Baxter the stationary robotic assembly line worker (left) and the PR2 research platform capable of dynamic localization and navigation (right). Under fair use policy (Deyle, 2012) and (Garage, 2012)

One of the prime goals of this thesis was to create a humanoid upper body platform that was significantly cost-effective and had all the required attributes including degrees of freedom, ranges of motion, power density ratios, sensing, and processing power. Maintaining human realism was necessary to enhance the rate of adoption in many scenarios. The goals for the finalized platform were to demonstrate an assistive robotic operation with teleoperative control or being controlled from a distant location over the internet. Advances in the vision capture systems are quickly gaining speed in terms of the reliability but they do not come close to human intervention, making the use of fully autonomous systems less practical in time intensive situations. In addition to the teleoperative control, another goal in this thesis was to have user-free human interface device (HID). Preprogramed routines, motions or sequences are typically coded or assigned through joysticks to manipulate the robotic system. However, the objective in this thesis was to create an interactive system whereby the operator uses his/her body to move the various joints of the robotic platform and create a seamless interaction between the robot and user opening the pathway for a more realistic teleoperative control. The undertaking was made possible by the evolution of the previous technologies/systems developed in Bio-inspired Materials and Devices Laboratory (BMDL) at Virginia Tech, the low cost alternative hardware and software that are currently available, and the additive manufacturing processes that significantly reduce the time from design to fabrication. Due to the goals and the versatility of the proposed upper body and hand system, the thesis is expected to provide foundation for many emerging applications such as disaster relief or explosive ordinance disposal (EOD).

Future Applications

About 3,300 United States casualties that have occurred in Afghanistan, 238 were killed due to IEDs in 2010 alone shown in Figure 1.2 (Whitlock, 2011). These include roadside bombs which are detonated close to soldiers in the field or in vehicles. To counter these attacks, the military has expanded its efforts in counterinsurgency information gathering, reconnaissance from Unmanned Arial Vehicles (UAVs), bomb-sniffing dogs, and ground robots. Once the IEDs are located, disposing them poses even greater technical challenge. A common trend for robotics is to accomplish those tasks that are dull, dirty or too dangerous for humans. Disarming and disposing of IEDs fits this vision and thus many companies have made effort to develop systems in this field.

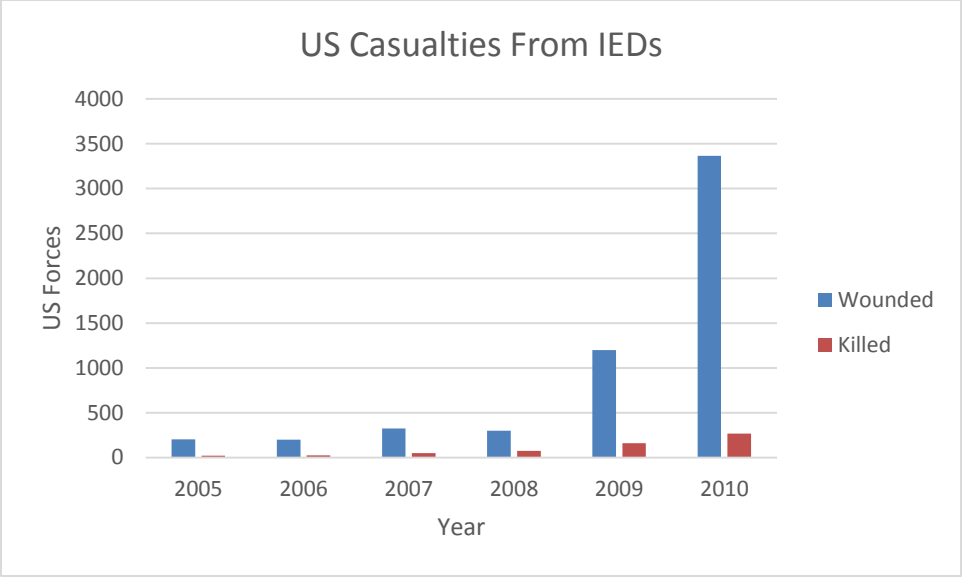

Figure 1.2 Casualites of road side bombs in Afghanistan from 2005 to 2010 . The number of IED events significantly increased from previous years.

Currently, the Department of Defense (DOD) is investing heavily in robotic technologies such as PackBots, predator drones and other smaller systems to conduct reconnaissance in the air and on the ground. This is exemplified by the fact that in February 2013, two contracts were awarded for over $27.3 million to supply the DOD with FirstLook robots and other miniature drones (RBR, 2013). DOD's investment reflects a small fraction of the millions of dollars spent on technologies for bomb detection robots. The question will remain whether or not military robots are the best way to clear an IED from the field.

The two technologies that seem to be prevalent over the past decade in disarming IEDs for robotics are the robotic claw and the mini-flail as shown in Figure 1.3. The claw, which is attached to a multi degree of freedom arm, is used for more delicate operations such as transporting the explosive to an uninhabited site before controlled detonation. This system has been used on many teleoperated robots for the last decade such as the Talon shown in Figure 1.3. The mini-flail is attached to the front of a ground robot and it sweeps over fields of mines with multiple rotating links which detonate the explosives on contact. These are used to clear a footpath for troops to walk through a field of mines. These two technologies are very simple and have been proven to work but are limited by ground topography and dexterity.

Figure 1.3 Talon robot from QinetiQ moving an IED shell (left) and The Protector by HDT with the modular mini-flail attached (right). Under fair use policy (Annear, 2013) and (Magnuson, 2012)

The other non-robotic option is for a trained professional to manually disarm the explosive with a bombsuit which is more efficient but comes at a higher risk. The bombsuit shown in Figure 1.4, is required to protect the operator from high levels of blast pressure, bomb fragmentation and thermal properties, but have numerous disadvantages and limitations. The suits are extremely bulky and have even been known to cause the operator to overheat because of the overlapping layers of Kevlar, plastics, and other composites that over insulate the body heat. The bombsuit also lacks gloves which gives the user the necessary mobility for completing the task effectively but exposes their hands to any accidental detonation (Wikipedia, 2013). The large suit also degrades situational awareness to foreign enemies and tactical readiness due to issues of fogging in the visor and large weight of approximately 80 lbs. There is a distinct gap between the drones used for EOD and the bombsuit that the operator can wear. The robot systems provide little dexterity in situations that require fine motor skills such as clipping wires or grasping delicate objects. The bombsuit has hand dexterity but lacks mobility for the rest of the suit as well as it does not fully protect the operator. The gap in protection and mobility is the main motivation for developing a human-like upper body that can be mounted on to the mobile platform.

Figure 1.4 Bombsuit capable of protecting the user from IED devices. Hands are fully exposed for full hand dexterity. (Loughran, 2011)

EOD is not the only application that requires the dexterity and range of motion similar to that of human being. For example, hazmat crews working on disaster relief operation can use the same technology for their needs. The nuclear disaster at Fukushima in 2011 would be an example where human-like dexterity would be ideal as it would prevent exposure of nuclear radiation to the human workers. The World Trade Center relief effort would be additional example that could have been simplified with the help of a similar robotic system. A laboratory assistant capable of handling dangerous chemicals for experiments would be another instance of where this system would be extremely capable and keep humans a safe distance away. Having a robotic upper body with full human dexterity that can be easily controlled via teleoperation will provide the assistance needed for fields such as search and rescue missions, hazmat disposal, chemical handling, and many others. The system being discussed in this thesis will bridge the gap between giving the user full dexterity over the life-sized humanoid robot and protection through teleoperation.

Based on these promising applications, design specifications were formulated. In order to be fully capable in all situations the max ranges of motion needed to be simulated. For example manipulating hand tools of various sizes and shapes required dexterity and precision in the finger

joints. To be sufficient in numerous applications required human ranges of motion with 3 DOF in the shoulder, 2 DOF in the elbow/forearm and 16 DOF in the hand/wrist. The power supplied by the motors had to be capable of lifting a maximum of 5 lbs in a controlled motion. A full feedback control was necessary for precise joint position. The geometry of the upper body and arms had to fit in the confined anatomy of a 6ft tall human in order to allow for the largest power density of the motors and be able to fit in an environment built around human ranges of motion.

Biological Background

Human anatomy has evolved over millions of years in order to provide the dexterity and ranges of motion that our upper body is capable of producing. In order to mimic these motions, research was conducted to understand how the underlying tissue, bones and muscle groups interact with each other. The shoulder and arm were the primary focus for this thesis. The shoulder is composed of multiple muscle groups which are necessary for the wide range of motion shown in Figure 1.5.

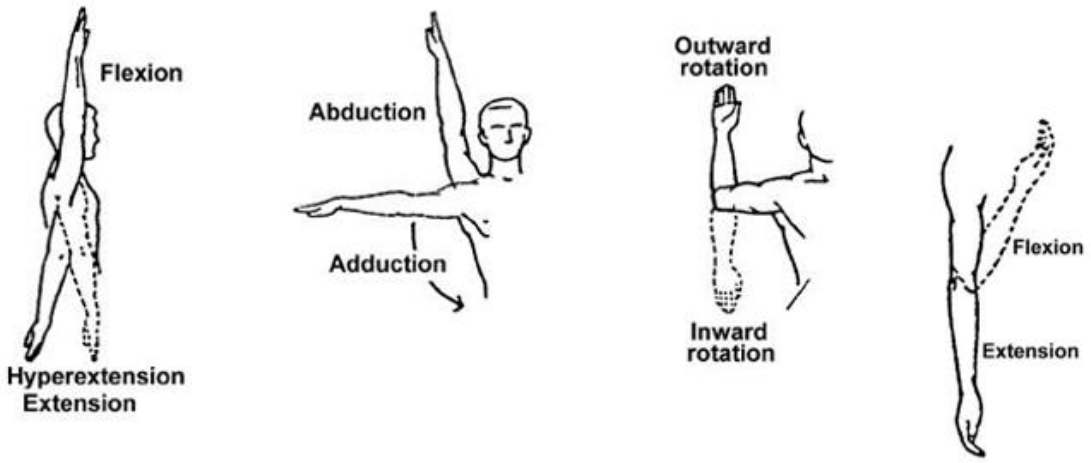

Figure 1.5 The four degrees of freedom in the shoulder and upper arm. Under fair use policy (ArmyMedical)

Four muscles make up the underlying rotator cuff: supraspinatus, infraspinatus, teres minor, and subscapularis. These muscles are responsible for small amounts of abduction and rotation as well as keeping the humerus in contact with the clavicle and scapula that form the ball and socket joint respectively (Laura Inverarity, 2010). The outer lying muscle on the shoulder is the deltoid that is responsible for the large ranges of motion of flexion and abduction. Moving down the arm, the bicep and tricep are responsible for flexion and extension of the elbow respectively.

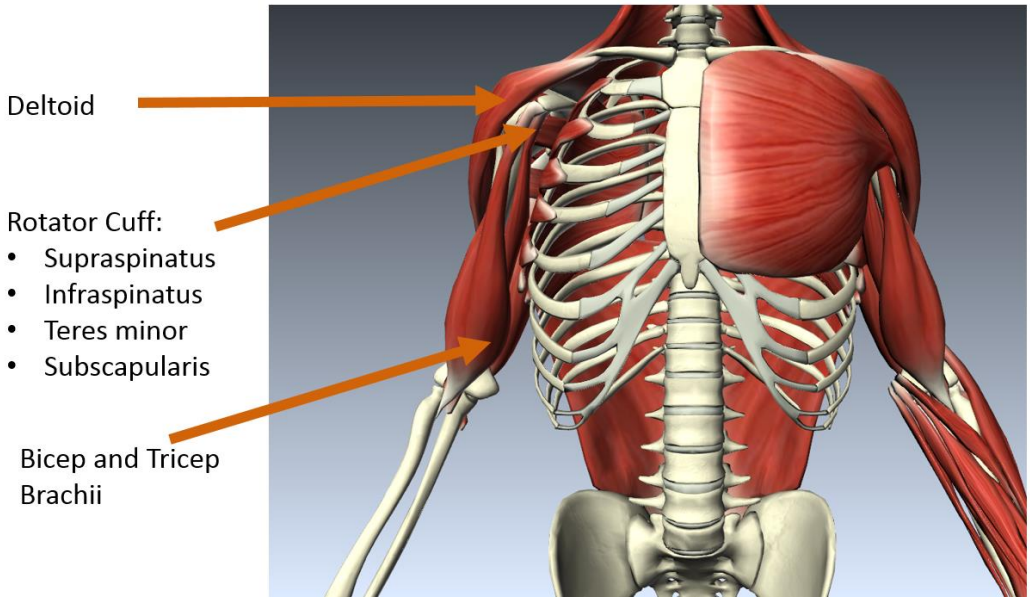

Figure 1.6 Upper arm muscles that provide flexion, abduction and rotation of the arm as well as flexion and extension of the elbow. Under fair use policy (BioDigital, n.d.)

The human hand is also vastly complicated due to the high degree of dexterity required for each of our fingers. Surrounding the ulna and radius bones in the forearm are the extensors and flexors. The extensors are connected via tendons that attach to the top of each phalange and are required in order to fully extend the fingers. The curling of each joint is done by the flexors which are located on the underside of forearm. Theses muscles and their respective tendons flow through the wrist to each of the phalanges being controlled. By having opposing forces in each joint, the fingers reach a desired position by dynamic changes of tension in the flexor and extensor muscle groups. Widening and tightening of the fingers is accomplished with the

abductor and adductor muscles in the palm. These are necessary for different grip strategies in terms of holding objects.

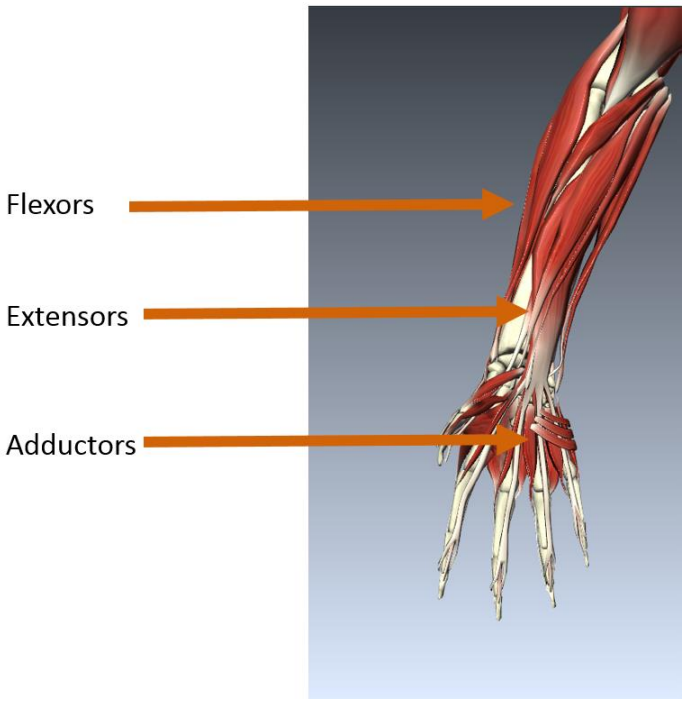

Figure 1.7 Anatomy of human forearm depicting the flexor, extensor and adductor muscle groups Under fair use policy (BioDigital, n.d.)

Chapter 2: Design of DASH Hand

Introduction and Literature Search

From a robotic design standpoint, the human hand is one of the most difficult appendages to be replicated by mechanical components. The 22+ degrees of freedom, the confined geometry and the abundance of feedback due to touch sensing makes mimicking the human hand a complex problem. Many commercial entities have attempted to address this challenge and have proposed unique solutions. However, these solutions are equally complex and expensive which prevents their deployment in common applications. Reduction in cost and complexity are the main reasons why most of the commercial robotic hands utilize simple claws and passively actuated grasping systems to complete their tasks.

In last five years, there have been numerous advances in both intrinsically and extrinsically actuated humanoid hands. Intrinsically actuation systems place the motors in the hand to actuate the fingers. Typically these are small DC motors that use pulleys or geared systems to actuate the linkages in each finger. Intrinsic actuation systems have a niche market in prosthetics due to the reduced weight of the system and simplicity of the motions. Intrinsic actuation usually requires a larger-than-human geometry to fit all the components in the hand. Few systems have succeeded at making a hand that is human sized and capable of achieving the same force output as a tendon driven system. In contrast, extrinsically actuated systems closely emulate the biology by actuating the fingers with tendons in a forearm. Due to the larger geometry of the forearm, larger motors can be accommodated to provide a higher power density to the fingers. Below are some of the most modern technologies relevant in each of these two groups.

Meka, a robotics company, has released the H2 Compliant Hand which features a 12 Degrees of Freedom (DOF) intrinsic system with five actuators as shown in Figure 2.1. Each finger is under actuated giving it compliance and reducing the weight of the hand. Excessive forces to the fingers are mitigated due to the finger compliance. The three fingers and thumb have series elastic actuators that measure the tendon force based on a spring between the motor and finger

tendon for precise control. The entire system weighs close to 800g and can grasp a weight of 2 kg (Meka, 2009).

Figure 2.1 The 3 fingered Meka intrinsic hand is fully modular at the wrist with self-contained electronics for use on a separate robotics system. Under fair use policy (Meka, 2009)

Kinea Design, now part of HDT Global and contracted by John Hopkins Applied Physics Laboratory, successfully demonstrated a mechanical prosthetic hand with biomimetic geometry, dexterity, and sensory feedback as shown in Figure 2.2. The hand contains over 80 sensors that measure temperature, texture, pressure, friction and points of contact. This information is communicated back to the amputee through implantable MyoElectric sensors wired directly into their nervous system. Each finger is driven by one motor in the palm to make natural curling motions and compliance when grasping objects. The program was sponsored by DARPA's Revolutionizing Prosthetics program to give wounded soldiers returning home a realistic prosthetic that acts and feels like a real hand (Kinea, 2009). A price for this hand or even the subcomponents was not mentioned but the program was funded with a budget of over $70 million to 30 participating organizations (APL, 2009).

Figure 2.2 Prosthetic hand designed by Kinea with motors at each joint and a multitude of sensors for sending information to user's nervous system. Under fair use policy (Kinea, 2009).

Sandia National Labs has recently developed an intrinsically actuated hand as shown in Figure 2.3. The technology was developed for one of the DARPA's project in order to develop a cost-effective robotic hand with modularity and high dexterity. The three fingers and thumb are identical units with three DOF. Each of the three fingers have a motor self-contained in the proximal end for flexion and another for abduction. The design simplifies the anatomy of a human hand by eliminating the pinky finger and removing the distal joints. The palm contains the electronics and a flexible tissue like structure for extra surface area when gripping the objects. The fingers connect to the palm with self-aligning magnets making the entire system modular and facilitating the rapid repair to the fingers if they become detached from the palm. The system is projected to have a low cost of $10,000 which is about 90% less than the other competitors in the market (Hobby, 2012).

Figure 2.3 Sandia National Labs intrinsic hand with modular fingers attached to a palm platform. Under fair use policy (Hobby, 2012).

Each of these prior hands were designed with different end goals. From a design standpoint, it becomes tedious to incorporate the proper motors and sensors in each finger for intrinsic systems. This requires making compromises in the design by either reducing the number of fingers or passively actuating the joints. The hands look bulky in comparison to the extrinsic systems because of the motors required for the typical grasping force of 10N per finger. Following the biological hand design, it is imperative to place the actuators in the forearm because of the larger geometry, allowing more motors at a higher power density.

Extrinsically actuated humanoid hands have been pursued by several larger firms and government agencies. Robonaut 2, or R2, is the latest development from NASA featuring a humanoid upper body with a head and two arms Figure 2.5. Each of R2's hands have 12 DOF with a grasping force of five pounds and is capable of Cutkosky's 16 grasps strategies as shown below

in Figure 2.4. The fingers have custom six-axis load cells at each digit of the hand providing it excellent tactile sensing capability. Embedded Hall sensors are also located in each finger for precise positional feedback of the joints. The tendons are controlled with force sensors and motor encoders on the actuators (Guizzo, 2012) . The entire system was packaged in a very human-like geometry with a mesh layer covering the circuitry, actuators, and components. The inspiration of this system came from the advances made in extrinsically actuated hands by the Shadow Robot Company.

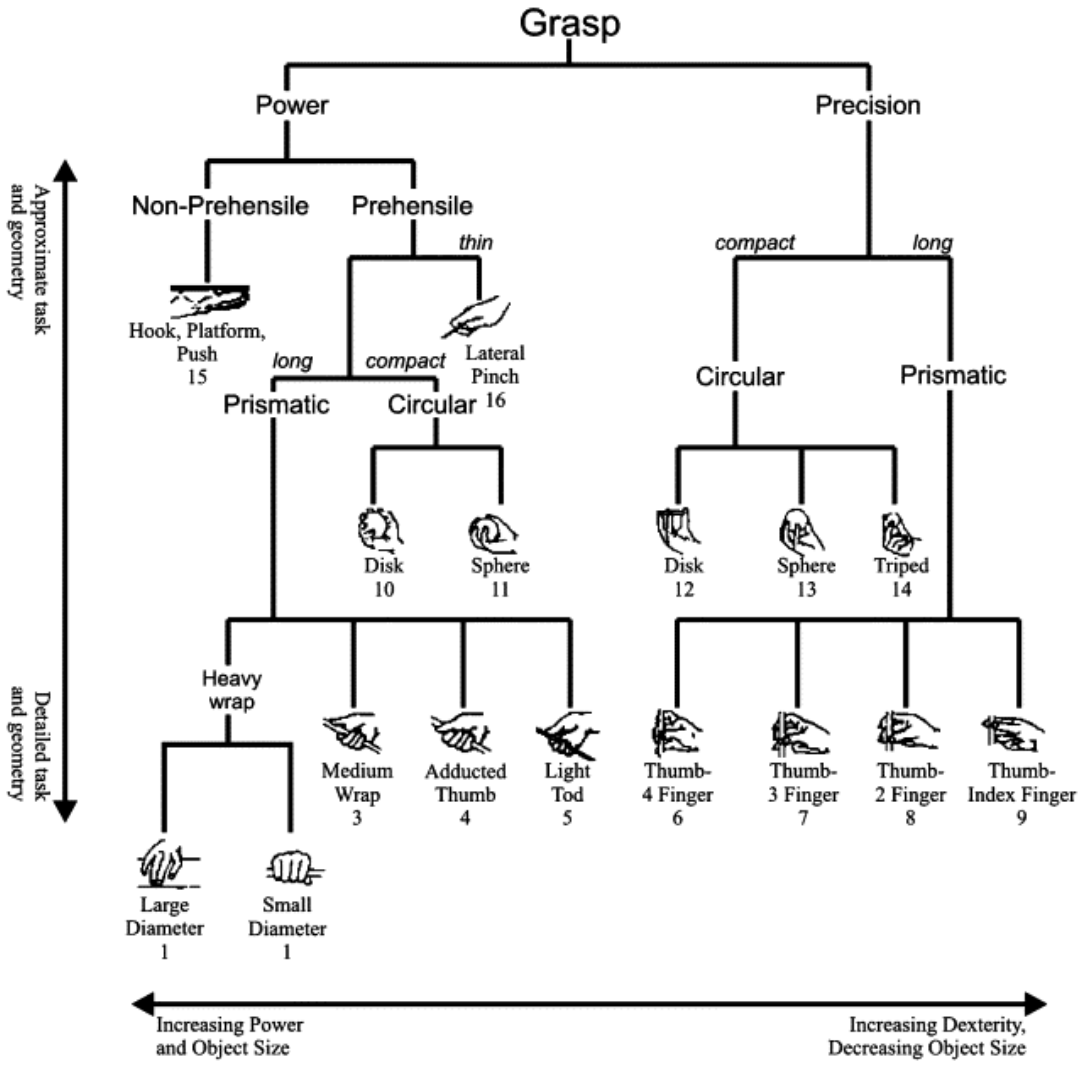

Figure 2.4 Cutkosky's 16 grasps strategies shown in separate columns of power vs. precision. Under fair use policy (M.R. Cutkosky, 1990).

Figure 2.5 Robonaut 2 extrinsically actuated humanoid hand with force sensors around each finger link. Under fair use policy (Guizzo, 2012).

The Shadow Dexterous Hand is one of most dexterous and well-built hands currently available but has a high cost of $250,000. The Shadow hand has 24 DOF (20 actuated and 4 under actuated) to closely mimic all the motions of a human hand. Each finger has three DOF and the thumb has 5 with the other DOF coming from the wrist and palm. Each degree of freedom is tendon driven with the choice of pneumatic "Air muscles" or electronic "Smart Motor" actuators shown in Figure 2.6 (Shadow, 2013). The air muscles allow for compliance and are measured with a solid state pressure sensor at the valve manifold. The smart motor system measures the force of each pair of tendons driving each joint of the finger. Hall Effect sensors measure the rotation of each joint and the additional BioTac tactile sensors embedded in the fingertips are capable of measuring

force, temperature and vibration. The entire system is open source and capable of being teleoperated with a data glove or autonomously with software (Shadow, 2013).

Figure 2.6 Shadow smart motor platform (left) and Shadow air muscle platform (right) holding objects with its dexterous 24 DOF hand. Under fair use policy (Shadow, 2013).

The Institute of Robotics and Mechatronics at the German Aerospace Center, known by the acronym DLR, has also been a leader in humanoid robotics. Currently most of the humanoid hands are connected directly to motors or actuators in a way that does not accommodate for accidental forces that may occur during the real world operations. DLR introduced a novel compliant hand that has variable stiffness actuation to compensate for dynamic collisions shown in Figure 2.7. The ability to mimic biology gave it a competitive edge against the other competitors in the market of extrinsic-driven humanoid hands. Each joint was driven by two custom motors for antagonistic drive and variable stiffness just the same as human fingers are driven by opposite muscles that are always in tension. The 2 DOF wrist and 19 DOF hand required 42 motors, each with the nonlinear compliant mechanisms. The mechanisms were modular with the position

sensor, motor, and stiffness sensor on one PCB for fast replacement of each tendon actuator. The initial results showed that the hand can drive a nail with a 500g hammer without damaging the actuators or system (Markus Grebenstein and Alin Albu-Schaffer, 2011). DLR has demonstrated several humanoid hand designs including many generations of the DLR-Hand that incorporated intrinsic actuators with timing belts for compliant stiffness, harmonic drives, flat motors and torque sensors (H. Liu, K. Wu, P. Meusel, N. Seitz, G. Hirzinger, 2008).

Figure 2.7 DLR Hand-Arm system with extrinsically actuated 21 DOF hand and 4 DOF upper arm. Under fair use policy (Markus Grebenstein and Alin Albu-Schaffer, 2011).

Areas of Improvement and Background

The design of a human hand in this thesis evolves from a previous iteration developed at Virginia Tech termed as the Dexterous Anthropomorphic Robotic Typing (DART) hand shown in Figure 2.8. The size and weight of the arm and hand were optimized to be biomimetic. The hand and forearm were extrinsically actuated with 16 servo motors for the finger flexion and abduction as well as 3 servo motors for the wrist actuation. Tendons attach each finger to an actuator and the return force was achieved through a torsional spring. The medial and distal joints were coupled in each of the fingers with a four bar linkage to remove the need for adding another motor. Positional

measurement was redundantly driven with a Hall sensor but further calibration was necessary. The system was designed to type on a keyboard to quantify the dexterity, speed and accuracy of the position achieving roughly 20 words per minute. The entire system was 3D printed with filament extrusion technology for rapid prototyping (Priya, 2011). This chapter builds upon the architecture of DART and introduces a novel actuation system that significantly improves upon the prior technology providing the desired performance of hand and forearm.

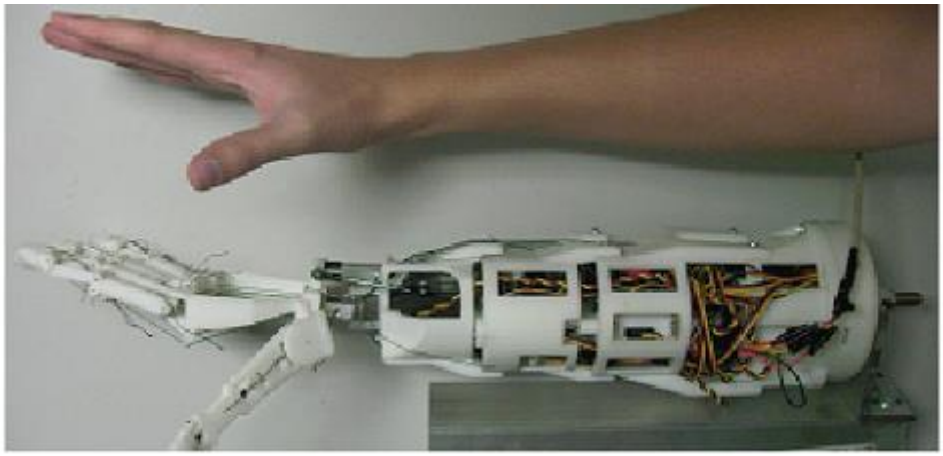

Figure 2.8 Humanoid DART hand shown next to a human hand and forearm for comparison. Under fair use policy (Priya, 2011).

The design focused on a hybrid approach of combining intrinsic and extrinsic actuation in a human-like shape. The Dexterous Anthropomorphic Sensor-Driven Hybrid-Actuation (DASH) hand follows a similar design approach from an anatomical and mechatronic standpoint but numerous modifications were made to mitigate a majority of the problems experienced in the DART Hand. The requirement of maintaining the hand and arm in biomimetic dimensions were incorporated during the design process. The entire system had to accommodate the required drivers, motors, sensors and other electronics within the confined anatomical geometry. The other design parameters of the second generation hand were done to mitigate a majority of the problems experienced in the first design. Modularity of the fingers, palm, tendons and forearm were crucial to reduce the maintenance and repair time. Robust positional feedback at the joints was necessary to achieve accurate feedback without relying solely on the servo motor sensors. New U-joints for

the wrist and fingers were introduced to eliminate the high amount of friction of the tendon cables at the extremes of each degree of freedom. The factor of safety also required the U-joints to be increased to accommodate large forces at the joint. The sum of these requirements along with the previous design goals of biomimetic designs, high power density ratios, high degrees of freedom and low cost needed to be addressed for DASH. The final end state was to have a system that was dexterous, powerful, and modular with a cost factor of at least one order of magnitude smaller than any commercially available equally-capable systems.

Dimensions and Range of Motion

The design specifications for the humanoid hand and forearm required the geometry to fit within the geometry of a 50th percentile adult male shown in Figure 2.9. This constrained the design to be 193mm x 89.6mm x 42.6mm in length, width and height of the humanoid hand. Digit length for the distal, medial, and proximal phalanges was taken into consideration for each finger. DASH hand shown in Figure 2.10 features the ring finger and index finger measuring 96 mm in length from fingertip to proximal joint, while the pinky and middle finger measured 76mm and 101mm respectively.

Body Size of the 40-Year-Old American Male for Year 2000

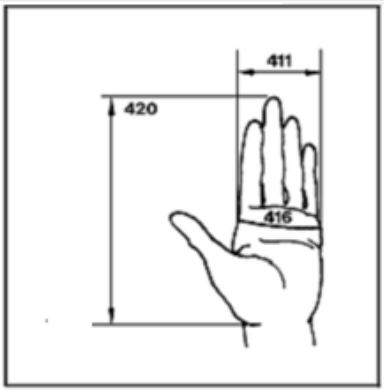

No.	Dimension	5th percentile	50th percentile	95th percentile
420	Hand length	17.9 (7.0)	19.3 (7.6)	20.6 (8.1)
411	Hand breadth	8.2 (3.2)	8.9 (3.5)	9.6 (3.8)
416	Hand circumference	20.3 (8.0)	21.8 (8.6)	23.4 (9.2)

Figure 2.9 Human hand critical dimensions for the average male of 40 years of age. Under fair use policy (NASA, 2000).

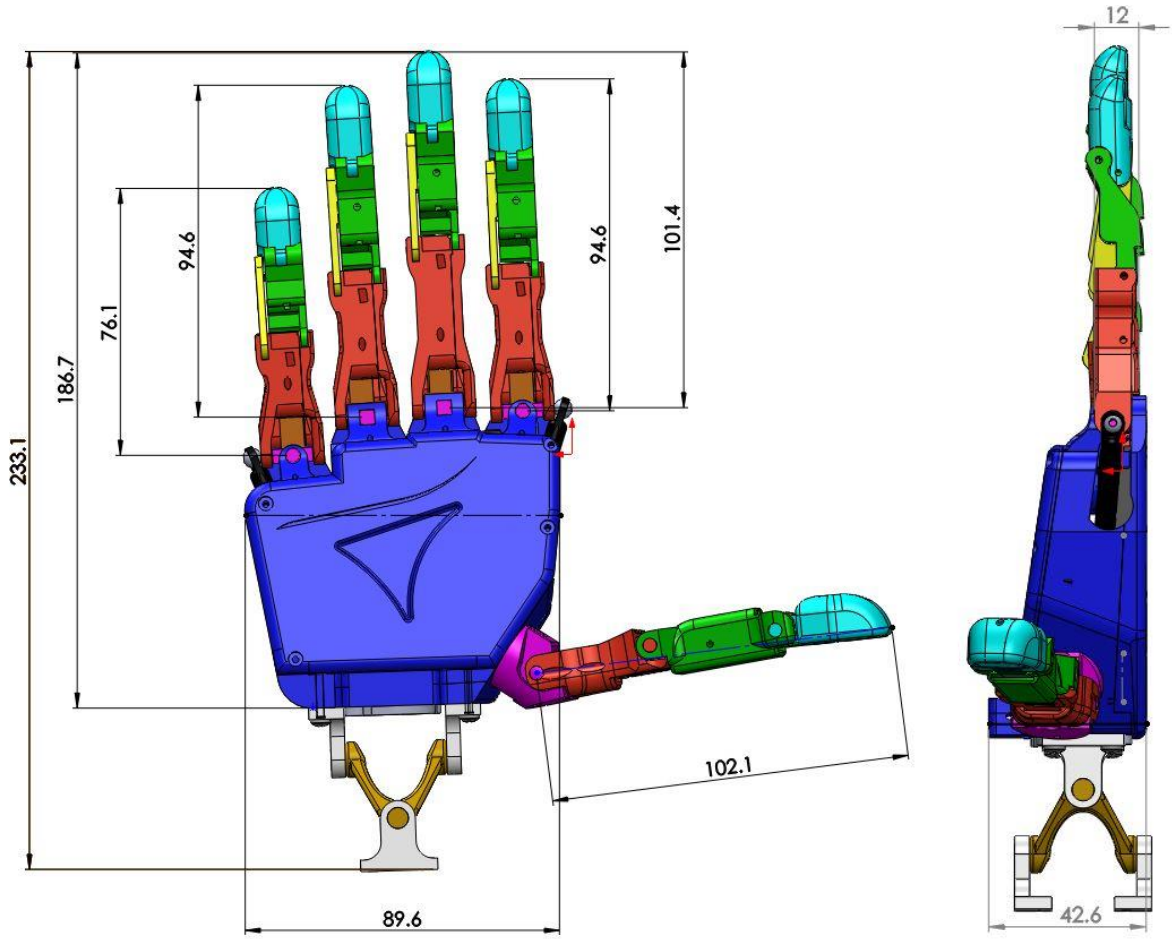

Figure 2.10 Dash hand design with proximal, medial and distal links of the fingers shown light blue, green and red respectively. The palm is shown in dark blue and each of the fingers attaches to the palm via the pink u-joints.

Measurements were taken for ranges of motion of abduction in the index, pinky and thumb joint abductions. Literature suggests that the range of motion is typically between 20-25 degrees for the fingers and 70-80 degrees for the thumb as shown in Figure 2.11 (a). From the measurements that were taken in our laboratory, most hands were capable of a little over 30 degrees at maximum extension for the fingers which became a design constraint as the major abduction range of motion Figure 2.11 (b).

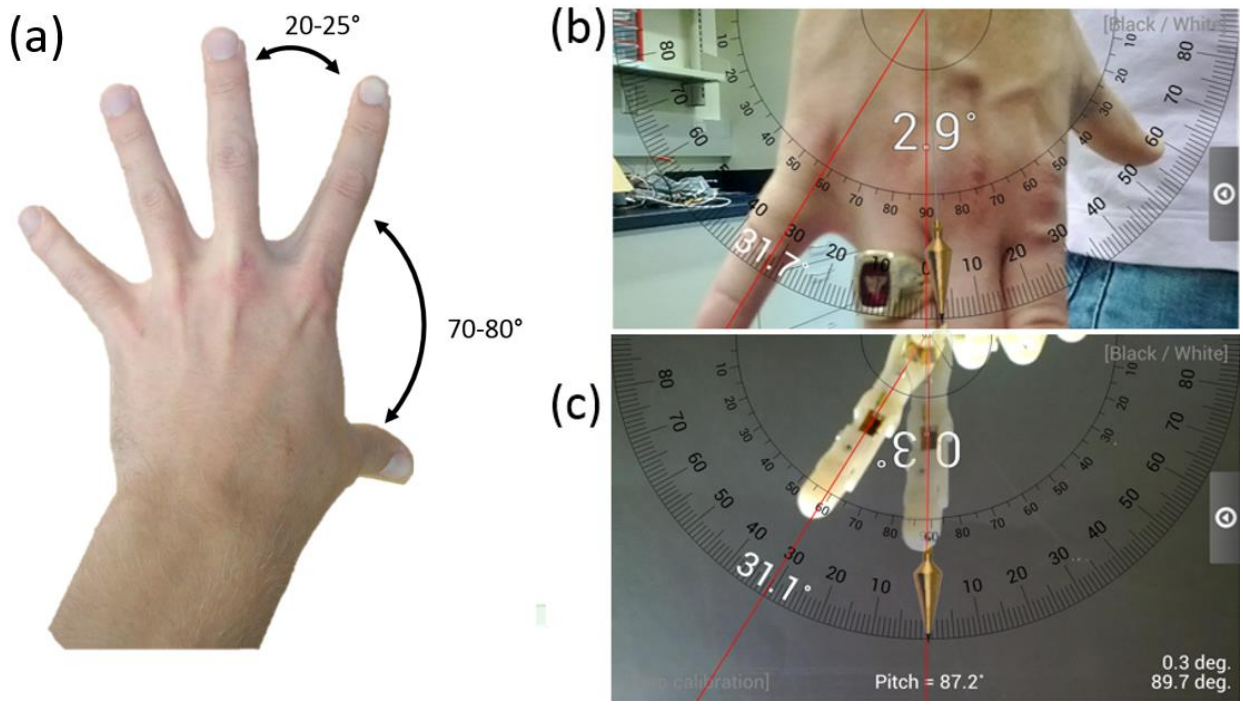

Figure 2.11 (a) Abduction of index is 25° for the fingers and up to 80° for the thumb. (b) Actual measurements for index and pinky abduction were measured closer to 31°. (c) Final model shows the same range of motion was achieved.

The abduction components of the humanoid hand play an important role in performing different grip articulations. Of all the digits in the hand, the opposable thumb is the most crucial abduction joint. It is the thumb that allows the formation of the c-shaped-grip, power-grip, and the precision-grip. Widening the width of the finger allows for grasping larger diameter objects in a "C-Shape" fashion. Precision-grips take advantage of finer dexterity. The ability to combine these different grip strategies into one design allowed the use of multiple scenarios. In comparison to the DART hand, DASH improved the design by eliminating abduction of the middle and ring finger, two lesser degrees of freedom in the hand. After careful analysis, it was found that these joints are less useful for the different grip strategies because they do not widen the grip size but merely make the hand look more realistic by providing equal spacing when abducting each of the fingers in unison. This design choice to exclude these two degrees of freedom in the new hand design was also driven by geometry which will be discussed in the motor placement section.

Flexion, or the bending moment around a joint of the fingers, followed a similar design path as the DART hand but with some modifications. Each of the flexion joints relies on a passive actuation to provide a counteracting force and return the joint to its initial position. Spring steel was implemented to provide this return force instead of torsional springs allowing for more design freedom in sensor and tendon placement. The same 4-bar linkage was used to couple the distal and medial flexion motions into one actuated motion shown in Figure 2.12. The tendon attaches the medial joint and with rigid rods the medial portion actuates the distal portion of the finger as well. This allows for a passive driven joint that still produces a natural human motion and simplifies the actuator selection. Typically most humans do not exhibit a need for just distal flexion in daily activities so coupling this motion was a logical design choice.

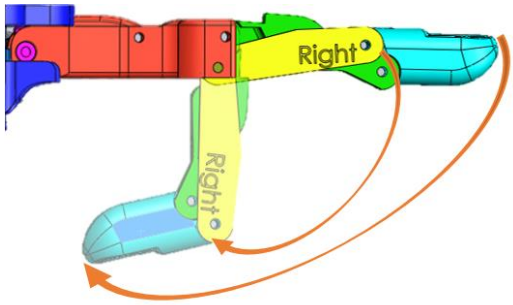

Figure 2.12 Finger flexion of medial joint coupled with distal joint in a four bar mechanism.

The ranges of motion for each joint were crucial for accomplishing different grip strategies as described earlier. Abduction joints result in widened grips for larger objects while flexion joints help in grasping. Extrinsic actuation allows for more power for each motor and also for adding more than one degree of freedom for each joint. Multiple components of flexion allow for more dexterous manipulation of objects. The final design in Figure 2.13 shows the capabilities of flexion and abduction in the DASH hand.

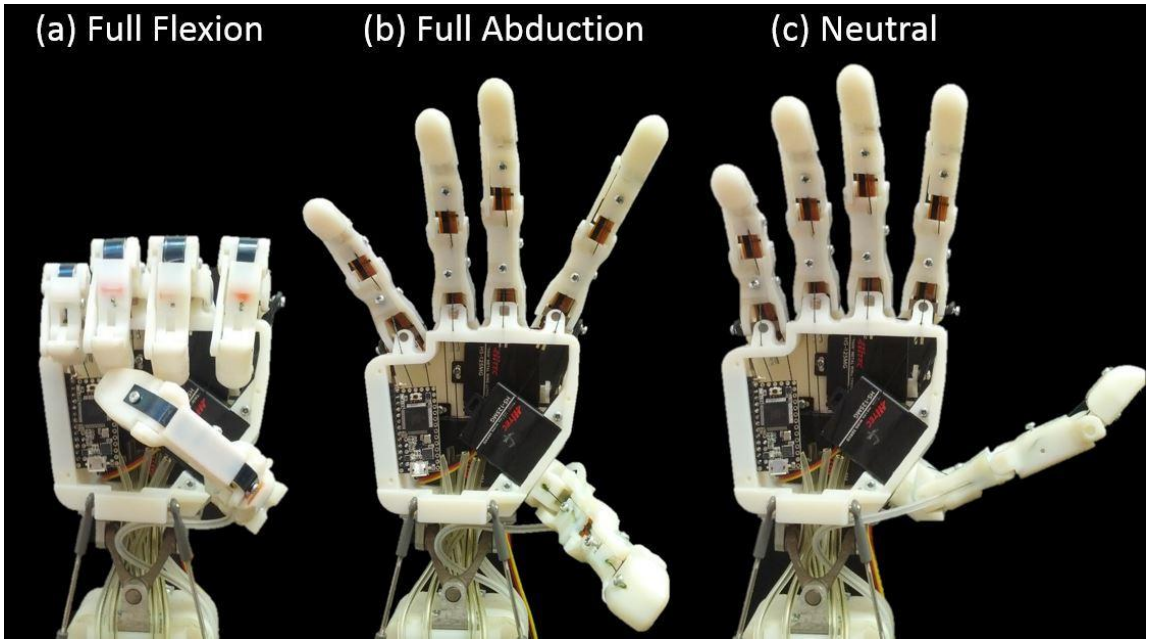

Figure 2.13 (a) Full finger flexion is possible with the use of 11 actuated degrees of freedom. (b) Widening the grip size is accomplished with the three servos located in the hand responsible for abduction. (c) The neutral position shown is the condition where none of the motors were actuated.

Sensor Selection

The addition of sensors in each actuated joint provides additional feedback to assist in position control over the flexion motions. Because the tendons would be unintentionally driven during wrist actuation the design mitigated this movement in two different ways. First, by incorporating a Bowden cable design in the middle of the wrist, the tendons would experience less unintentional actuation. Secondly, by the inclusion of sensors at each actuated joint gave the ability to monitor the actual position which is highly desired in cases when the hand was obstructed by a foreign object.

Bend sensors shown in Figure 2.14 were chosen over typical potentiometers or encoders because of the size, cost-effectiveness and lack of mechanical degradation. The Flexpoint bend sensor is a conductive ink based material laminated on a substrate and used to measure the deflection by change of resistance. Essentially, the sensor is a variable resistor that is used to measure the bending. These sensors come in a various lengths but are slim enough to fit in the

width of a typical human finger. They are ideal for DASH because they do not occupy large area yet they can measure joint angles effectively.

Figure 2.14 Bend sensor shown against a piece of spring steel measuring 32mm x 8mm in length and width. The metal connectors can be bent vertically for installing into the finger system

The DART hand incorporated a torsional spring to help in returning each digit back to the normal resting position. This is an effective solution but the use of bend sensor forced the design to find an alternative that still provided the necessary return force. Initial concepts had the bend sensor and spring steel encased at the center of each actuated joint. Testing showed that the small radius of curvature inside the finger was not ideal for the spring steel and caused fracture due to the forces exceeding the tensile strength. Spring steel was used to provide the returning force instead of a torsional spring or a second motor. Using a second motor to counter the effects of the flexion system would be expensive and occupy limited design space for a tendon driven system. The spring steel was placed on the outside of the joint which allowed a larger radius and greater return of motion for the finger. Plastic sheaths were originally cut to length to help guide the spring steel back to its initial orientation as shown in Figure 2.15 (a). Over time the plastic would deform and the sharp edges of the spring steel would slice through the plastic, rendering the joint incapable of returning to neutral position shown in Figure 2.15 (b). The plastic sheaths were replaced with a more permanent solution. Channels were printed on top of the respective digits allowing for a

smooth return force and minimal assembly/maintenance. The channels were wide enough to accommodate one or more large pieces of spring steel of the same size for returning higher loads Figure 2.15 (c). The final design used a modular approach to allow for easy assembly shown in Figure 2.15 (d). The printed channels were modular for the proximal joint and can be unscrewed from the link to allow the spring steel to be easily attached once the finger is mounted to the palm.

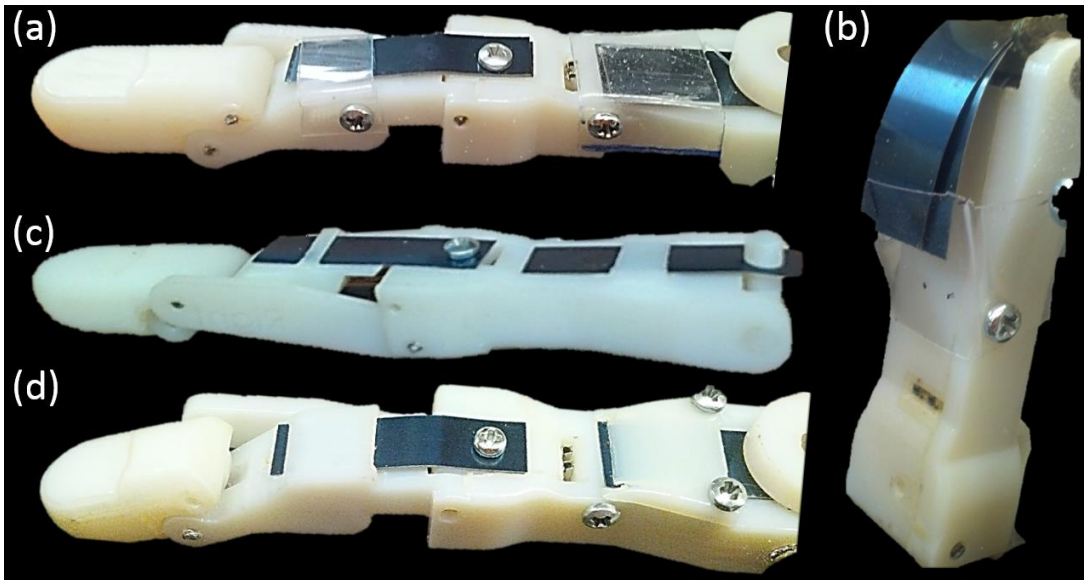

Figure 2.15 (a) First design of the bend sensor holding plastic shown on top of the index finger. (b) The spring steel catching on the side of plastic sheath making the joint not return to neutral. (c) Second generation with thinner plastic supports built into the 3D printed index finger links. (c) Final design with modular 3D printed plastic supports to remove spring steel faster.

Spring steel calculations

The readily available strips of spring steel come in the form of AISI 1074/1075 and 1095. AISI 1074-1075, also known as scale-less blue steel, has less of a return force but is easier to bend initially. AISI 1095, or blue-tempered steel, has a higher yield strength and is used in applications that are under continuous stress. The manufacturer of this spring steel does not rate the yield strength of the strips which makes it difficult in choosing the correct material but following the standards of AISI the yield strength for these materials should be around 190-210 GPa (AZOM, 2013).

The geometry of the finger and the return force were the main controlling factors in determining the spring steel dimensions. A thick piece of spring steel was not ideal for a small radius of curvature. Calculations were necessary in order to identify the correct thickness and proper return force of each joint. Each piece of spring steel was clamped at one end and allowed to freely slide through the channel. The setup of this system can be approximated as a cantilever beam with the left end fixed and a force in the downward direction on the right. The initial design goal was to find the correct width range that would make a radius of curvature at 4 mm around the fixed location achievable. Radius of curvature was calculated by the following equation:

$$Curvature = \frac{1}{R} = \frac{d^2y}{dx^2} = \frac{M}{E * I}$$

where M is equal to the moment due to the force acting on the beam, E is the Elastic Modulus and I is the moment of inertia. The moment of inertia for a prismatic beam is given as

$$I = \frac{1}{12} wh^3$$

whereby w is the width of the spring steel and h is the height of the spring steel. With a given force of 12 N, modulus of elasticity of 200 GPa and length, width and height of the spring steel at 25.4 mm x 6mm x 22 mm respectively, the radius of curvature was calculated to be 3.5mm. Using this as a base, the design goal of the complete system was to drive the radius of curvature of each joint using this same calculated measurement. Keeping the same force and enlarging the spring steel required a larger radius of curvature depicted in Figure 2.16. After testing multiple samples of spring steel varying in thickness, the results indicated two pieces of 0.01" thick spring steel were required to provide the accurate return force for the desired length and radius of curvature.

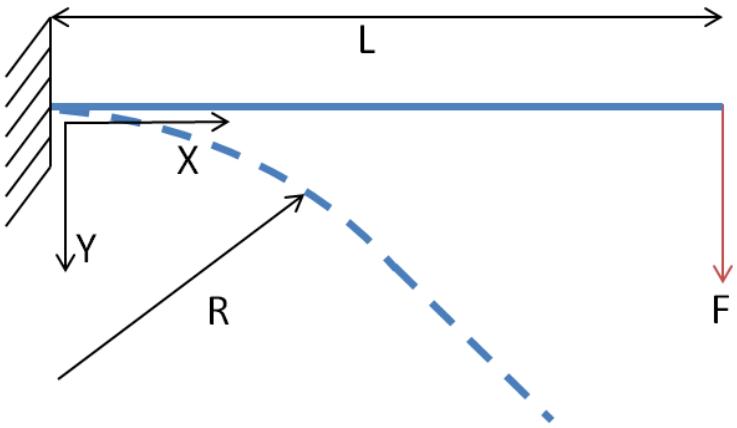

Figure 2.16 Spring steel diagram relating the force applied by the tendon (F) to the radius of curvature (R) of the spring steel based on length (L).

Motor Placement

DASH is a unique combination of extrinsically and intrinsically actuated system. The previous version, DART, was developed as a fully extrinsic system with all the motors in the forearm. This allowed for the tendons to be free flowing in the palm but also left a large geometry unused. Other extrinsic systems also take advantage of this space in tendon driven systems. Looking towards biology, it was logical to place the abduction motions in the hand instead of the forearm shown in Figure 2.17. This also reduced the length of the forearm without additional motors for abduction placed in the geometry. The thumb, index and pinky proximal joints would be driven with a single wing servo in order to reduce the addition of another motor and take advantage of the space shown in Figure 5. Since each of these motors were internal to the palm and did not require a set of tendons passing through the actuated wrist, it was confidently assumed that the motor position alone would not be affected and thus the use of additional sensor measurements to assess the position of the servo was not necessary. The two motors driving the index and pinky joints were connected with a ball joint on a push pull rod directly in line with the printed u joint. This allowed for actuating the flexion portion of the joint without drastically interfering with the abduction portion and vice versa. Due to the size of the palm the thumb was directly interfaced on the servo without any other mechanism.

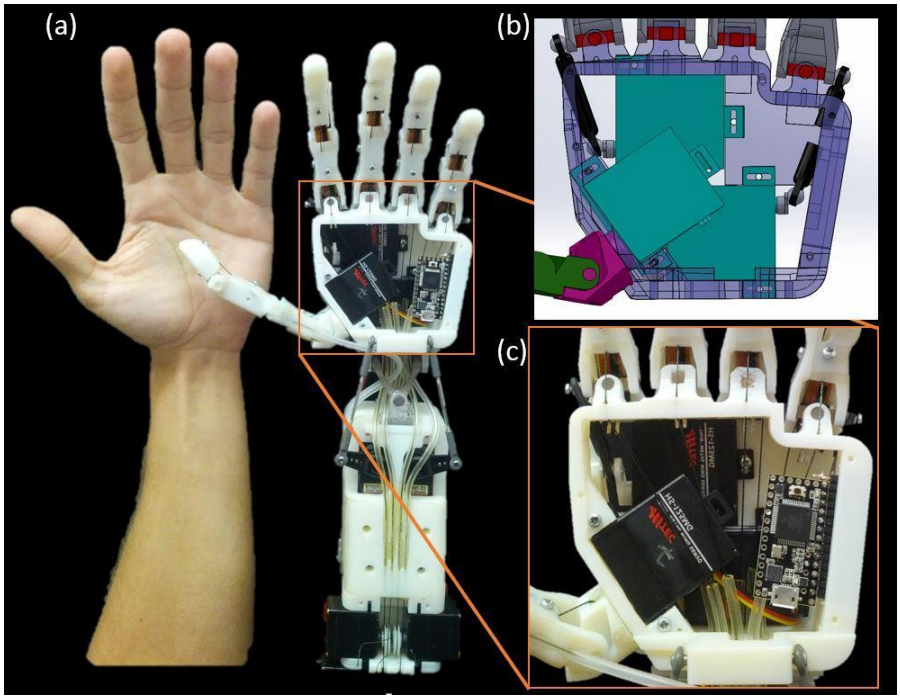

Figure 2.17 (a) the DASH hand is compared to a human hand to give a sense of dimensional accuracy. (b) Intrinsic motor placement for abduction of the thumb, index and pinky joints. (c) Palm design of intrinsic motors including the microcontroller and tendon routing.

Wrist Design

The wrist design went through several design changes from the initial conception. Keeping with the ideology of the DART design, a U-joint was included that allowed cables to pass through and was able to rotate in both x and y planes. The DART wrist design needed improvement because it was not modular, robust or strong enough to handle the high dynamic loads. A custom U-joint was developed to mitigate these issues. The first design offered a wide inner diameter at 20 mm to allow for multiple Bowden cables to pass from the forearm to the palm without interference. Having the tendons pass through the center of the wrist offers the least amount of change in length of tendons as the wrist is actuated. This design was to be milled out of five pieces of aluminum and then assembled to create the U-joint. The major issue with this design was if the wrist was fully actuated to one extreme in either direction. It rotates the hole of hand directly in line with the attachment post of the U-joint and causes interference. The next iteration mitigated this issue by offsetting the rotation points of the u-joint by 12mm and shrinking the attachment post height to

compensate for the offset. This allows the u-joint to be actuated in any extreme without pinching the tendon system on the attachment posts. This new design was 3D printed to achieve the desired precision. Tensile strength became an issue as 3D printed plastic is extremely brittle at 60 MPa. The final design uses the thickened offset geometry printed in a stainless steel infused with bronze to produce a more robust wrist joint at 682 MPa. This increased the tensile strength by a factor of 11 and still allows for a large amount of tendons to pass freely through the wrist without interference shown in Figure 2.18.

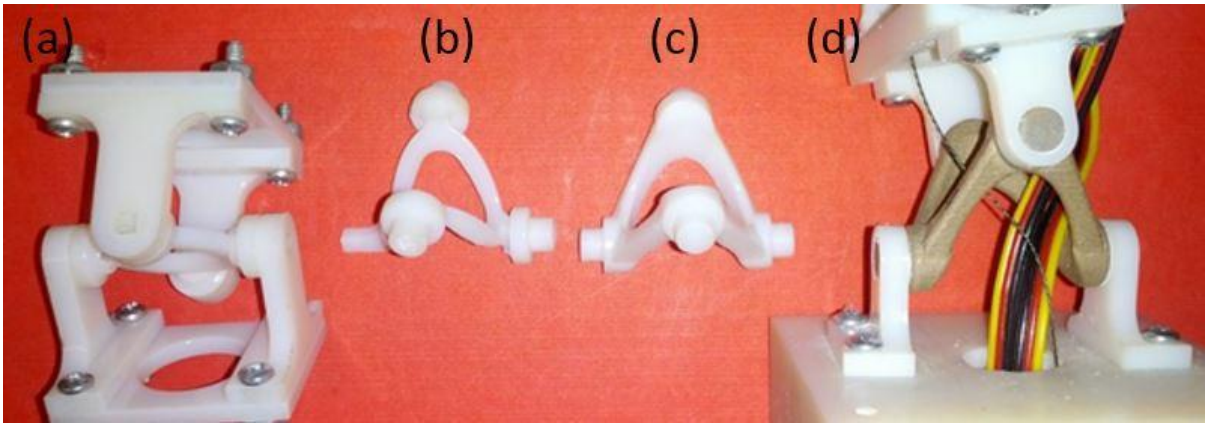

Figure 2.18 The evolution of the wrist (a) in-plane wide u-joint, (b) split-plane thin member u-joint, (c) split-plane thickened member u-joint, and (d) final split-plane u-joint 3D printed in stainless steel and sintered bronze.

With the assistance of two Hitech HS-7980th servo motors providing 611 oz-in each, the wrist is capable of sustaining a 5.64 lbs (2.56 kg) load shown in Figure 2.19. This is excluding any applied force from the flexion or abduction joints. This load exceeds the maximum requirements established by the initial design specifications.

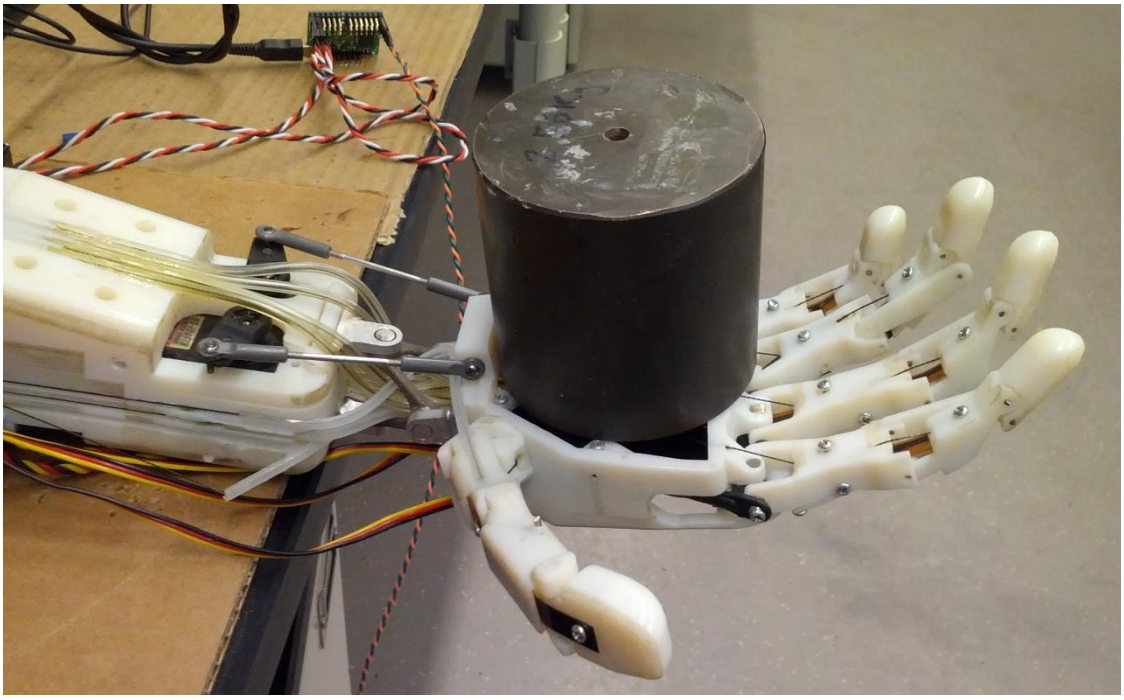

Figure 2.19 Wrist design supporting a 2.56 kg load in the center of the palm.

Change in Tendon Length

Custom servo horns were fabricated for each tendon actuator. The appropriate servo horn diameter was derived from the change in length equation of the fingers being actuated around the center of rotation. The initial and final length of the tendon, L_i and L_f is given as:

$$\Delta L = \sqrt{(a^2 + b^2)} - \sqrt{(c^2 + d^2)}$$

where *a* and c were equal to the height and b and d were equal to the lengths of their respective hypotenuse displayed in Figure 2.20. Each of the tendons for the joints were found to be 14mm of change except for the proximal joint of the Thumb which was 7mm. After finding the change in length, the diameter was back calculated by solving for D through the following equation:

$$\Delta L = \frac{\theta \pi D}{360} \quad => \quad D = \frac{\Delta L * 360}{\theta \pi}$$

where θ is the minimum angle of bend in each joint defined as 85° based on human range of motion. The horn diameter was rounded to even 20mm. Based on the known angle of motion and the velocity of the servo motors, it was calculated that each joint actuation should take roughly 0.5

seconds to complete. This is within the acceptable range of most human hands and meets the requirements of our design goal in terms of a biomimetic extrinsic actuator driven hand.

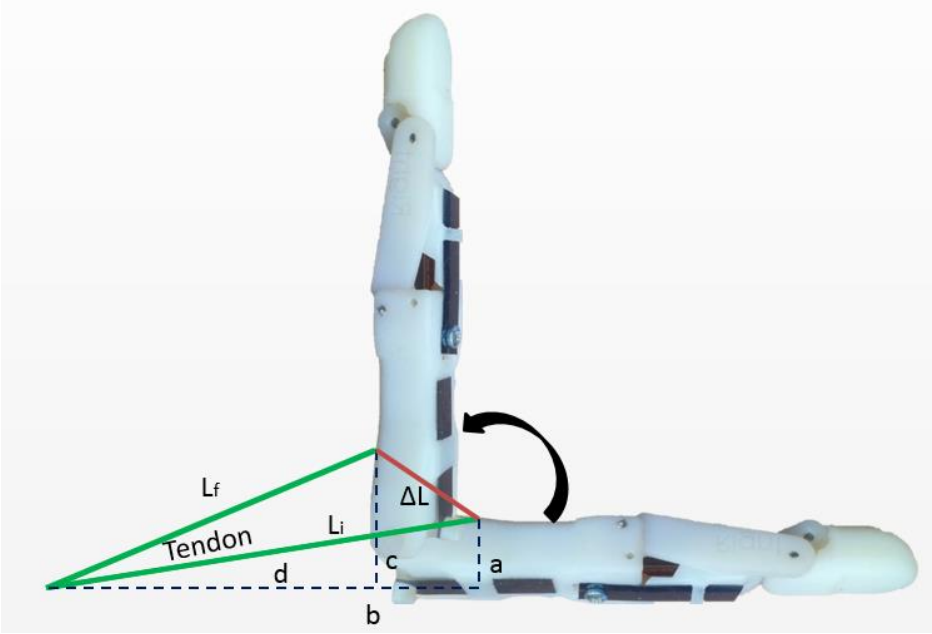

Figure 2.20 Change in length diagram showing the tendon in green with the finger at neutral (horizontal) and fully actuated (vertical).

Kinematics

The kinematics of the hand were assumed to have a fixed-base joint located at the center of the palm. Each of the links connecting the thumb were assumed to be in parallel to this initial base joint. The hand was seen as a separate sub-system from the forearm which will be discussed later. The abduction joints in the thumb, index, and pinky fingers can be viewed as a universal joint with two degrees of freedom. Each of the other revolute joints are 1 DOF. The distal joints in the four fingers are coupled with the motion of the medial joints as discussed previously shown in Figure 2.21.

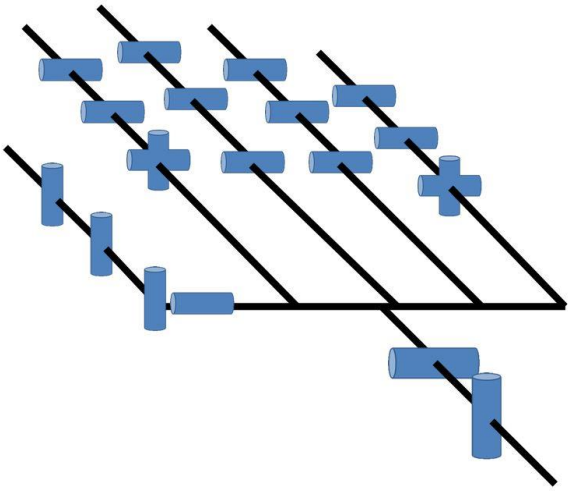

Figure 2.21 Kinematic model of hand. Each blue cylinder represents a rotational degree of freedom. The distal and medial joints are coupled for each of the fingers. The wrist is driven by a parallel design.

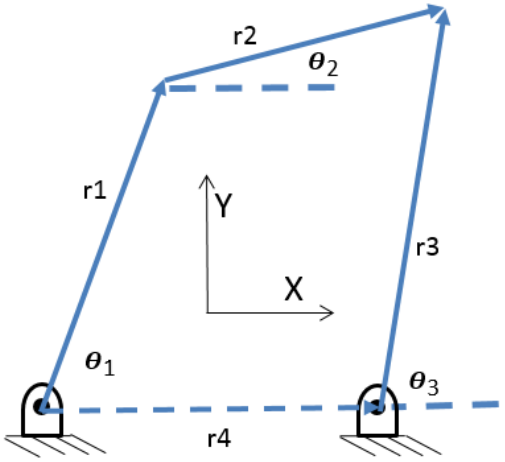

Figure 2.22 Kinematic analysis on four bar mechanism represented by four vectors: r1, r2, r3, and r4.

The kinematic analysis for the four bar mechanism was solved by forming the loop closure equation. This was done by splitting the links into sets of vectors that have the same final coordinates

$$r1 + r2 = r3 + r4$$

where r2 is the distal joint base plane represented as a line segment and r4 is the distance between the grounded links r1 and r3. By setting the equation to zero and taking their respective X and Y components, the following algebraic equations represent the four line segments:

$$r1 \cos(\theta_1) + r2 \cos(\theta_2) - r3 \cos(\theta_3) - r4 = 0$$
$$r1 \sin(\theta_1) + r2 \sin(\theta_2) + r3 \sin(\theta_3) = 0$$

where θ_1 becomes the independent variable and is held constant at a fixed angle between 0-90°. Line segments *r1, r2, r3 and r4* are set to the following dimensions of 29.9 mm x 6.3 mm x 32.1 mm x 6.2 mm respectively which allows for solving of the specific angular position of r2. The location of the fingertip can be calculated by knowing the position of the base of the distal joint, r2.

The kinematics of the wrist were more challenging due to the parallel actuation method in the wrist shown in Figure 2.23. Typically most robotic systems are serial links in nature but by having the motors side by side instead of built into the wrist was advantageous for biomimetic principles and to reduce the overall weight. The design also allows for the tendons to pass through the center of the wrist for smooth rotation and reduction in friction.

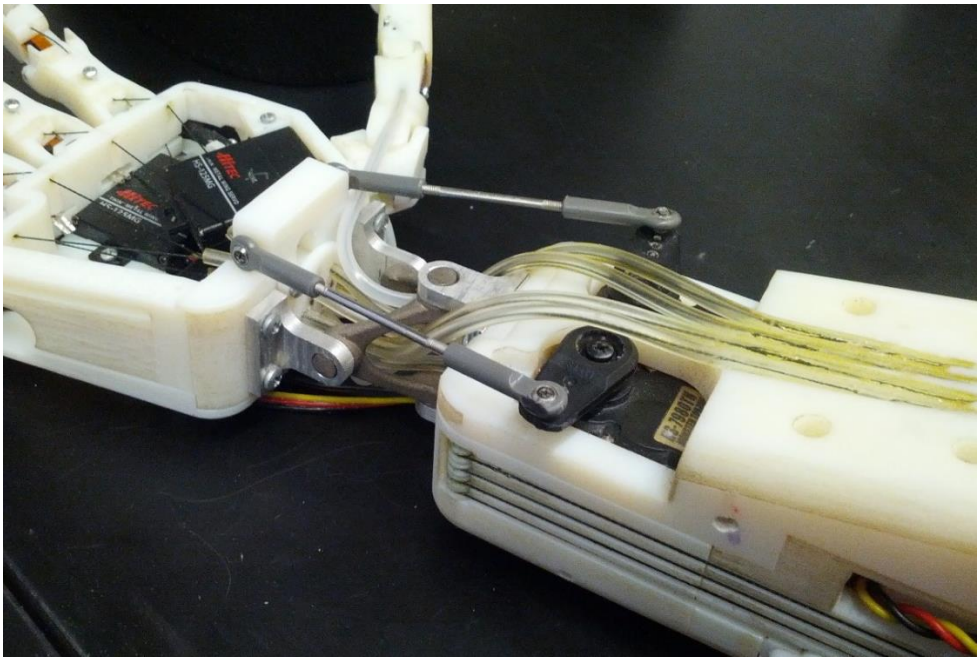

Figure 2.23 Parallel actuation method for 2 DOF in the wrist. Metal rods connect the servo horns to the base of the palm with ball joints.

Rotation matrices were used to calculate the required angle of revolution of the two servo joints based on the desired angle inputs of yaw, pitch and roll. The roll angle should be zero if the forearm is not rotation about the elbow joint. The rotation matrices for roll, pitch and yaw are

$$Rotation\ (x) = \begin{bmatrix} 1 & 0 & 0 \\ 0 & \cos\gamma & -\sin\gamma \\ 0 & \sin\gamma & \cos\gamma \end{bmatrix}$$

$$Rotation\ (y) = \begin{bmatrix} \cos\theta & 0 & \sin\theta \\ 0 & 1 & 0 \\ -\sin\theta & 0 & \cos\theta \end{bmatrix}$$

$$Rotation\ (z) = \begin{bmatrix} \cos\theta & -\sin\theta & 0 \\ \sin\theta & \cos\theta & 0 \\ 0 & 0 & 1 \end{bmatrix}$$

where the concatenation of the three rotations forms

$$R = Rx * Ry * Rz$$

This final rotation matrix is multiplied by the neutral positions of palm side ball joints to give the ball joint positions of JointR and JointL.

Electronics and Controls

It was essential that the entire hand be modular to allow future replacement/repair and modification with simplicity. This design goal led to the creation of an enclosed sensor housing in the palm with a micro controller that deciphered the joint positions of each of the actuated fingers. Originally an off-the-shelf Arduino chip was selected to be used in the palm but due to geometric constraints and number of analog pins, a similar product called *Teensy 3.0* was chosen. The *Teensy 3.0* packs 34 I/O, where 10 of which are PWM channels and 14 are analog inputs as shown in Figure 2.24. The *ARM Cortex* chip runs 48 MHz powered by the micro USB. The entire device measures 1.4” x 0.7” and cost around $20. Overall, this device met the requirements in terms of size, speed, ease of use, cost and support for 11 analog bend sensors in the hand.

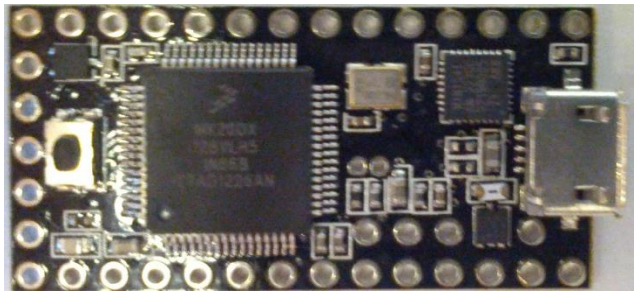

Figure 2.24 Arduino-based Teensy board measuring 0.7" in width and 1.4" in length.

In order to characterize the analog signal of each joint measurement, a voltage divider was used to find the change in resistance for the angle shown in Figure 2.25. The bend sensor can be approximated as a variable resistor that has an increased resistance based on an increase in deflection. The ideal voltage divider, or the one that produces the maximum sensitivity to the change in resistance, can be calculated by finding the min and max resistance in order to optimize for the correct pull-down resistor (Schmeder, 2008). The following voltage divider schematic shows how the sensor input would take place.

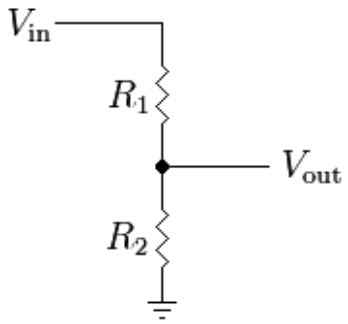

Figure 2.25 Voltage Divider where Vin = 3.3V, R1= Bend Sensor, Vout = Analog Reading, and R2 = fixed resistor.

The minimum and maximum resistance of the sensor for 0 to 90° was measured with an ohm meter to be 10-200 KΩ respectively. Given the range of R1, the maximum and minimum voltages that the board will read can be calculate as

$$Vout_{min} = \frac{R2 * Vin}{R2 + R1max}$$

$$Vout_{max} = \frac{R2 * Vin}{R2 + R1min}$$

The derivative of the voltage ranges was taken with respect to R2 giving the following equation

$$\partial_{R2}\left(\frac{R2}{R1_{Min} + R2} - \frac{R2}{R1_{Max} + R2}\right) == \frac{R2}{(R2 + R1_{Max})^2} - \frac{1}{R2 + R1_{Max}} - \frac{R2}{(R2 + R1_{Min})^2} + \frac{1}{R2 + R1_{Min}}$$

By solving for zero and R2 as a positive value the final equation becomes

$$R2 = \frac{\sqrt{-R1_{max}{}^2 * R1_{min} + R1_{min}{}^2 * R1_{Max}}}{\sqrt{-R1_{max} + R1_{min}}}$$

which for the chosen bend sensors produces a fixed resistance of 39 kΩ. The wiring diagram for the 4 voltage dividers in the flexion of the fingers is shown in Figure 2.26.

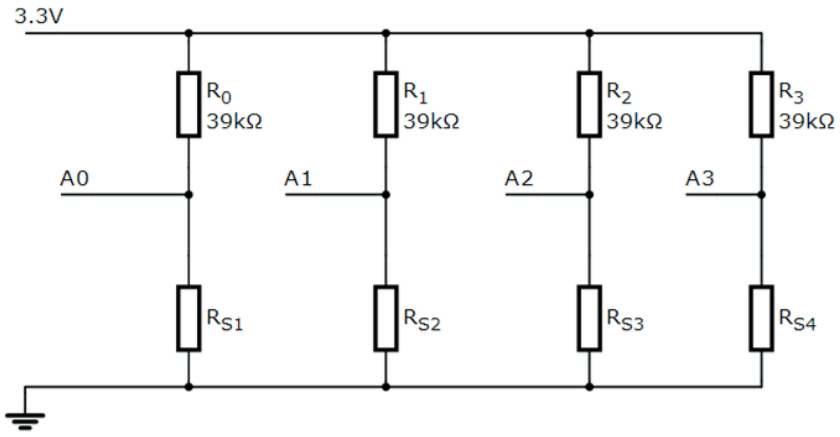

Figure 2.26 Simplified circuit diagram showing the first four flexion sensors with cascaded voltage dividers.

Conclusion

This hybrid actuation robotic hand offers a versatile and low cost solution that is attractive for applications requiring dexterous manipulation. The use of COTS servo motors, microcontrollers and 3D printing technology allows the DASH hand to accomplish high DOF manipulation at a an order of magnitude lower price compared to the products currently on the market. The design is modular for rapid repair, if necessary, and fits within the dimensions of a human arm. This biomimetic approach allows for intuitive operation with the assistance of a data glove that measures the joint positions of the user. Future testing will be conducted to quantify the joint forces and speeds. The incorporation of pressure sensors at the fingertips embedded into a silicon skin is currently being investigated to give the user a sense of grip force on objects. Testing is currently underway to evaluate the different grip strategies possible for manipulation of common hand tools.

Chapter 3: Design of Upper body

Introduction and Motivation

The restriction in the degrees of freedom (DOF) in the shoulder and large motor power requirements makes designing an efficient biomimetic upper body of a humanoid robot a challenging task. Using the currently available commercial components, the replication of the complete human anatomy is not feasible. One of the main limitations is imposed by the low power density of the motors. Because of these limiations, humanoid engineering design must compromise on the biomimetic aspects to meet the system requirements in terms of; degrees of freedom, geometric size, cost, and power density of the joints. The second generation upper body system, which is the focus of this thesis, utilized previous advances made at Virginia Tech and was completely redesigned to mitigate the issues associated with weight, size, power, and modularity in the first generation.

In the earlier generation of the upper body, the focus was on developing the functionalities suitable for the medical simulation application. These simulations incorporated different medical scenarios in which the robot performed tasks in order to provide the medical student training in a 'life-like' situation. This included movement in the arms and shoulder to allow the robot to have the capabilities of simulating an adverse situation such as a seizure. Realistic life-like arms incorporated RFID sensors that allowed measuring intravenous medication and the pulse rate. These features proved to be complimentary to that available in other simulators that lacked physical motion. The presence of physical motion influenced the decision-making process of the student being trained.

The requirements for a new upper body were dictated by the vision that robot could be used either as a remote semi-autonomous or as a teleoperative assistant in scenarios where employing a human would be exceedingly dangerous. The reasoning behind teleoperation was to impart the capabilities of human motion in terms of strength, fluidity of movements and range of motion. Additionally, the goals included designing this upper body within the confines of the human anatomy with natural degrees of freedom. The focus of this chapter will be on describing the design

iterations for each subcomponent, manufacturing process for the upper body, assembly, and testing of the final design.

Current Technologies

A comparative benchmark analysis was conducted to assess the performance of robots currently in the marketplace. A few examples from the benchmark are exemplified below. One existing design that was investigated based upon the information available in literature was the HRP-4 from Japan's National Institute of Advanced Industrial Science and Technology. This humanoid is 151 cm (5 ft.) tall and weighs only 39 kg (86 lbs) as shown in Figure 3.1 (AIST, 2011). Because weight was a main design constraint, it is helpful to examine a lightweight design that has achieved a high power output for future applications where the upper body attaches to a mobile platform. The kinematics behind the HRP-4 shoulder was one of main focus in the literature review.

Figure 3.1 HRP-4 Robot with 34 DOF and each arm weighing 0.5kg. Under fair use policy (AIST, 2011)

A robot developed in Germany, ARMAR III, incorporates a modular structure for the shoulder with three degrees of freedom shown in Figure 3.2. The overall system has 43 DOF including two arms, a holonomic platform and vision capabilities (T. Asfour, et al., 2006). This platform was capable of perception including object tracking, location and 3D image construction.

Figure 3.2 ARMAR III home assistant robot with mobility base and vision system. Under fair use policy (T. Asfour, et al., 2006).

The information derived from the literature as well as the experiments conducted on the first generation of the upper body provided the requirements for the upper body (Priya, 2011). These requirements included 4 DOF in the shoulder/upper arm area, light weight, and the ability of the arm to lift at least five pounds beyond that of its own weight. In doing so, the overarching goal was to keep the design close to that of normal human morphology.

First Generation Design

The first iteration of humanoid upper body was fabricated out of steel and welded parts (shown in Figure 3.3) which made the entire platform extremely heavy, rigid, and incapable of

being repaired easily due to the lack of a modularity (Priya, 2011). The motor and gear sizes utilized in the first iteration required large magnitudes of current and occupied most of the space available within the framework of the robot. Also, there was no shoulder flexion/extension so reaching forward to pick an object was not possible. The system control was designed without feedback so a closed-loop control was not available for manipulation.

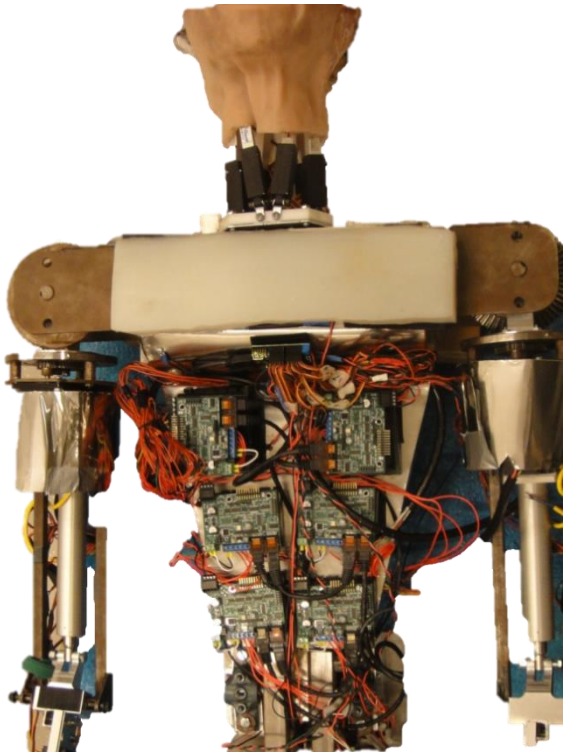

Figure 3.3 Design of the upper body for medical simulation weighing 50 lbs. This first iteration had 2 DOF in each shoulder measuring 23" for shoulder span and no feedback control.

The linear actuator located in the upper arm that drives the elbow was first tested to evaluate if the specifications met design requirements capable of lifting 5 lbs. Also in the upper arm, a smaller DC motor was incorporated to provide the rotation of the shoulder that replaced a larger stepper motor. The shoulder joint provides the arm with two additional degrees of freedom: flexion/extension and abduction/adduction. By adding a third degree of freedom and reducing the size of the shoulders the entire design became more biomimetic. The torso area was also made more efficient from the previous generation by eliminating unnecessary components, streamlining

the internal cable system, and reorganizing the assembly parts. All these new features were integrated into the arm-shoulder which reduced the overall size of the design by 2 inches in the shoulder span and provided overall weight reduction of roughly 15 lbs.

The design for the upper body was divided into three subsections: torso, upper arm, and shoulders. In the torso section, the electrical component layout and wiring were redesigned to be more compact, better organized, and have reduced weight. A spine structure was designed to resemble that of normal human to support the upper body and was also utilized to feed the wires and cables through the length of the torso. For the upper arm, the linear actuator used for the bicep in the first iteration was tested to determine whether it would meet the new design requirements. The elbow, mounting plate, and gear system were all redesigned in the upper arm to improve the overall assembly and make it modular for ease of repair. A new efficient rotational motor for shoulder rotation was researched and selected. The primary goal for the shoulder was to reach forward and lift an object. Adding the flexion and extension degrees of freedom allowed this to be achieved. The motors that controlled the shoulder and arm movement in the first iteration were replaced with lighter and more efficient motors, which greatly reduced the overall weight of the upper body while enhancing the functionality.

Torso Design

The design of the torso required that it is not only supportive and rigid but also of nominal size in order to accommodate the other mechanical components in the upper body. Incorporating the additional third degree of freedom into the shoulder design required another two motors to be placed in the torso which restricted the space in the lower chest cavity for electronics. This was solved by manufacturing a rectangular frame machined out of aluminum and attached to the motor mounts of the four stepper motors. Lightening holes were used around this frame to reduce the unnecessary weight. A spinal column was built from 80/20 aluminum stock and brackets that mounted directly to the motor frame. It was chosen for its small size, lower weight, strength, and ability to easily attach/detach fixtures. The entire robot was supported from this 80/20 stock post that measured 40 x 40 x 370 mm.

The limited space within the torso region required efficient layout to contain all the electrical components. Because the torso was designed in a tapered shape to mimic the morphology of a human torso, it minimized the cable length and consolidated the components. A plastic channel wire runner attached to the spinal column assisted in organizing the wires running from components in the torso to the head, shoulders, arms, and lower body. The electronic components on the torso were bolted to a 1/8 inch thick transparent acrylic plate. This chest plate holds each of the motor controllers, microcontrollers, fanless Fit-PC, and power supply shown in Figure 3.4. The primary design constraint for the chest plate was the geometry.

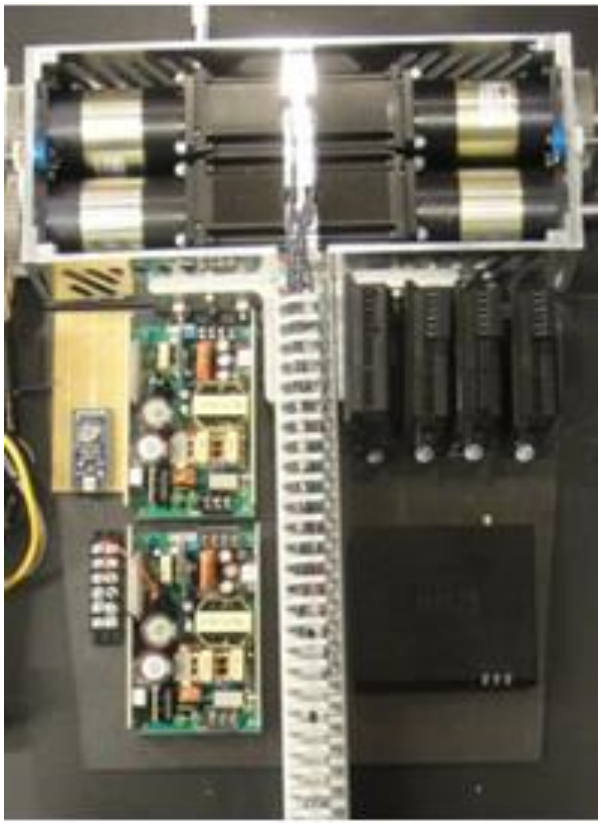

Figure 3.4 Picture of the torso assembly, which includes the 80/20 erector rod spine, cable management runner, acrylic chest plate, and the four NEMA motors.

Upper Arm Design

Actuator Testing and Selection

Before redesigning the upper arm, the strength and speed of the current linear actuator was tested to determine if it would meet the goal of lifting 5 pounds. To simulate forces acting on the elbow, a 1.33 pound metal bar was modified to replicate the forearm weight while lifting objects of different weights. To hang the weights from the bar, a hole was drilled approximately where the hand would grip objects and two more holes were drilled on the opposite end to easily attach the bar to the current elbow joint. To impose the most torque on the linear actuator, the robot was positioned upright and the weights were lifted perpendicular to the ground against gravity. The angular position of the bar from zero degrees (bar pointing down) to 150 degrees was timed. The LabVIEW program used to control the robot included velocity, acceleration, and deceleration parameters that were adjusted for each test. The velocity parameter was set to 6, 9, 12, 15 and 18 rev/sec and the acceleration was adjusted to 30, 50 and 70 rad/s^2 for the testing. Weights ranging from 0 to 5 pounds were individually hung from the bar to record the times and to identify the limits of the linear actuator.

There was a positive linear trend for angular speed versus velocity. This validated the assumption that as the velocity increases, the angular speed of the joint increases proportionally. At 5 pounds, the ideal settings were a velocity of 12 rev/sec and an angular acceleration of 30 rad/s^2 which produced an angular speed of 65.24 deg/sec shown in Figure 3.5

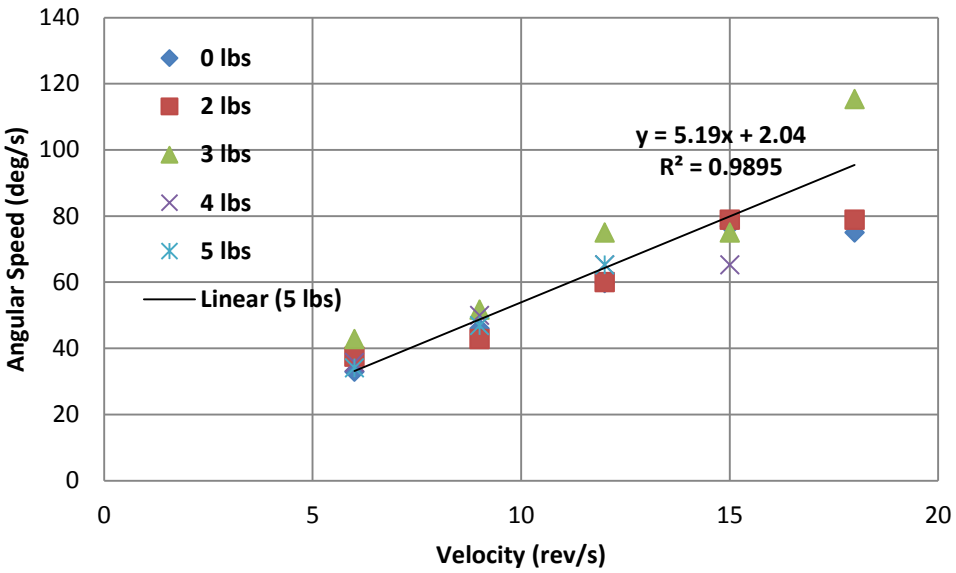

Figure 3.5 The angular speed of the bicep versus velocity for an acceleration setting of 30 rad/s^2. The trend line shows a near linear relationship for the 5 pounds. The angular speed was calculated using the degrees that the forearm traveled and the time it took to travel this distance. The velocity was set using LabVIEW.

At high velocities, the robot stalled when attempting to lift heavy weights such as the 5 pounds. It was determined that lifting 5 pounds is possible, as long as the LabVIEW program is set to a lower velocity (i.e.: 6 or 9 rev/s) or a lower acceleration (i.e.: 30 rad/s^2). It should be noted that there was a difference in the counter weight of the test and the actual forearm. The forearm weight of the old design was considerably lighter at 1.5 lbs so using the test bracket at 1.33 lbs was an adequate testing strategy. The actual hand that was developed after this test was 2.8 lbs. Other linear actuators were researched but the lower power density was not found to be adequate for the system if a shorter motor length was chosen. The slightly long length of the linear actuator was accommodated by redesigning the gears in the shoulder system. This linear actuator came at a lower cost than a custom built solution primarily due to the use of a stepper vs. DC motor.

The rotational motor in the previous design was a stepper motor from *Anaheim Automation*. It was able to achieve the desired range of motion but was larger than necessary because of the absence of the gear system. A stronger and lighter brushed motor option from *Maxon Motors* was

chosen to replace the stepper motor. The new rotational motor was selected based on the calculation of the required torque using Equations (1) – (3),

$$\alpha I_{zz} = \Sigma T \tag{1}$$

$$T_{gravity} = r * m * g * \cos(\theta) \tag{2}$$

$$\Sigma T = T_{motor} - T_{gravity} \tag{3}$$

where α is the angular acceleration, I_{zz} is the moment of inertia, T is the torque, r is the radius, m is the mass, g is the gravitational constant, and θ is the angle of the bicep at the point of highest torque. From these equations, Figure 3.6 was developed that shows the total torque as a function of time required for the current arm to rotate by 360 degrees.

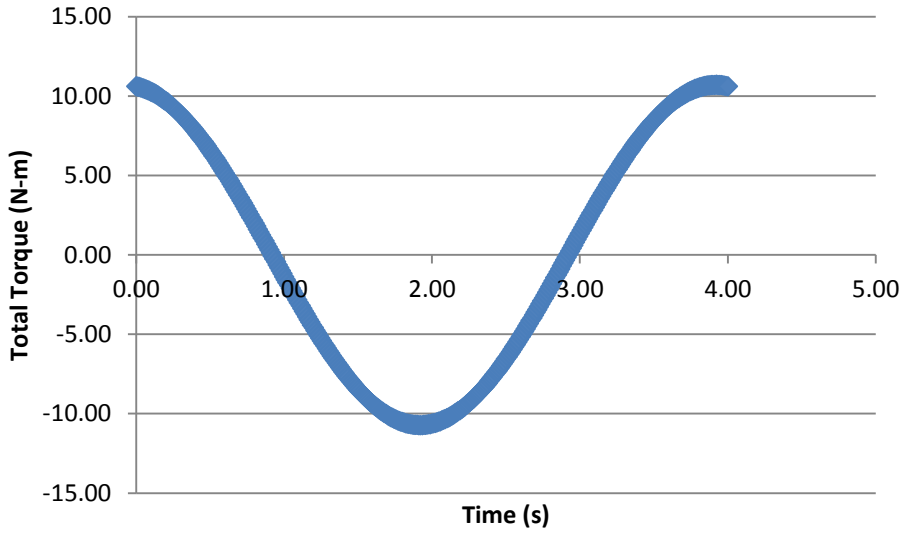

Figure 3.6 The total torque calculations (N-m) versus the time (seconds) it took for the arm to rotate by 360 degrees. The total torque includes the torque due to gravity and the torque due to acceleration.

The maximum allowable torque calculated for the rotational motor was 10.71 N-m. This value was used as a basis to select the new DC brushed motor. A rotational motor that met all of our design requirements was selected from *Maxon Motors* and was designed to attach to a gearbox

and HEDL encoder. The HEDL encoder produces pulse trains from electrical signals that are used to indicate the velocity, direction, and position of the arm. Due to system constraints, the encoder was not used but instead positional measurements from potentiometers were used for closed loop feedback control.

Upper Arm Structural Design

The guiding objective in the design of the upper arm was to achieve a more compact system while still maintaining the necessary DOF. Modularity of design was also required for repair and testing purposes. The main design change with respect to first iteration was using motor mounts to make connections to the supporting structures between the two motors. The linear actuator in the first model rotated about a pin connected to the shoulder joint. In order to eliminate the linear actuator's passive movement, the elbow joint was changed. In the second iteration, the linear actuator moved along a guided slot in the elbow which rotated the forearm circularly about the elbow joint displayed in Figure 3.7. Not only did the new rotational motor have a three stage gearbox incorporated with it, but a 2:1 gear ratio to rotate the upper arm relative to the shoulder was used to further amplify the 15 Nm of max torque supplied by the planetary gear. Both motors were fixed to their respective support structures mentioned below.

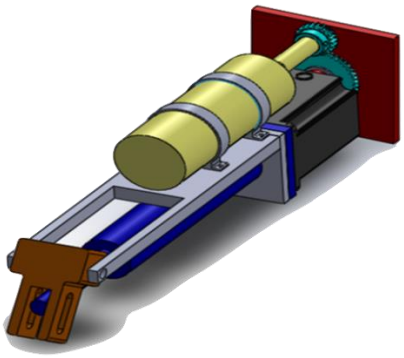

Figure 3.7 The second iteration for the upper arm with the following components: upper arm to shoulder attachment plate (red), the elbow joint (brown), the rotational motor (gold), elbow support structure (grey), the linear actuator (blue), and the linear actuator motor (black).

The design for the upper body went through several successive iterations due to different system complications. The initial elbow support on the upper arm, which was first designed to be one solid L-bracket required being separated into two sub-sections for machining purposes. The structural integrity of the elbow was also at risk which required the redesign of two separate elbow supports. Additionally, an individual component was placed between them to mount the rotational motor and isolate any lateral movement. The motor casing screws were used to mount the linear actuator assembly, the DC motor support and the elbow support pieces together. The final design is illustrated in Figure 3.8. Triangular truss structures were designed to distribute the load of the forearm on the elbow support structures. The FEA analysis was conducted in SolidWorks to calculate the maximum yield stress which was found to be approximately 8000 psi for the elbow support shown in Figure 3.9. The final supports decreased the range of motion so they were inverted causing the overall arm length to be increased. The elbow joint was also elongated and redesigned to allow for larger movement. The range of motion remained a higher priority than anatomical size when the elbow was redesigned.

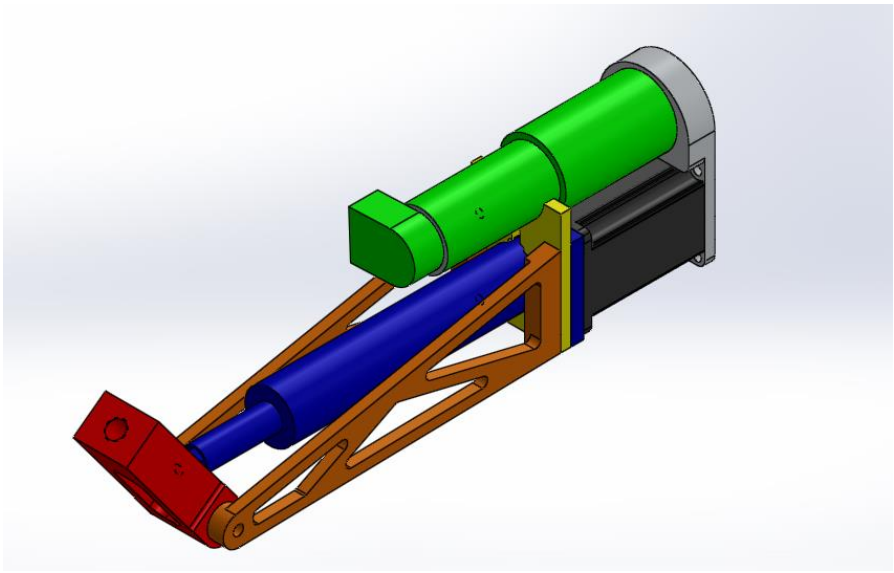

Figure 3.8 The final upper arm design. The new elbow supports are shown in brown and include triangular trusses for additional support. The red elbow joint was elongated to allow the linear actuator to retract and extend without interfering. The gray base plate was rigidly attached to both the DC and stepper motor, which then integrates with the shoulder assembly.

The base plate located on the top of the upper arm was also modified to enhance the rigid support in order to attach the rotational motor, linear actuator, and slewing gear. The slewing gears

allow for a rotation with nylon bushings of the entire assembly of the upper arm relative to the shoulder while also providing a fixed mounting point. Both slewing gears that are connected to the upper arm and chest had to be modified due to size and to simplify the assembly. Figure 3.10 illustrates displays the base plate with the custom slewing gear attached.

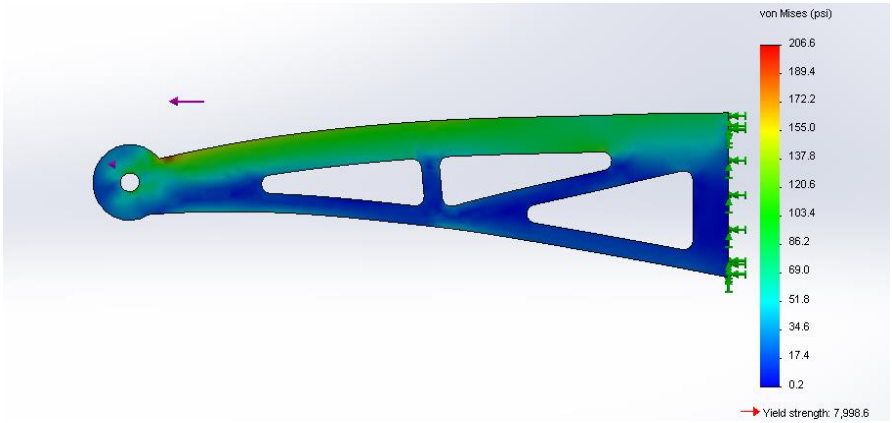

Figure 3.9 FEA analysis showing a color distribution of the stress resulting from the external load placed on the support. The maximum yield stress is approximately 8,000 psi.

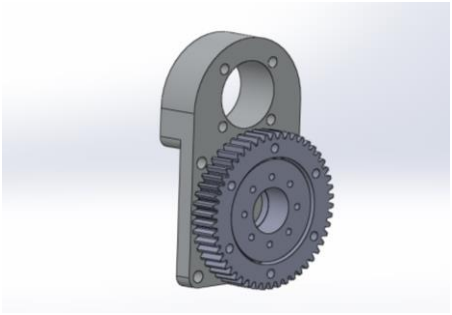

Figure 3.10 Shown is the base plate which integrates the rotational motor in the upper arm and the shoulder. The large gear is mounted to the base plate and the bearing allows the teeth to rotate freely.

The final upper arm design was functional, cost-effective, efficient, and achieved the desired range of motion and degrees of freedom. Each of the support parts were custom machined from 1060 aluminum as shown in Figure 3.11. The triangular truss structures provided the structural support between each motor and held the entire assembly together without adding more than 1 lb. of extra weight due to the truss design. The entire assembly can be removed from the

shoulder with 6 screws enhancing modularity for separately testing different code segments or in its entirety with the whole robot. Reusing the linear actuator from the old project saved cost and design time after it was verified to meet the requirements for lifting the desired weight of 5 lbs. This new design, with the removal of the passive actuation in the linear actuator, reduced the overall length by two inches. Due to the overall length of the linear actuator, the bicep was still longer than necessary for biomimetic validation. The new DC motor was more efficient solution to achieve the upper arm rotation due to the reduction in overall size of 30% and increased torque with the planetary gear head by 95%.

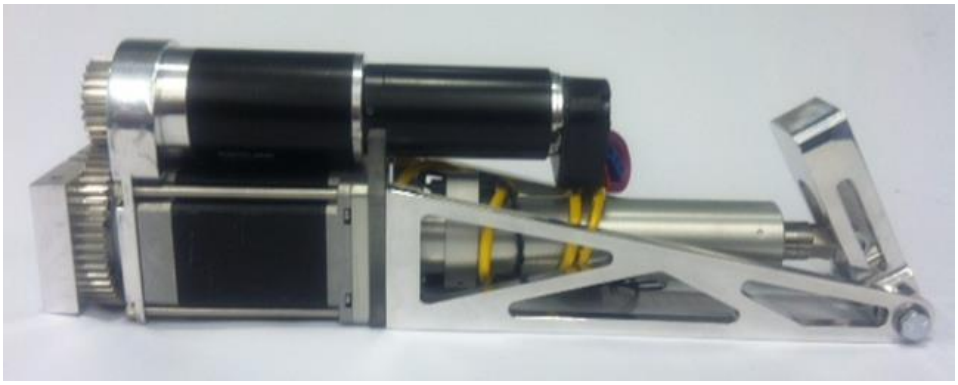

Figure 3.11 Shown is the final upper arm assembly. All manufactured pieces are made of aluminum for a lightweight design, and all the components were designed to be as compact as possible. The upper arm measures 12 inches in length and 2.5 inches in width.

Shoulder Design

The shoulder was one of the most challenging aspects of the upper body because of the 3 DOF located in a volume of about 420 cm^3 and the desire to have the capability for lifting 2.3 kg or roughly 5 lbs. Additionally, the design required the reduction of overall size and weight of the previous shoulder design in order to be anatomically correct. Therefore, the shoulder width was reduced from the previous design of 24 inches to 21 inches, which aligns well with a humanoid form mimicking a six foot tall male shown in Figure 3.12.

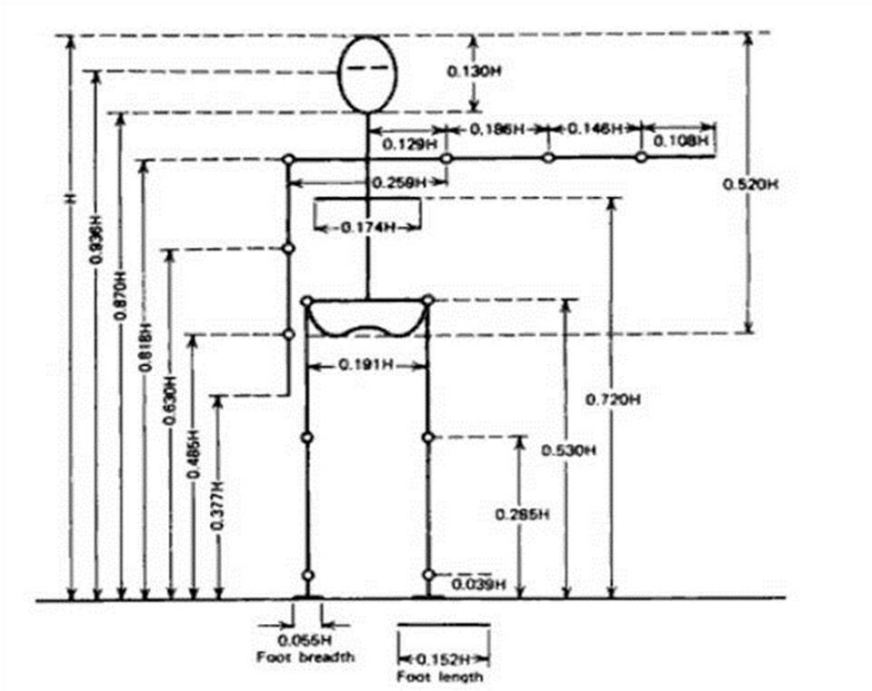

Figure 3.12 Based on the anatomical break down a human male at 6 ft. should have the shoulder span (joint to joint location) around 18.6 inches. Our final model measures 21 inches form outer to outer shoulder and 18.8 inches for shoulder span. (Winter, 1979)

Motor and Gearhead selection

New stepper motors were necessary to make the desired motion in the shoulder, reduce the overall weight and provide capability for lifting the entire upper arm and forearm. Research was conducted to find the best motors on the market that would meet the criteria for size, power, cost and weight. The final decision was to use NEMA 23 stepper motors and attach planetary gear assemblies for the required output torque of 4166 oz.-in. This design choice was primarily due to the lower cost compared to using professional DC brushless motors and harmonic drives. The 5818 Super Torque Stepper Motors, sourced from *Lin Engineering*, contain a bipolar parallel coil wound design with 2.8 amps per phase as shown in Figure 3.13. The high magnitude of amperage gives the motor alone a holding torque of 305 oz.-in before the gearhead. Inline planetary gearheads (023PNX) from *CGI* were attached directly to the stepper motor shaft and provided a max torque of 298 in-lbs. The trade-off is these gearheads add an extra 4 inches to the shoulder length and 3lbs to the weight of the system. Two gear ratios were chosen for the shoulders: a 28:1 gear ratio for

the abduction motion and a 70:1 gear ratio for the flexion motion. The difference in gear ratios was accounted through the bevel-pinion gear assembly which will be discussed later in this chapter.

Figure 3.13 Stepper motor connected with planetary gear head capable of providing a max torque of 298 in-lbs.

These motors were stacked vertically in the chest and secured to the spinal column of the robot with the supporting mounting frame. Flexion and extension motions were achieved by the lower stepper motor which rotates the entire shoulder joint with a 1:1 gear. Abduction and adduction motions were achieved by implementing a bevel gear and pinion into the shoulder as shown in Figure 56. To conserve the space in the shoulder and reduce the design complexity of a 3 DOF system, the DC motor responsible for lateral rotation was placed in the upper arm. Each degree of freedom was also outfitted with position feedback. Potentiometers and encoders were built onto the robot to establish a closed loop control system. Figure 3.14 shows the initial shoulder assembly.

The design uniquely couples the two motion of the shoulder driven by the stepper motors, unlike other humanoid robot designs that use motors at the actual joint location for abduction. A movement in the flexion or extension direction causes the bevel gears inside the shoulder to rotate the arm a third of the distance in abduction or adduction based on the bevel-pinion gear ratio of

3:1 shown in Figure 3.15. In order to subdue this feature, a software solution was used to account for the coupled motion of the abduction motion to the flexion stepper motor. The program actuates the abduction stepper motor to step backwards by 1/3 of the steps taken when the flexion stepper motor is in motion. The program also constantly confirms the shoulder is in the correct position using the potentiometer feedback and adjusts accordingly.

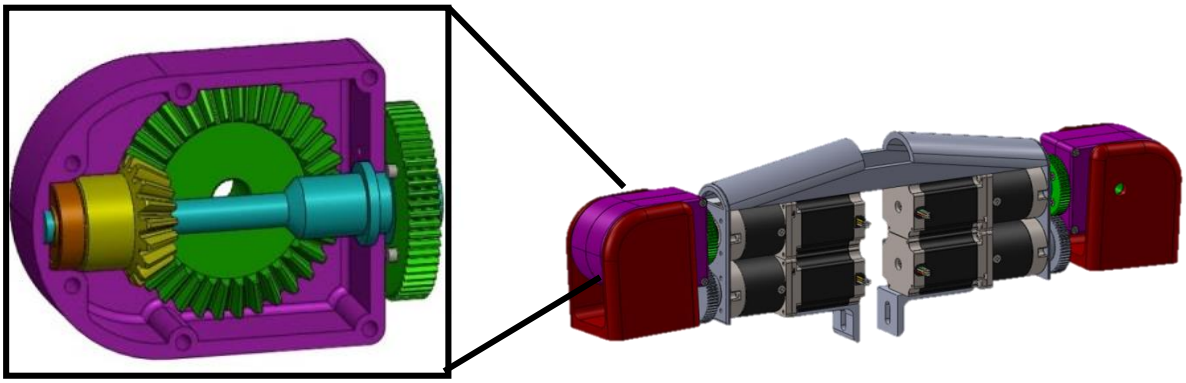

Figure 3.14 The initial design for the shoulder. The four NEMA 23 size stepper motors replace two larger and heavier stepper motors. A casing shown in red and purple was used to increase the realism of the design. The cut-out of the shoulder shows the gear system responsible for abduction/adduction for the new shoulder.

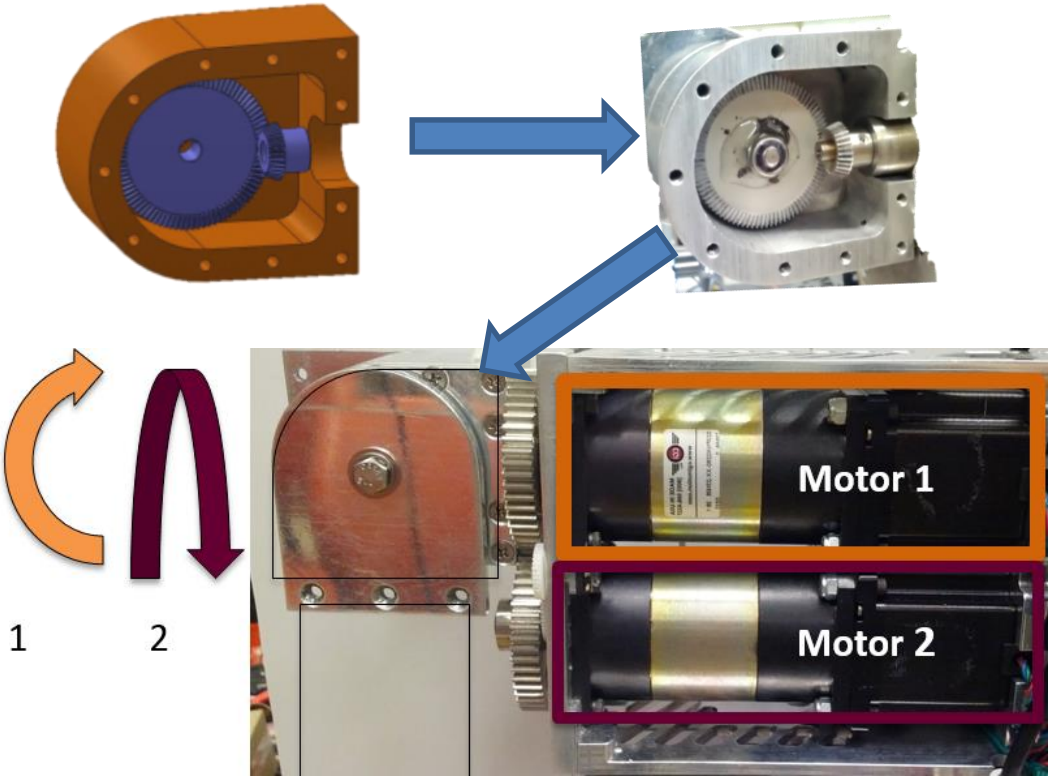

Figure 3.15 CAD design of the shoulder assembly, with a view of the internal gear system in the shoulder. The diagram details the layout of the motors in the chest that enable the abduction and flexion motions accomplished by their respective motors 1 and 2.

Reducing the weight of the shoulder area was achieved by changing the motors, support structure and support materials. The two large motors in the previous design with a weight of 12 pounds each were replaced. The new selected motors each with a weight of 5 pounds reduced the overall weight by over 50% per motor. The size reduction was possible by using a gear head attached to each of the stepper motors. Aluminum and carbon fiber were explored as possible material alternatives that offered enough strength to support the framing of the humanoid while also largely reducing the weight and still capable of being machined. The aluminum framing of the shoulder area replaced the heavy cold rolled steel which was susceptible to corrosion. The previous design also had large steel gears in the shoulder that substantially increased the weight. A new design was implemented which allowed for smaller overall gear sizes in a more anatomical geometry.

Slew Gears

The initial concept was to use a commercially available geared slewing bearings from *Igus* to provide flexion and extension movements in the shoulder joint while allowing the abduction and adduction movements to pass through the center of the slewing gear. However, the geared bearings were too large for the design. Thus, customized geared slewing bearings were manufactured with an off-the-shelf gear and 3D printed spacers were used to act as the custom bearing as shown in Figure 3.16. Tolerances were critical for a smooth fit with the 3D printed spacer that acts as a bushing between the two rotational parts. These bushings were used in the shoulder flexion as well as the bicep/shoulder rotation joint. They allow for the assemblies to rotate while being rigidly mounted to their respective ground frame.

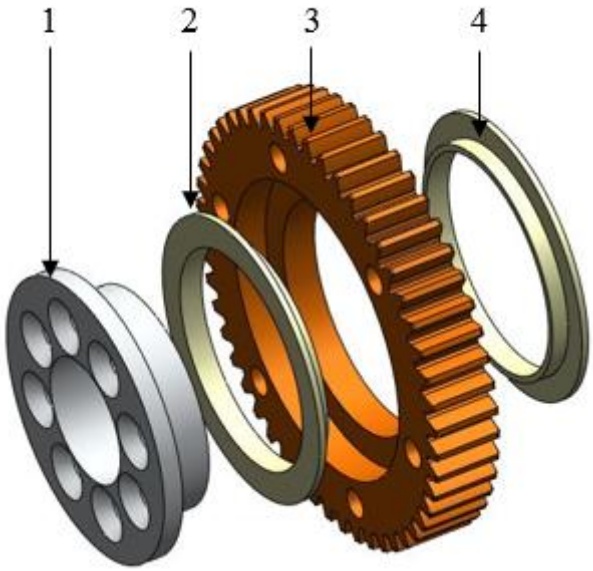

Figure 3.16 Slew bearing design with (1) connecting hub, (2) 3D printed bushing, (3) driver gear, and (4) 3D printed bushing

Shoulder Redesign

Multiple iterations of the shoulder design were necessary to make the assembly mechanically robust. The initial iteration used two small ball thrust bearings to distribute the load of the bevel gear onto the one bolt that held the entire arm assembly to the robot. The main issue was that when the arm would travel greater than 75° away from the body, the bevel gear would adversely loosen the single bolt holding it to the shoulder causing the entire system to crash into the torso shown in Figure 3.17 (a). Multiple methods were attempted to quickly repair the issue but epoxy and self-locking nuts were not the optimum solution as shown in Figure 3.17 (b). This design was reengineered with a more reliable solution that took advantage of needle thrust bearings, ball thrust bearings, radial bearings to distribute the force to the surrounding supporting shell, as well as multiple bolts to avoid the loosening issue.

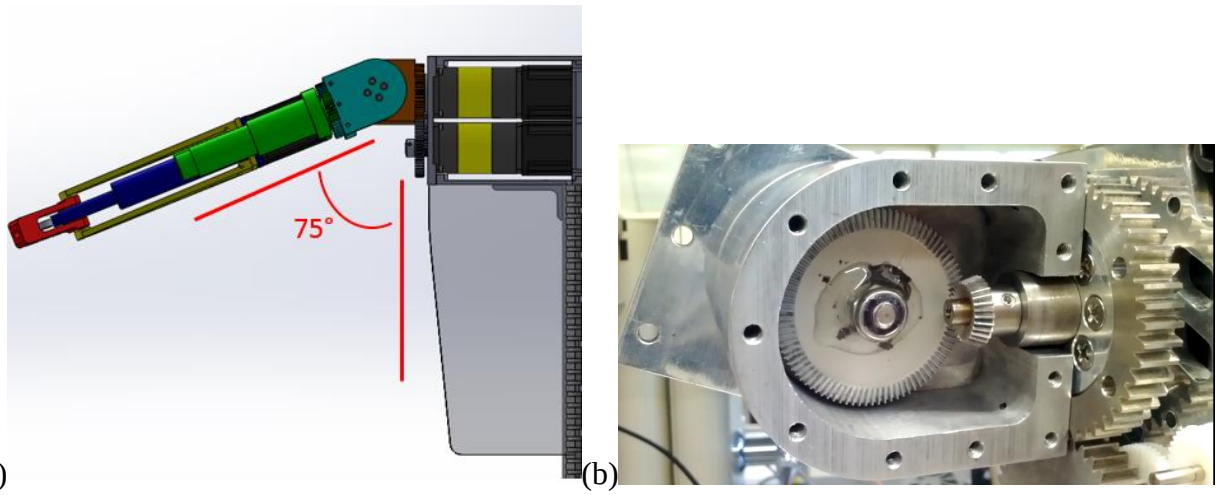

(a) (b)

Figure 3.17 (a) Max angle before single bolt loosened from internal gear and lost contact with the pinion gear. (b) Attempted to mitigate the issue with Epoxy and locking heck nuts

The shoulder redesign was necessary to incorporate positional feedback into the abduction motion as well as keeping the arm from coming loose from the assembly. The design challenge was to minimize the parts that needed to be machined and keeping the same shell thickness (Figure 3.18 (a)). Reduction of friction was also required to make the movements smooth and controlled. In order to put more bolts through the gear, a larger bearing was necessary to hold the system. A thrust bearing was still necessary because of the thrust force supplied by the beveled and pinion gear. The added benefit of increasing the bearing size was that it provided a larger surface area to support the higher lateral forces. Needle bearings also increased the surface area compared to ball bearings because of the larger rollers while still being relatively thin at 2mm in thickness. Two sets of thrust bearings were used in the final design between the outer shell and arm plate and the inner shell and beveled gear shown in Figure 3.18 (c). Radial bearings were also necessary for the potentially large radial loads from the front bolt holding the shell cover plate to the arm. A combination of radial and thrust ball bearings were used to mitigate any unforeseen issues on the front side of the shoulder covers shown in Figure 3.18 (b). Before machining the new parts and the shell pieces, a 3D printed version of the final parts was tested to verify that the multiple new bearings were within tolerance of the design shown in Figure 3.18 (d).

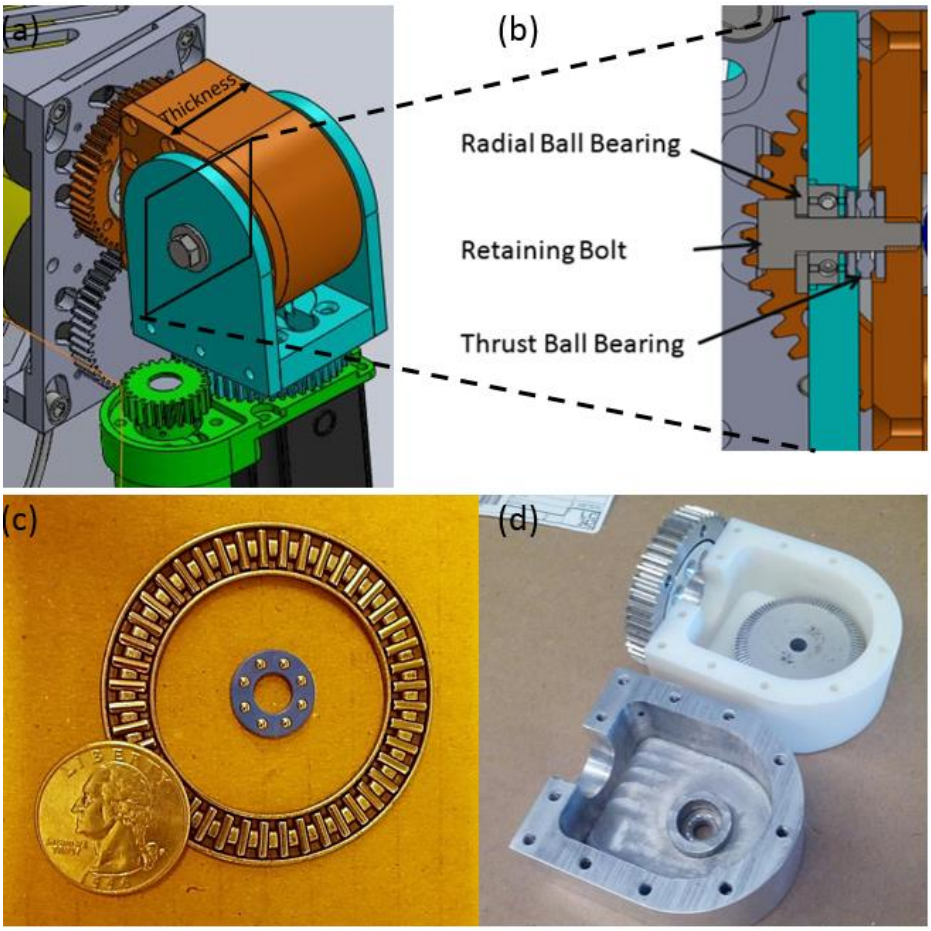

Figure 3.18 (a) Design constrains related to shoulder thickness. (b) Radial and thrust bearing between shoulder shell and outer arm plate. (c) Difference in size between needle thrust bearing and initial ball thrust bearing. (d) Rapid prototype of new shoulder design to check for tolerances before producing final version.

The potentiometer was redesigned to fit inside the shoulder assembly. The first design included a potientometer at each joint for closed loop control but the system was left on the outer face of the shell and was subject to potential damage from extreme conditions and errors in the loop. The new design optimized the placement of the potentiometer directly inline with bevel gear for direct access to the position of the joint. It was also encased in the shell cover for a more secure fit and cable management approach. 3D printed spacers were fabricated to secure the potentiometer relative to the shell and act as a bushing between the connection hub and the inner diameter of the shell. The final desing is shown in the exploded

Figure 3.19 and assembly Figure 3.20.

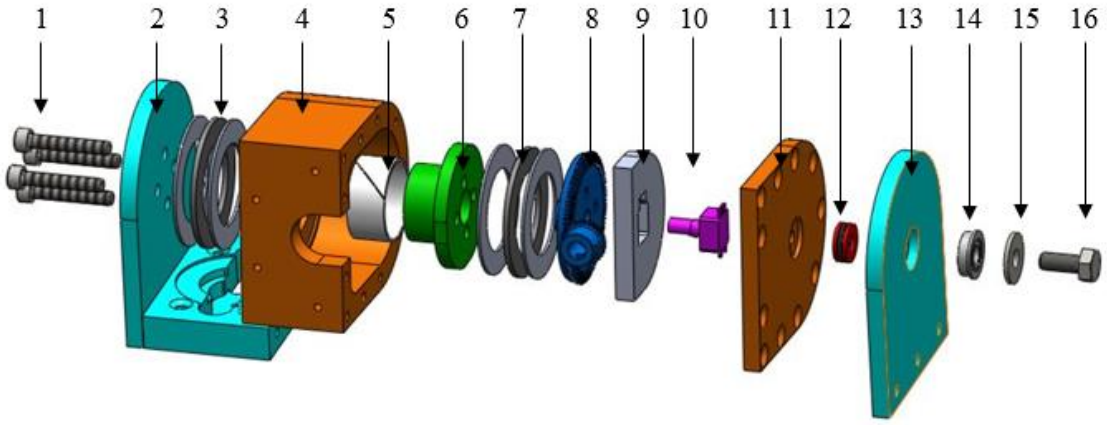

Figure 3.19 Exploded view of the final shoulder design with (1) hex retaining screws, (2) outer arm plate, (3) thrust needle bearing assembly, (4) shoulder shell, (5) 3D printed bushing, (6) connecting hub, (7) thrust needle bearing assembly, (8) bevel and pinion gear assembly, (9) 3D printed potentiometer holder, (10) potentiometer, (11) shell cover, (12) thrust ball bearing assembly, (13) outer arm plate, (14) radial bearing, (15) retaining washer, and (16) hex bolt.

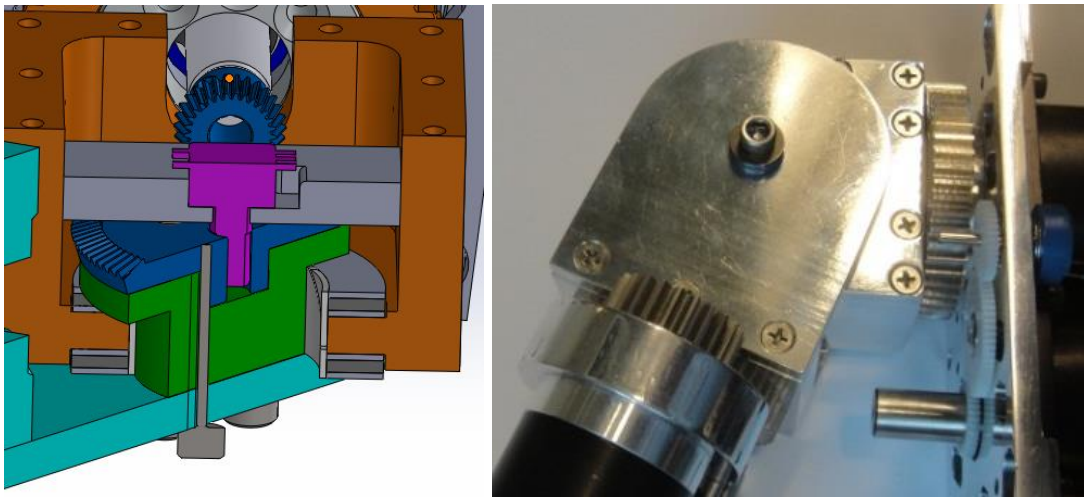

Figure 3.20 Rotated section view of assembled shoulder (left) and final assembly (right).

Conclusion

The upper torso objectives were met by reducing the overall weight and size, adding a third degree of freedom in the shoulder, and providing closed-loop feedback for all the motors. The overall weight of the torso was reduced by 5 lb for a total weight of 45 lb. This weight reduction is significant for any future application that will require mounting of the upper body on to a mobile platform. Additionally, the upper arms were reduced in length by 2 inches and width by 1.5 inches, providing a more realistic humanoid scale which is necessary to operate in a human environment. The overall width of the robot was reduced by 3 inches to 21 inches in comparison to the first generation. Much of the weight reduction was accomplished by using NEMA 23 stepper motors with gear heads rather than the previous NEMA 34K stepper motors without gear heads. The weight of each motor assembly was reduced by 7 lb by using the smaller stepper motors with appropriate gear heads while providing a max torque of 298 in-lb. Weight reduction was also accomplished by using 1060 aluminum instead of steel and removing the excess material in the structural design. The difference in size of the motors also allowed integrating two additional motor assemblies to provide 3 degrees of freedom, flexion and extension of the upper arm with the achievable ranges of motion shown in Table 3.1. Each joint incorporated a feedback system for all functioning motors. A potentiometer was mounted to each of the joints of the six stepper motors and two DC motors located in the upper body, all of which provided accurate feedback. The potentiometers were successfully incorporated into the coding of the robotic movements to ensure a robust and functional system.

	Human	Current Design
Forward Flexion	180 Degrees	180 Degrees
Extension	45-60 Degrees	180 Degrees
Abduction	150 Degrees	165 Degrees
Internal Rotation	70-90 Degrees	45 Degrees
External Rotation	90 Degrees	135 Degrees

Table 3.1 Current Design vs. Human Arm: Range of Motion

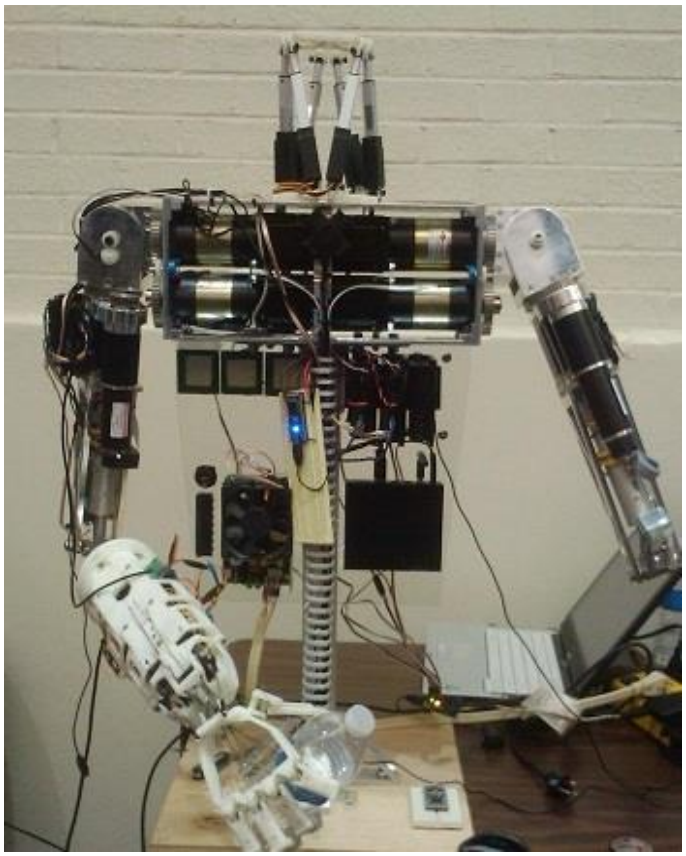

Figure 3.21 The final design of the upper body with the DART hand attached for gripping a water bottle.

Chapter 4: Kinect Integration

Introduction and Background

The Kinect device created by Microsoft is a technology for human user interface and currently marketed for the Xbox 360. It began to be used by researchers for developing variety of human – machine interfaces due to its cost-effective price and wide array of sensors. The Kinect was released in late 2010 and has since been one of the fastest selling consumer electronics reaching over 8 million units in 60 days (Alexander, 2011). Initially designed for enhancing the user interaction while playing games, the sensor captures human motion for controller free operation. Due to its low cost of around $100, many researchers began using it for robotic applications, computer interactions and other robotic systems. A numerous amount of "hacks" have led to Microsoft creating a Software Development Kit (SDK) to allow programmers to access the features and sensors with specific code packages. By allowing access to the low level sensor data, numerous projects and applications have been initiated mainly due to the open platform approach.

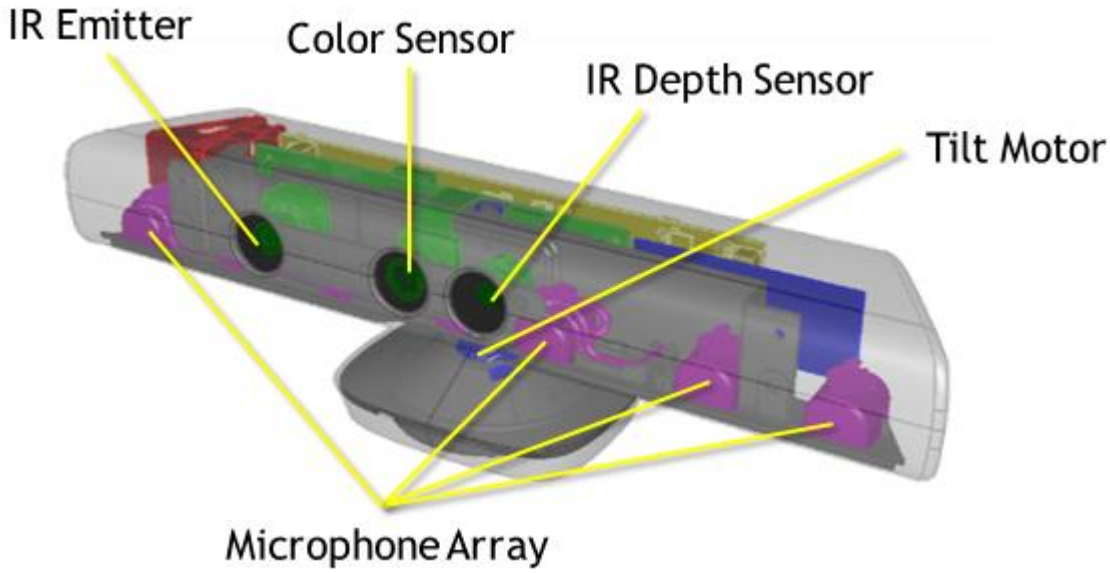

Figure 4.1 Kinect sensor showing internal components including the IR emitter and depth sensor responsible for capturing the skeletal data of a human. Under fair use policy (Microsoft, n.d.).

The Kinect has a multitude of sensor data including a 3D depth sensor, RGB image sensor and microphone array shown in Figure 4.2. The entire platform is built around the Prime Sense image processing chip. The Kinect acquires the data from the depth and image sensor and processes the skeletal data and facial recognition onboard before relaying all the information over USB to a host device. Also included in the device is a microphone array for voice recognition and audio direction. The base of the system is motorized for the device to tilt the image sensors in the pitch direction. The feedback is done by a 3-axis accelerometer.

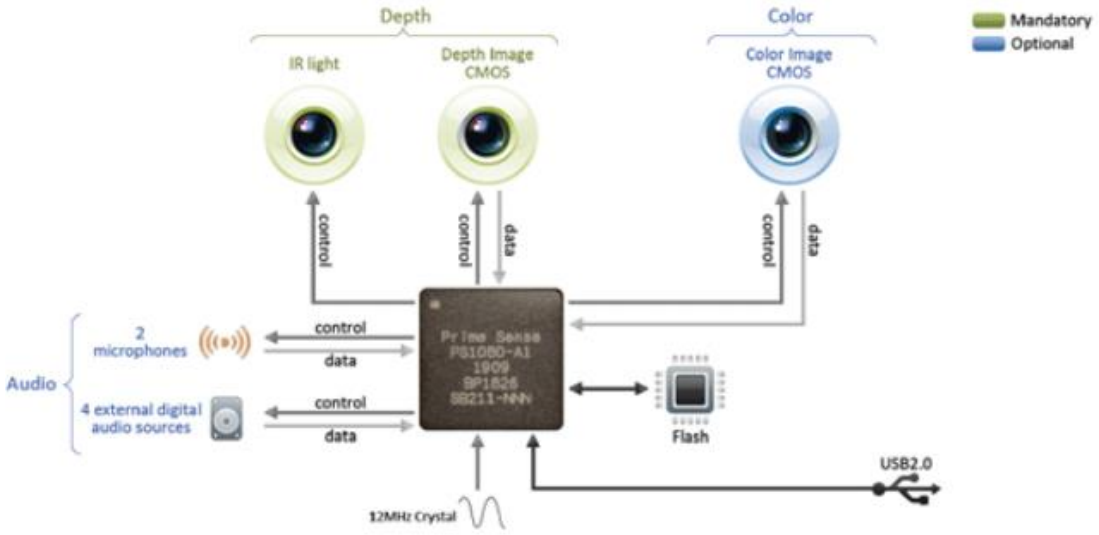

Figure 4.2 Sensor flow diagram showing communication to the Prime Sense chip and USB interface. Under fair use policy (Jordan Kuehn and Kevin Horecka, n.d.).

The primary uses in robotics platforms have been to integrate the image and depth sensor data streams for vision and mapping environmental surroundings. Other depth sensors on the market are priced around $20,000 which made integrating depth sensors too costly. Thus, the Kinect provides a great alternative for 3D depth data. The Kinect uses an Infrared (IR) dot matrix that is projected on the subject shown in Figure 4.3. The depth sensor tracks the changes between the dots in the matrix and calculates their distance relative to each other and the sensor. The depth sensor resolution of 640x480 is sampled at 30 fps. This generates a 3D depth map which can be

used for numerous applications such as Simultaneous Localization And Mapping (SLAM), object avoidance, and even dynamic tracking (RoborRealm, 2013).

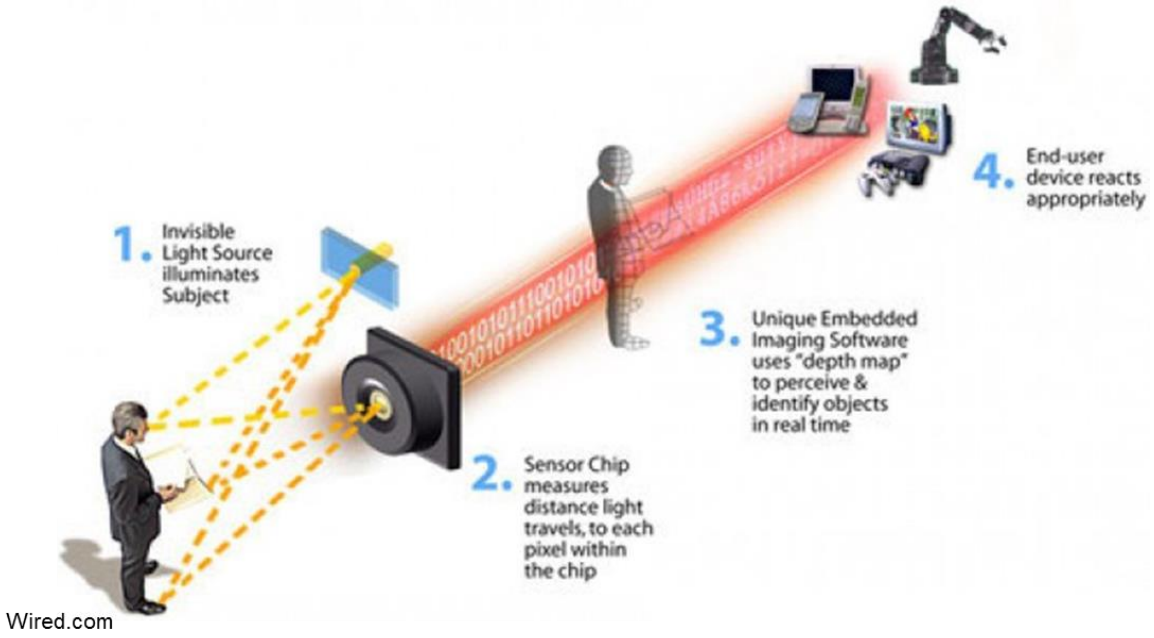

Figure 4.3 Kinect motion tracking is accomplished by: (1) projecting a matrix pattern of onto the subject, (2) sensing those points with an IR chip, (3) formulating those images into points, (4) and providing the 3D data to the user software. Under fair use policy (CARMODY, 2010).

The limitations to this technology are light sensitivity, placement and sampling rate. The depth sensor will not work well outdoors in direct sunlight because the IR data in the dot matrix will be oversaturated due to the sun's rays (RoborRealm, 2013). The field of view is also limited and the depth data cannot properly sense objects closer than a meter from the sensor. Finger positions are not efficiently tracked by the Kinect. The hand is represented as a final end effector position. Finally, the sensor has trouble mapping the skeletal frames if it cannot identify the head of the human from the rest of the body parts. This is typically not an issue unless the person is facing the Kinect sideways instead of head-on and objects are interfering with the depth of field.

The main contribution of this chapter was the ability to interface, track and manipulate skeletal points on a human subject. The significance of this ability is that the upper robotic body described in the previous chapter can be controlled using human-interaction approach as opposed to a keyboard or joystick. The Kinect has a built in algorithm that finds the head of a user and then

maps the joint locations of the torso, arms, hands, legs and feet in 3D space. This skeletal data is then correlated to each of the joints of the robot based on the potentiometer values shown in Figure 4.4. LabVIEW was the primary interface between these skeletal points and a specific wrapper was used to decipher the Kinect data and translate it into the joint locations used on the upper body embedded PC. The transfer of this data from the source PC with Kinect to the embedded PC on the robot was done wirelessly over the internet through a method called networked shared variables proprietary to LabVIEW. This allows for a human to interact naturally with upper body robot from a distant location.

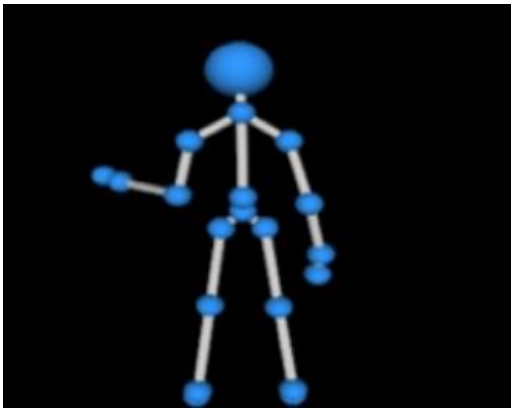

Figure 4.4 Skeletal tracking output of a single user displaying 20 data point in 3D space.

Teleoperation

Robotic control comes in different degrees of automaton as shown in Figure 4.5. Pure teleoperation is when the user has complete control over the robotic device from a remote distance. This allows for a direct interaction to the robotic hardware at a low level. Supervisory teleoperation takes a higher level approach while still giving the human operator control but removes the small details between operations. For example, instead of providing coordinates in the subroutines for each necessary step in controlling a robotic appendage, the desired positions are instructed by the user and the robot navigates those points based on inverse kinematics or built-in planed paths. Higher levels of autonomy are based upon specific tasks that the user picks and the robot decides the rest. An example is UAV navigation which is based on a desired location according to GPS coordinates. The operator of the UAV does not need to fly the vehicle nor give it step by step

direction but merely a way point that it should navigate to and the task is done autonomously. Total autonomy is when a robot makes all the decisions based on its environment without taking directions from a human Figure 4.5. A *Roomba* robot that is instructed to clean the floor every day at 2 pm and react to the environment around it without requiring human interaction or guidance is an excellent illustration of full autonomy.

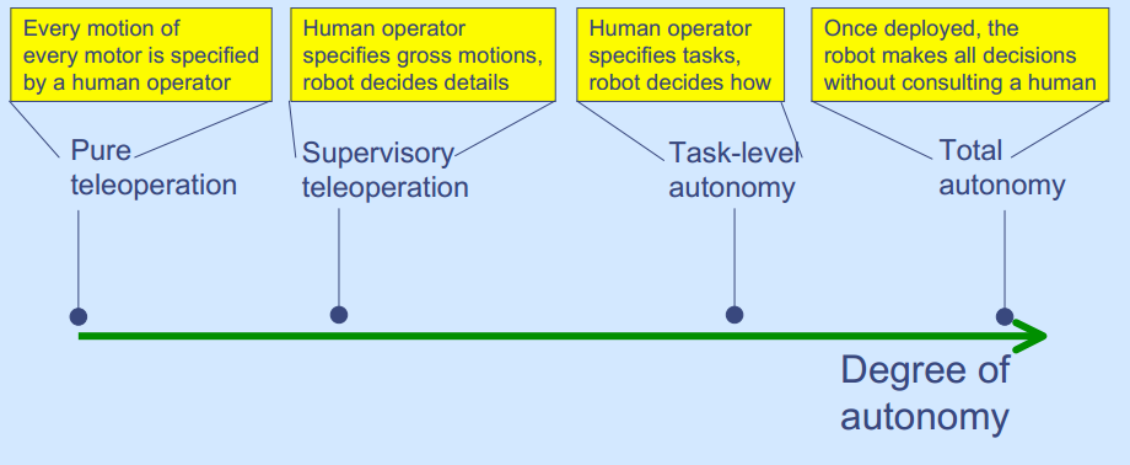

Figure 4.5 Degree of control from remote human control to full robot autonomy. Under fair use policy (Brooks, n.d.).

This project overlaps with pure and supervisory teleoperation in the spectrum of autonomy. The essential idea is to give the operator control over the robot through the Kinect interface. The Kinect samples the joint coordinates of the human subject by the IR sensor and builds a skeletal representation. These skeletal model points are used to determine the robots degrees of freedom (DOF). The upper body and hand have built-in limits to determine if the motion is in a feasible range of movement. If the desired motion can be achieved then the robot control system determines the appropriate motion otherwise it compensates by achieving the closest motion it can reach with regard to the desired position. This low-level autonomy offers some safety and robustness to the control scheme because the user does not have to be concerned if a movement will be excessive and cause damage such as having a robot arm swing into the torso cavity. This entire process is coordinated over the internet through a server with network shared variables.

Overall high level control diagram

The sharing of Kinect information and implementation on the humanoid robot requires two computers networked over the internet as shown in Figure 4.6. The host computer in the experimental setup is a laptop that is connected to the Kinect device and generates the 3D points for the skeletal data. Based on the specific points, joints are calculated and these angles are sent to the motors as theta angles. The client computer has a built in failsafe to ensure that if the connection between the computers is lost, then a global command to shut down the motors is initiated. The flow diagram resumes when a new connection is established and angles are received. Upon getting a new update from the Host connection, the motors use the low level programming shown in the last chapter to implement the positional control loops.

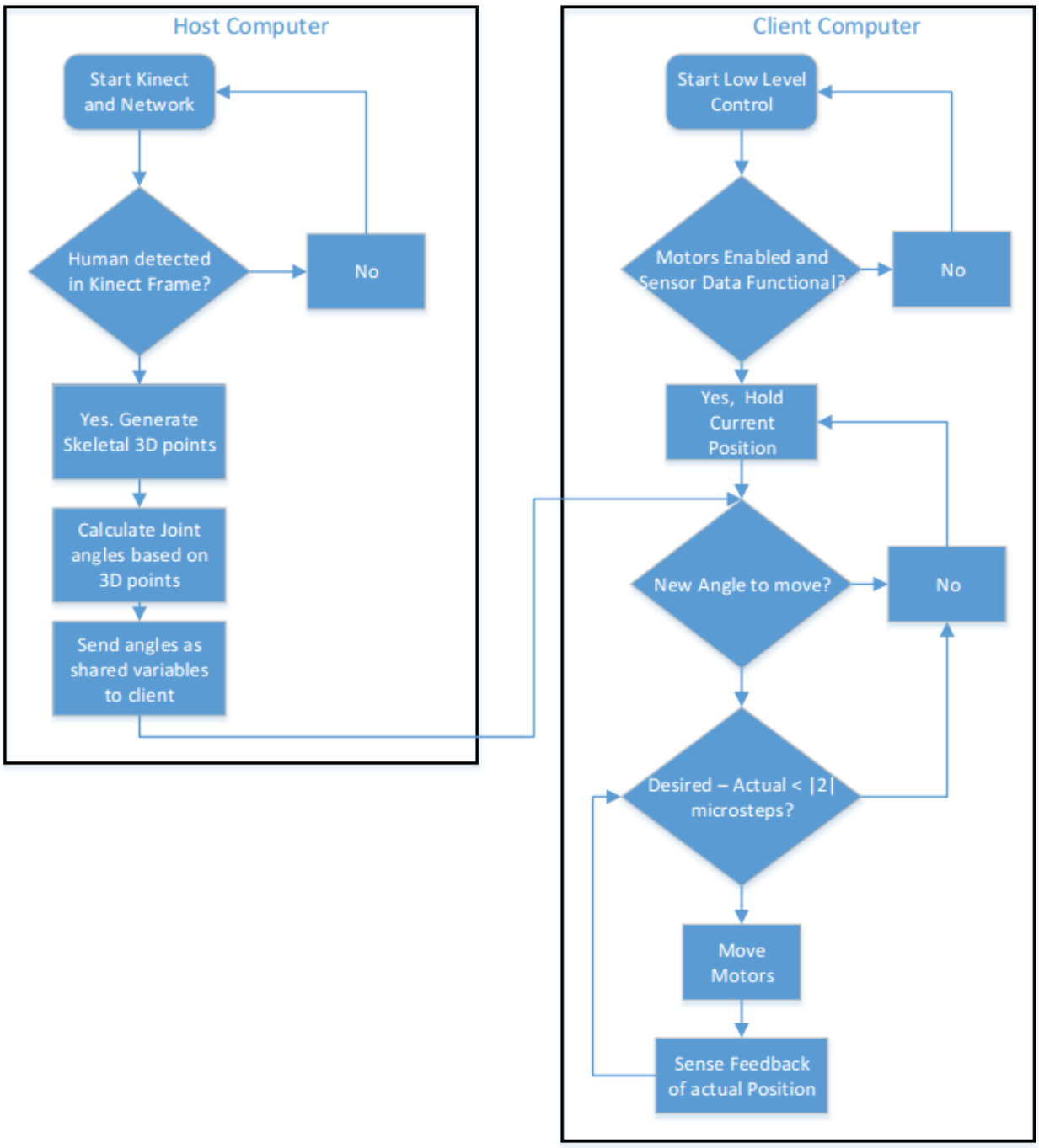

Figure 4.6 Flow chart of skeletal data transmission between the Host computer and Client computer.

Networking

The communication of the skeletal data transmission was done through the use of networked shared variable distribution shown in Figure 4.7. The VI running on the host computer stores each of the theta angles together in an 8 kB buffer. This buffer will be sent once filled or after a 10 ms delay, whichever comes first. The data is deployed to the client computer running a separate VI on the embedded PC of the humanoid. Since the value is not changed and redistributed, this communication is essentially one sided but the protocol does allows for updating the data sets. This is primarily useful for future situations when sending real time visual data back to the user after a given command is achieved on the client side.

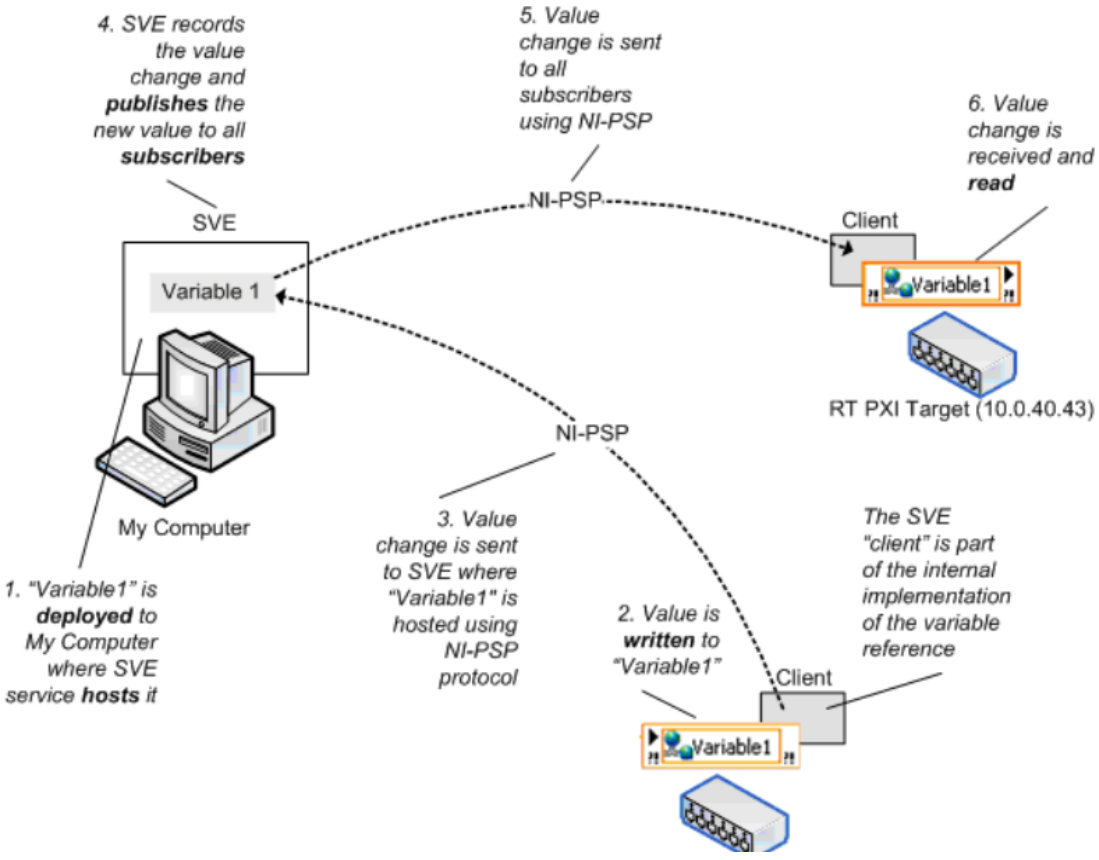

Figure 4.7 Example of network shared variable flowing between a host computer and multiple client computers. Under fair use policy (NI, 2012).

Wi-Fi was chosen as the standard for network communication primarily due to its widespread use, coverage in terms of range and adequate data rate as shown in Figure 4.8. Wi-Fi has been a dominating networking technology in the last decade because of the boom of personal computers and internet usage in the home. This makes implementing a wireless solution based on this technology highly cost-effective. Wi-Fi also has the capability of broadcasting a signal up to 600 Mbit/s outdoors with a range up to 250 m according to the latest IEEE 802.11n standards (IEEE, 2009). This will allow broadcasting joint angles for teleoperation quite simple within the desired application environment. Expanding the capabilities in the future to vision data will also be feasible based on the high bandwidth of communication. In the current version of the experimental set-up, the system was wirelessly connected to the local network where the shared variable engine was running underneath the network. Data transfer was almost instantaneous due to a lack of firewall or filters on the data.

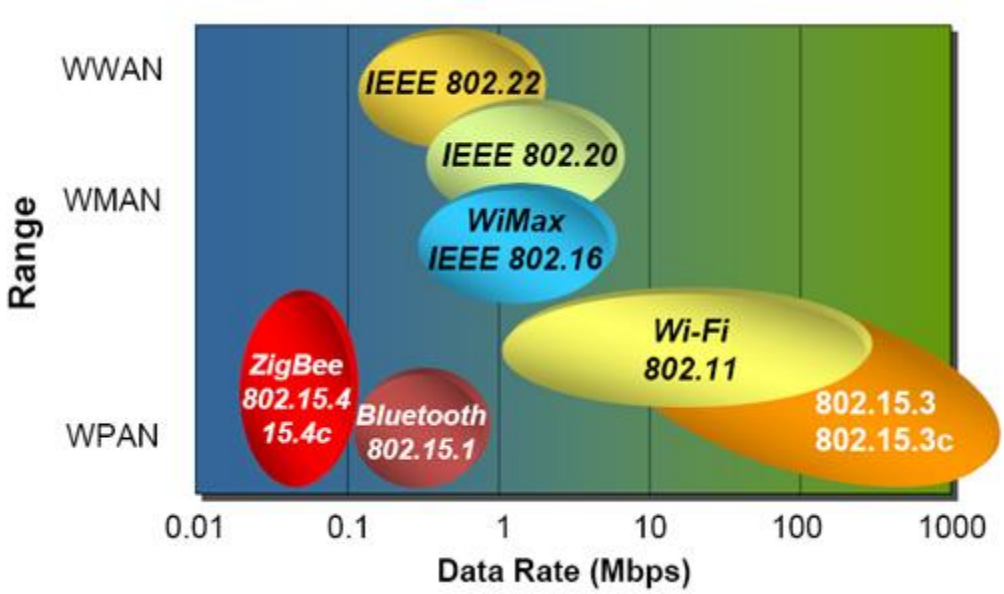

Figure 4.8 Different types of wireless protocols plotted in terms of their data transfer rate against their capability range. Under fair use policy (ANSolutions, n.d.)

Exogenous Full State Feedback Tracking with Kinect

A laboratory validation of using a Kinect with teleoperation for robotic control was completed. Elbow and shoulder flexion of a person were simulated using a double pendulum

model consisting of two degrees of freedom. Exogenous inputs from the skeletal data tracked from the user's right arm were used to control the position of both joints of the double pendulum. This experiment was completed using a LEGO NXT kit using two motors linking two segments and a Kinect tracking the shoulder, elbow, and hand of a subject.

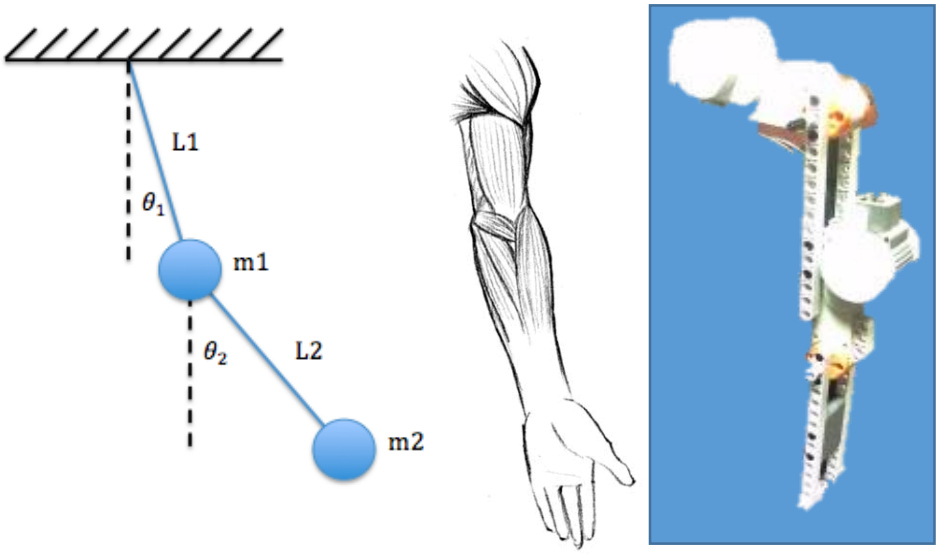

Figure 4.9 Double pendulum model (left) representative of the human shoulder and elbow joints (middle). Physical LEGO NXT model used in experiment (right).

This system was approximated as two point masses, m1 and m2, separated by lengths L1 and L2, pictured in Figure 4.9. Based on this theoretical system, the non-linear equations of motion can be derived using Lagrange's equations of motion to give:

$$(m_1 + m_2)L_1^2\alpha_1 + m_2L_1L_2\alpha_2\cos(\theta_2 - \theta_1) - m_2L_1L_2\omega_1^2\sin(\theta_2 - \theta_1) + (m_1 + m_2)gL_1\sin(\theta_1) = \tau_1$$

$$m_2L_2^2\alpha_2 + m_2L_1L_2\alpha_1\cos(\theta_2 - \theta_1) + m_2L_1L_2\omega_1^2\sin(\theta_2 - \theta_1) + m_2gL_2\sin(\theta_2) = \tau_2$$

There are several squared terms as well as trigonometric terms that make this system non-linear, and uncontrollable. To simplify these terms, the small angle approximation was applied to significantly reduce the complexity of these equations, giving

$$(m_1 + m_2)L_1^2\alpha_1 + m_2L_1L_2\alpha_2 + (m_1 + m_2)gL_1\theta_1 = \tau_1$$

$$m_2L_2^2\alpha_2 + m_2L_1L_2\alpha_1 + m_2gL_2\theta_2 = \tau_2$$

Notice that the terms of interest in these equations, α_1 and α_2 are coupled. However, this can be resolved by forming a linear system of equations, giving

$$\begin{bmatrix}(m_1 + m_2)L_1^2 & m_2L_1L_2 \\ m_2L_1L_2 & m_2L_2^2\end{bmatrix}\begin{bmatrix}\alpha_1 \\ \alpha_2\end{bmatrix} + \begin{bmatrix}(m_1 + m_2)gL_1 & 0 \\ 0 & m_2gL_2\end{bmatrix}\begin{bmatrix}\theta_1 \\ \theta_2\end{bmatrix} = \begin{bmatrix}1 & 0 \\ 0 & 1\end{bmatrix}\begin{bmatrix}\tau_1 \\ \tau_2\end{bmatrix}$$

Solving for $\alpha_1$and α_2 results in the following equations:

$$\begin{bmatrix}\alpha_1 \\ \alpha_2\end{bmatrix} = \begin{bmatrix}(m_1 + m_2)L_1^2 & m_2L_1L_2 \\ m_2L_1L_2 & m_2L_2^2\end{bmatrix}^{-1} * \left(-\begin{bmatrix}(m_1 + m_2)gL_1 & 0 \\ 0 & m_2gL_2\end{bmatrix}\begin{bmatrix}\theta_1 \\ \theta_2\end{bmatrix} + \begin{bmatrix}1 & 0 \\ 0 & 1\end{bmatrix}\begin{bmatrix}\tau_1 \\ \tau_2\end{bmatrix}\right)$$

Experimental Parameters

The basic parameters for the system were as follows: m1=80.7 g, m2=50 g, L1=.145 m, L2=.108 m, g=9.81 m/s^2. In the model, it was expected that the system acts as an ideal pendulum, meaning zero damping. However, each joint is composed of a motor which has a noticeable damping. As a result, a simple experiment was conducted in order to determine the magnitude of damping for both segments of the pendulum. A settling time of 5% follows the equation:

$$T_s = \frac{3}{\omega_n * \xi}$$

Since it was assumed that this is a linear system, the natural frequency for a pendulum becomes:

$$\omega_n = \frac{1}{2\pi\sqrt{\frac{L}{g}}}$$

Using these equations, the damping of each pendulum was determined by timing the settling time of each pendulum segment dropped from a reasonably small angle. The following damping terms were calculated from the experiment: $\omega_{n1} = 1.51$, $\omega_{n2} = .991$, $\xi_1 = 1.41, \xi_2 = 2.61$ which give a damping term in the theoretical control scheme.

Theoretical Controller Design and Performance

In order for the system receive a tracking input, an exogenous control input was used. Because the motors return position and velocity, it was possible to utilize a full-state feedback control scheme. The initial objectives for this controller were to be able to settle within 5% after 1 second while utilizing a peak control effort of .015 N-m (the limit of motors). However, this criteria was not met, suggesting a problem with the theoretical control scheme. Poles were selected using typical pole placement methods. From the initial selection, poles were placed further to the left in order to improve the settling time. However, it became quickly apparent that this theoretical system would not meet the expected requirements of 5% settling time to 0.5 radians within 1 second, while staying beneath the .015 N-m peak control effort. As a result, the requirements became 10% settling time within 2 seconds, without placing a hard limit on the control effort.

After some modification, poles were selected to be at -1 -5 -15-15i and -15+15i -30-60i -30+60i, which provided a reasonable settling time for both joints to 0.5 radians, while resulting in a peak control effort of roughly three times the maximum torque of the selected motors for the first segment. The results are illustrated in Figure 4.10.

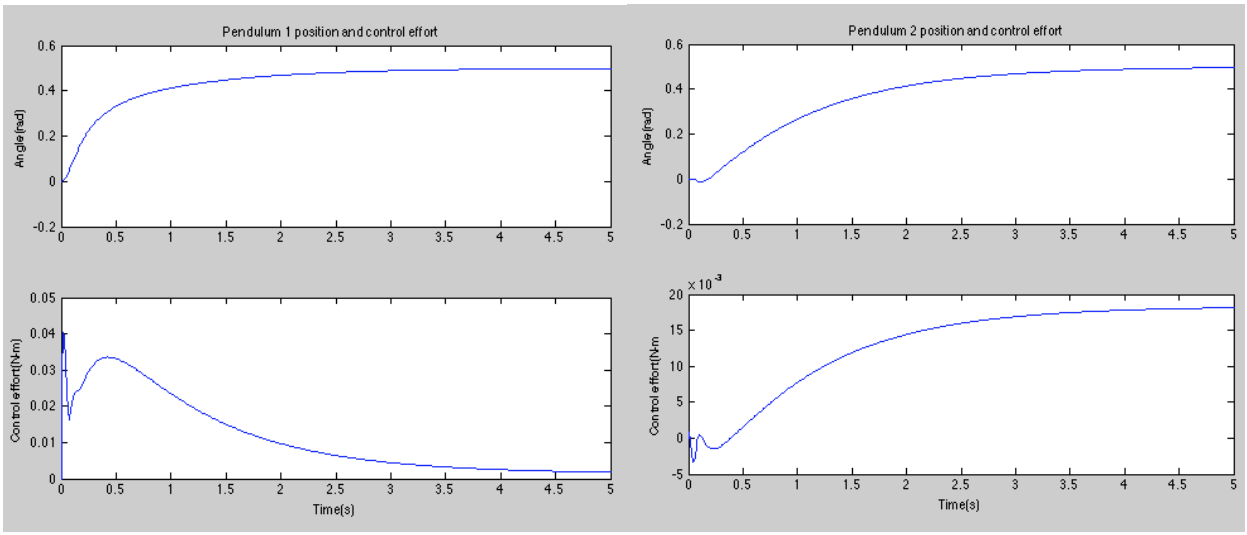

Figure 4.10 Angles and control effort for$\theta_1 = \theta_2 = .5\ radians$. Pendulum 1 is shown on the left and Pendulum 2 is shown on the right.

This process can be repeated using a different target angle for either segment. However, if the target angle is increased, there is a greater demand for peak control effort in order to reach this angle within the 2 second settling time, which can be observed for the system approaching 1.2 radians, where the system requirements for peak control effort go far beyond the capabilities of the motors shown in Figure 4.11.

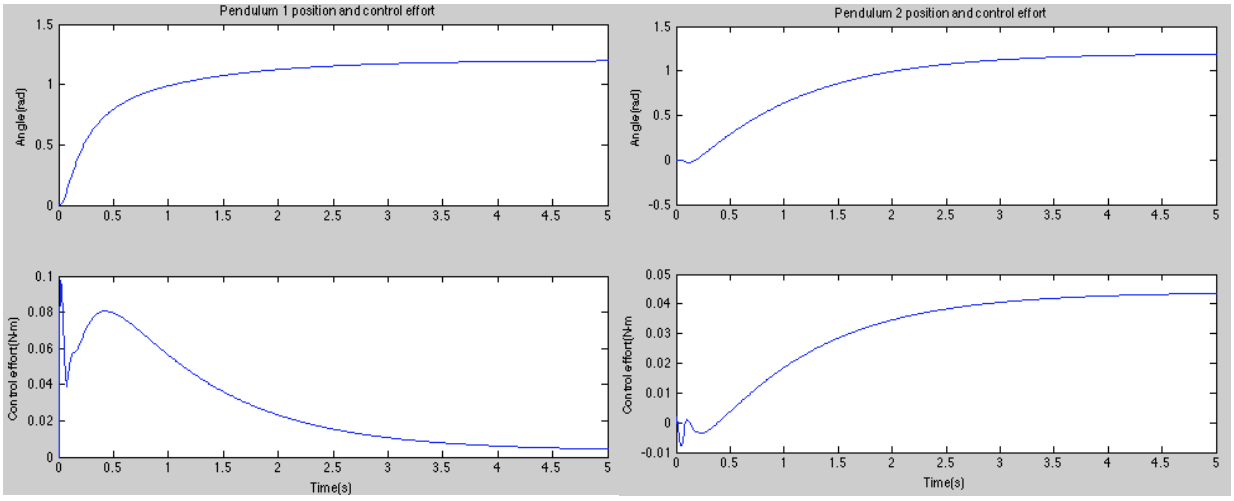

Figure 4.11 Angles and control effort for $\theta_1 = \theta_2 = 1.2\ radians$. Pendulum 1 is shown on the left and Pendulum 2 is shown on the right.

Several issues were observed in the control mechanism suggesting errors with the theoretical control scheme. In particular, it was noticed that when tracking a value for theta 2 (the angle of the second pendulum) set to 0, one would expect the segment to require a steady state input of 0, since the segment is effectively hanging loosely. However, in these situations it was observed that the steady state input was a large value. In this particular instance, 0.03 N-m, or double the allowable output torque of the motor. In general, peak control efforts required were significantly higher than expected, requiring almost triple the motor maximum torque to barely accomplish simple motions with long rise times. When basic open loop control was attempted for the physical system, it was observed that the simulated motions could easily be replicated with faster response times despite the previously estimated required peak torques.

Experimental System Hardware

The hardware of this system consisted of an Xbox Kinect sensor module and a Lego NXT brick with two motors. The Kinect tracked the human and mapped the joint locations as 3D points. The 3D points were sent to LabVIEW as tracked locations. Analytic geometry was used to map the line segments between the shoulder to elbow and the elbow to wrist in order to calculate the desired joint angle. The same method was used to calculate the angle of the shoulder relative to the torso and elbow respectively. These two mapped angles were then filtered due to the sensitivity of the system. Essentially, if the angle was smaller than 0 then the system filtered this as an invalid response to the joint angle tracked. It was observed that this sensitivity would occur when the system was confused by two locations having the same reference point. This usually occurred when the wrist was over the top of the shoulder. If the angle was less than zero, then the filter would feed back in the last good known location as the current position in order to keep it from losing power to the motor. These angles were stored as local variables for both theta 1 and 2. The angles were then inserted into controller and output by the NXT to the motors.

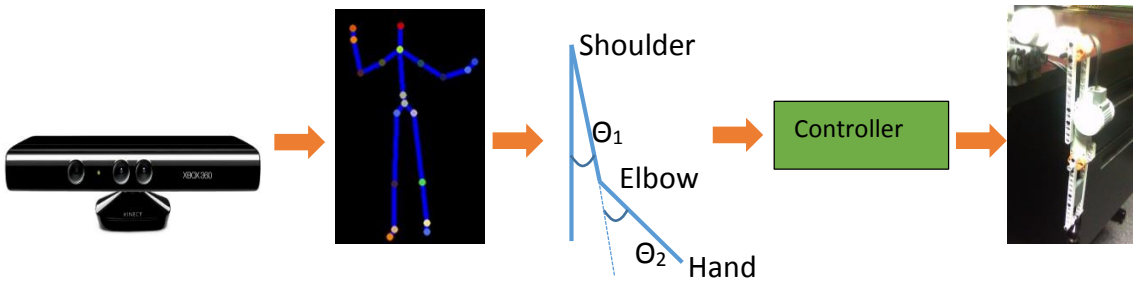

Figure 4.12 Control diagram showing the flow of information from the Kinect to the experimental setup.

The software for the proposed algorithm was simplified as an exogenous input with the assumption of no noise for full state feedback was used in the model. The system takes the desired input of each theta as an exogenous input. This R matrix (2x1) is subtracted from the reference angles Y (2x1), measured from the encoder of the motors. This produces an E term for error between desired and actual angles. The error is integrated and becomes the X_i term. This is then multiplied by Gain Integral G_i (2x2) term to give a new 2x1 input matrix term U_i, related to error. This term is subtracted with the input from the full state feedback input U_o which is derived from the multiplication of the gain matrix of the full state (2x4) and the states X (4x1). These two inputs are subtracted and are converted to Torques 1 and 2 for motors. From this point the motors move and a new actual theta one and two are recalculated. An example of the block diagram used for our controller is shown in Fig. 4.13.

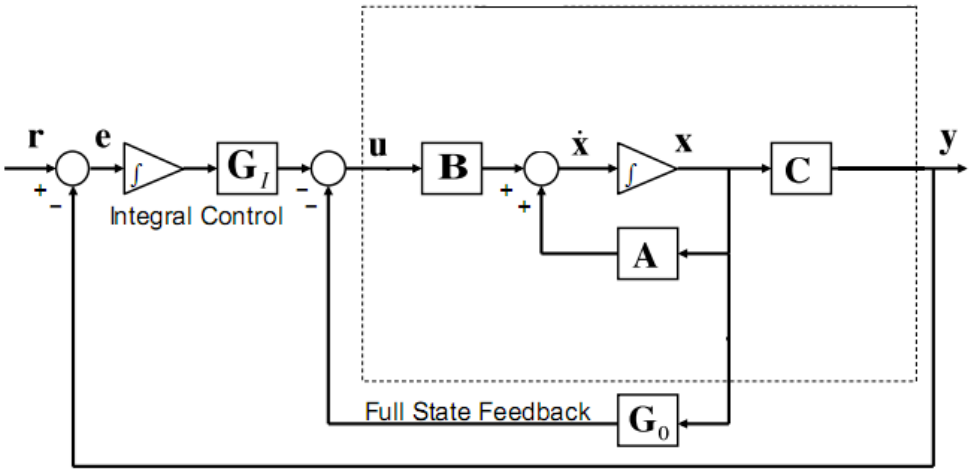

Figure 4.13 Exogenous input controller block diagram.

Final Implementation and Results

The integrator was removed and replaced with a much simpler proportional controller to drive the system. The system was able to track both theta 1 and 2 from the Kinect with a time delay of approximately 0.2 sec. By default a double pendulum system is non-linear and was modified to operate within the bounds of a linear control scheme. However, to linearize this system, it was assumed that the angles of the pendulum would remain small. Despite this nonlinear issue, this control scheme was used to manipulate a double pendulum to fairly large angles. As a result, this system would be expected to encounter significant errors as these angles increased between the theoretical and actual results. It is recommended that future investigations of this topic implement a non-linear controller in order to improve accuracy of the model.

In terms of the existing controller, establishing a cost function in order to better determine the pole placement would be a wise decision, as the attempted pole optimization proved to be inferior to the brute force pole placement method, which leaves some ambiguity.

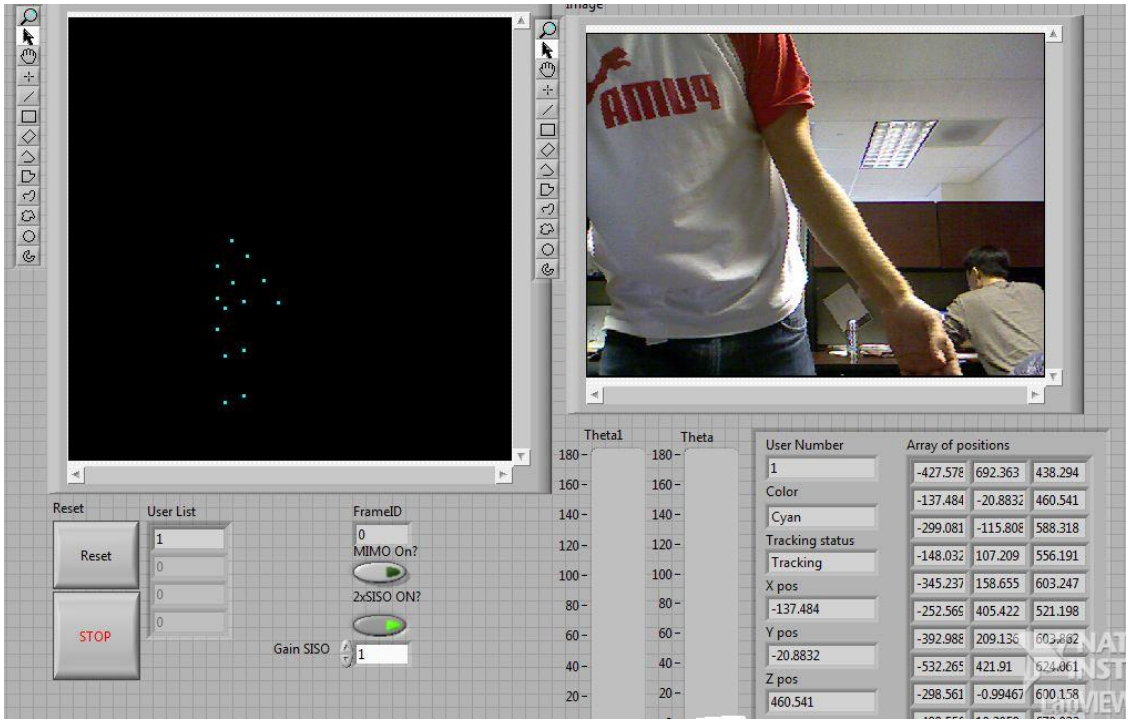

Figure 4.14 The front panel of the VI created for the experiment is tracking the right arm of human and relating the angle of theta 1 to the elbow and theta 2 to the shoulder flexion.

Chapter 5: Humanoid Robot Control

The control of the upper body was split into two sections containing the theoretical nonlinear control and the actual control implementation. Due to the nonlinearities, the assumptions made in the simple Kinect experiment in Chapter 4 could not be avoided. A nonlinear controller was developed for theoretical analysis of the 4 degrees of freedom in the upper arm and shoulder of the humanoid robot. Future modifications need to be made to the controller in order to be effective for the actual system. Until then, the system is functional based on a positional controller with control loops arranged for SISO operations. Implementing the nonlinear controller will address the issues present when coupling the motions in a MIMO configuration.

Nonlinear Theoretical Control

Overview

The upper body humanoid robot had 3 degrees of freedom at the shoulder that provided flexion, abduction and rotation as well as a 1 degree of freedom at the elbow joint that provided extension. The bottom stepper motor initiated the gear system and rotated the orange shoulder assembly around the Z1 frame to provide the required flexion. The top stepper motor was directly in line with a bevel gear system that extended through the orange shoulder assembly and rotated the blue shoulder assembly. The top stepper motor provided the abduction about the Z2 frame and caused the shoulder to move away from the body. The final shoulder rotation was actuated from the green DC motor and rotated about the Z3 axis. This pivots around the blue assembly and rotated the lower arm and elbow joint. The linear actuator in the upper arm extended the elbow by forcing the red joint away from the body. Analysis was conducted at the tip of the linear actuator to reduce the complexity of going from a rotatory stepper motor to linear translational motion and back to a rotational motion. These frames can be observed in Figure 5.1.

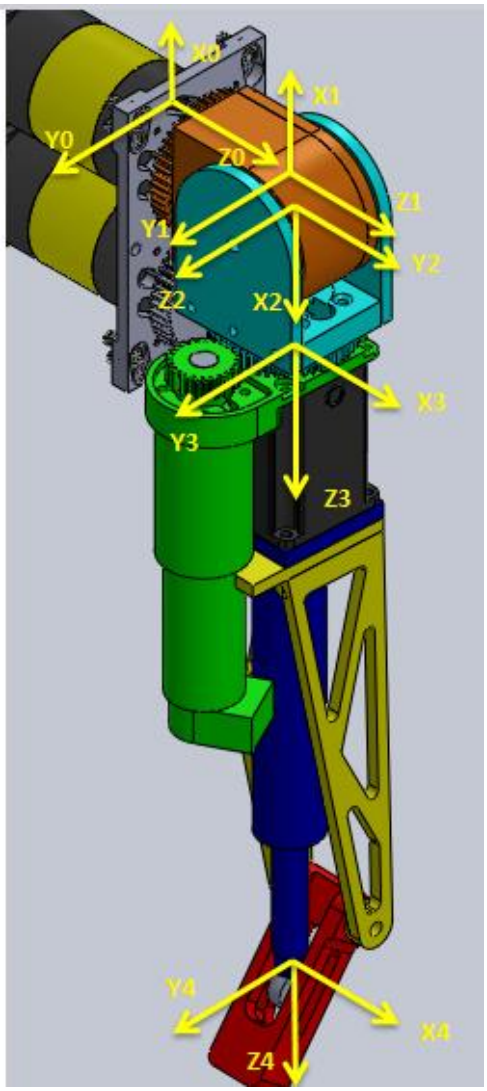

Figure 5.1 Degrees of freedom with their corresponding frame axis in yellow. The first and second frame should be aligned about the Y1 axis but were offset to reduce confusion in the figure

Denavit-Hartenberg Convention

The Denavit-Hartenberg (DH) convention is a set of parameters necessary to place reference frames between subsequent links in a robotic kinematic chain. These parameters are used to build a transformation matrix associated to each prismatic or revolute joint in the chain. The transformation matrices are generated from two translations parameters and two rotation parameters. In Figure 5.2, $\boldsymbol{\theta}$ represents the joint angle about Z_A with respect to the common

perpendicular that is made with X_B, D is the distance between the initial frame A to the intersection of the common perpendicular of X_B with Z_A, A is offset length from the base frame to the second frame along X_B, and $\boldsymbol{\alpha}$ represents the twist around the X_B frame. Based on the convention only these four parameters are necessary to relate the A frame to the B frame.

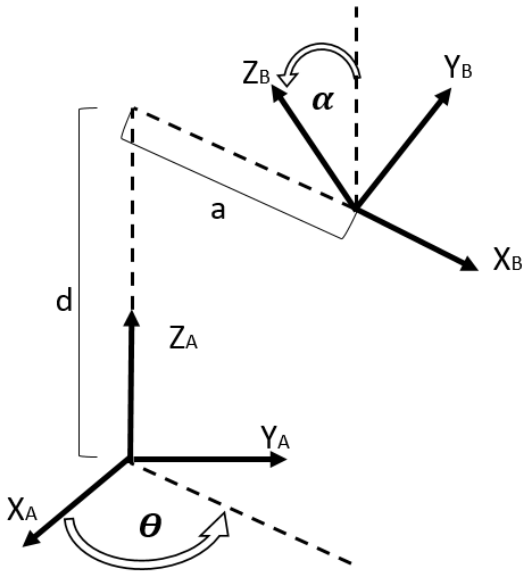

Figure 5.2 The four parameters necessary to relate two frames are: the joint angle $\boldsymbol{\theta}$, link offset d, link length a, and link twist $\boldsymbol{\alpha}$.

Based on the DH convention and the frames shown in figure 5.1, the following parameters represent the three rotational joints and one translational joint in the system.

	a	d	$\boldsymbol{\alpha}$	$\boldsymbol{\theta}$
1	7 mm	54.45 mm	0	$\boldsymbol{\theta}1$
2	0	60.8 mm	$-\boldsymbol{\pi}/2$	$\boldsymbol{\theta}2$
3	251.8 mm	0	$\boldsymbol{\pi}/2$	$\boldsymbol{\theta}3$
4	0	d(t)	0	0

Table 5.1 DH parameters for the joints relative to figure 5.1

Each of the parameters is used in the transformation matrix which is represented by the 4x4 matrix:

$$Translation\ (a) = \begin{bmatrix} 1 & 0 & 0 & a \\ 0 & 1 & 0 & 0 \\ 0 & 0 & 1 & 0 \\ 0 & 0 & 0 & 1 \end{bmatrix}$$

$$Translation\ (d) = \begin{bmatrix} 1 & 0 & 0 & 0 \\ 0 & 1 & 0 & 0 \\ 0 & 0 & 1 & d \\ 0 & 0 & 0 & 1 \end{bmatrix}$$

$$Rotation\ (\alpha) = \begin{bmatrix} 1 & 0 & 0 & 0 \\ 0 & \cos\alpha & -\sin\alpha & 0 \\ 0 & \sin\alpha & \cos\alpha & 0 \\ 0 & 0 & 0 & 1 \end{bmatrix}$$

$$Rotation\ (\theta) = \begin{bmatrix} \cos\theta & -\sin\theta & 0 & 0 \\ \sin\theta & \cos\theta & 0 & 0 \\ 0 & 0 & 1 & 0 \\ 0 & 0 & 0 & 1 \end{bmatrix}$$

Combining the rotation and translation components through matrix multiplication resulted in the following transformation matrix:

$$Transformation\ Matrix = \begin{bmatrix} Rotation & Translation \\ 0\ \ 0\ \ 0 & 1 \end{bmatrix}$$

$$= \begin{bmatrix} \cos\theta & -\sin\theta\cos\alpha & \sin\theta\sin\alpha & a\cos\theta \\ \sin\theta & \cos\theta\cos\alpha & -\cos\theta\sin\alpha & a\sin\theta \\ 0 & \sin\alpha & \cos\alpha & d \\ 0 & 0 & 0 & 1 \end{bmatrix}$$

Moments Of Inertia

The setup included the following assumptions: no friction was present in the system, all actuator dynamics were neglected, no gear slippage or backlash, and no limitations on the control. Each assembly was rigidly fixed and there was no room for movement between the joint locations. The weight of the bolts was neglected for the mass and inertia calculations. Although it was possible to model the system with ideal dynamic inversion with most of the parameters shown in Table 5.2, a smooth switching controller was chosen in order to compensate for any small neglected weight or uncertainty found in the system. The parameters for each of the respective links are shown in Figure 5.3, 5.4 and 5.5. The mass of the fourth link was held at 0.1 kg at the tip of the linear actuator. The model of the third link of the upper arm neglects the motor weight, thus manual measurements for the weight found the third link to be 2.04 kg. The center of mass for this link remained correct.

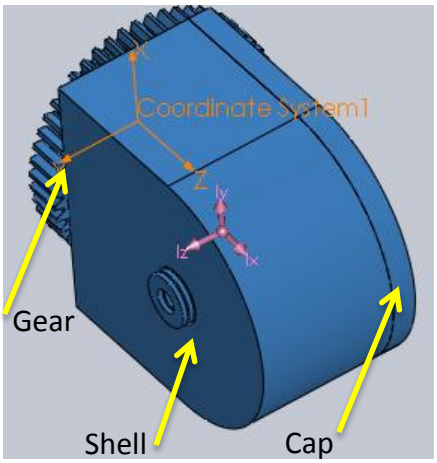

Figure 5.3 Shoulder assembly 1. The rotation happens about the coordinate system but the location of the center of mass was slightly offset from being in line with the Z0 axis. This was because the shell and cap of the system were not aligned around the center of the rotation of the gear.

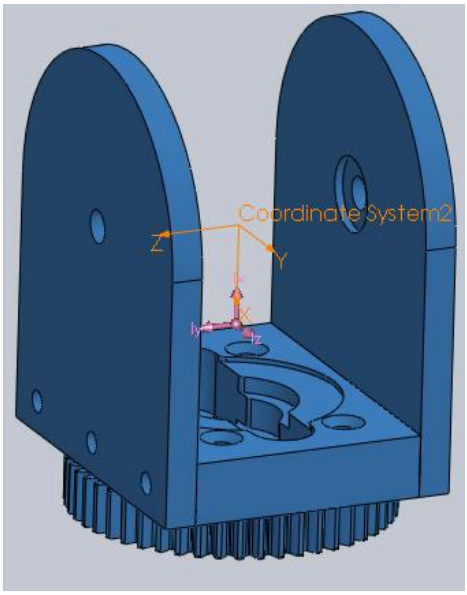

Figure 5.4 The second assembly of the shoulder was the outer shell and lower slew gear that were rigidly fixed as one unit. The rotation happened at the center of the top hole based on the internal bevel gear of the previous assembly. The location of the center of mass was in line with the axis of rotation and offset along the x axis by 20mm.

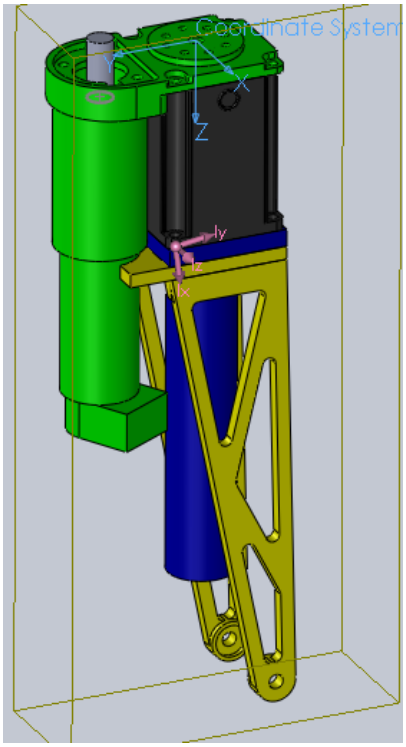

Figure 5.5 The upper arm portion was a combination of a DC motor shown in green, stepper motor shown in black, the rest of the linear actuator in dark blue and the supporting structure in yellow. Due to the motor weight, the center mass was shifted higher in the upper arm.

MOI (grams * m^2)		
Ixx	Ixy	Ixz
Iyx	Iyy	Iyz
Izx	Izy	Izz
Shoulder Moments of Inertia		
1.161069	0	0
0	1.234009	0.13519
0	0.13519	0.292829
Outer Shell Moments of Inertia		
0.273088	0	0.000038
0	0.461773	0
0.000038	0	0.414712
Upper Arm Moments of Inertia		
0.013185	0	0.000023
0	0.012708	0.000238
0.000023	0.000238	0.000922

Table 5.2 Moments of Inertia for the shoulder, outer shell and upper arm.

Approach

Initially, the system was modeled as an ideal dynamic inversion controller. This was done because the majority of the terms for the system were known. The dynamic inversion used a proportional and derivative gain on the tracking error and the derivative of the tracking error as the controller. These values were concatenated as the new controller in velocity with a parameter error outputs the required torque to the open loop system. The open loop implements the torque values for each of the individual motors and outputs the velocity and position. The setup assumes that there is a 10% error in parameters for the length and mass units of the system. This error should eliminate some of the assumptions with respect to the experiment conducted using the small angle assumption and issues with backlash in the hardware setup.

Figure 5.6 a and b showsthe dynamic inversion and open loop control respectively. The desired position was set to 1.5 radians for each of the rotational motors and 1.5 m for the linear

actuator. It should be noted that the translation and rotation were plotted on the same graph to show the convergence to the desired values. The initial velocity and desired positions were set to 0. The initial conditions for the system were at 0.01 rad and 0.01 m for the rotational and translational joints.

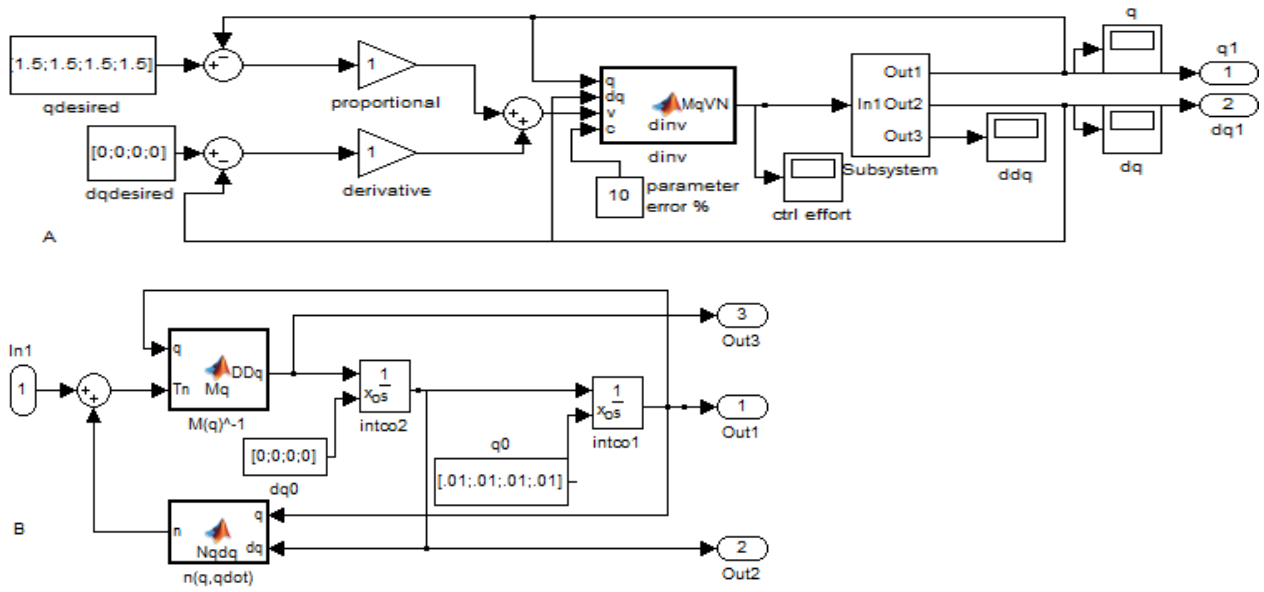

Figure 5.6 (A) The closed loop dynamic inversion of the controller with gain values for the position and velocity, parameter error and feedback from the open loop system. (B) The open loop system, that given a desired torque, outputs the correct position to each of the respective joints.

A range of gain values were chosen to see how the system reacts to different G1 and G0 inputs. The gains shown below were 1, 3, 5, 10, and 20. Gains of G0 = 20, and G1 = 5 were also tried to see if this had a different effect on the system. Figure 6 below illustrates the flexion, abduction, rotation and elbow extension with each of the different gain values.

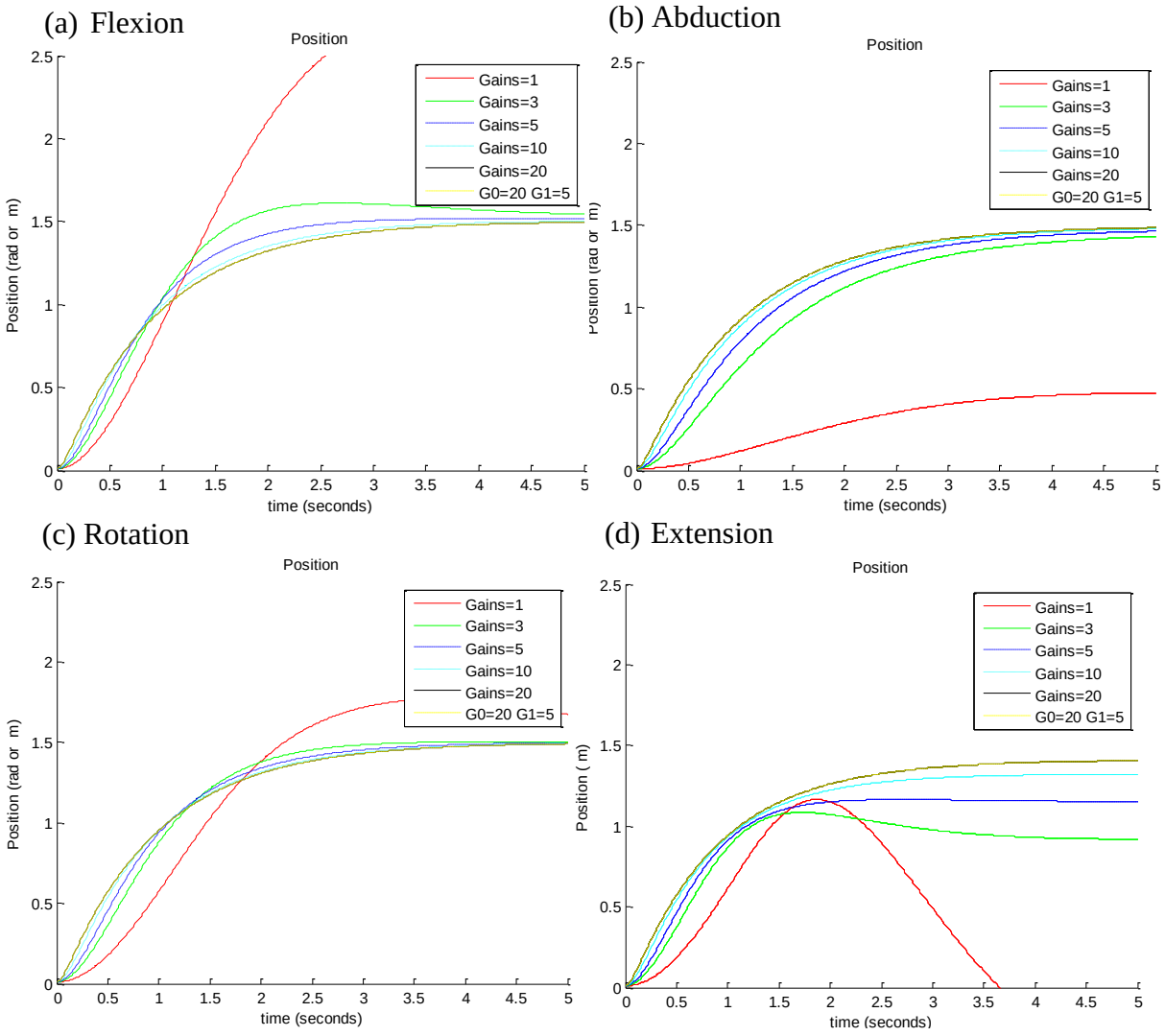

Figure 5.7 (a) Flexion of the shoulder, (b) Abduction of the shoulder, (c) Rotation of the shoulder, and (d) the extension of the elbow. Each graph is shown with the outputs for gains 1-20. Gains at 1 do not reach their desired position or overshoot past the position. Gains at 3 sometimes converge to the right value and for other portions of the system are undershot. The rest of the values do a decent job at converging to the desired location. Notice how there is little difference between the black and yellow plot. This shows that at a high G0 value of 20. The G1 has little effect on the overshoot.

Figure 7 has the same parameters for the control effort ast that for each of the graphs of flexion, abduction, rotation, and elbow extension.

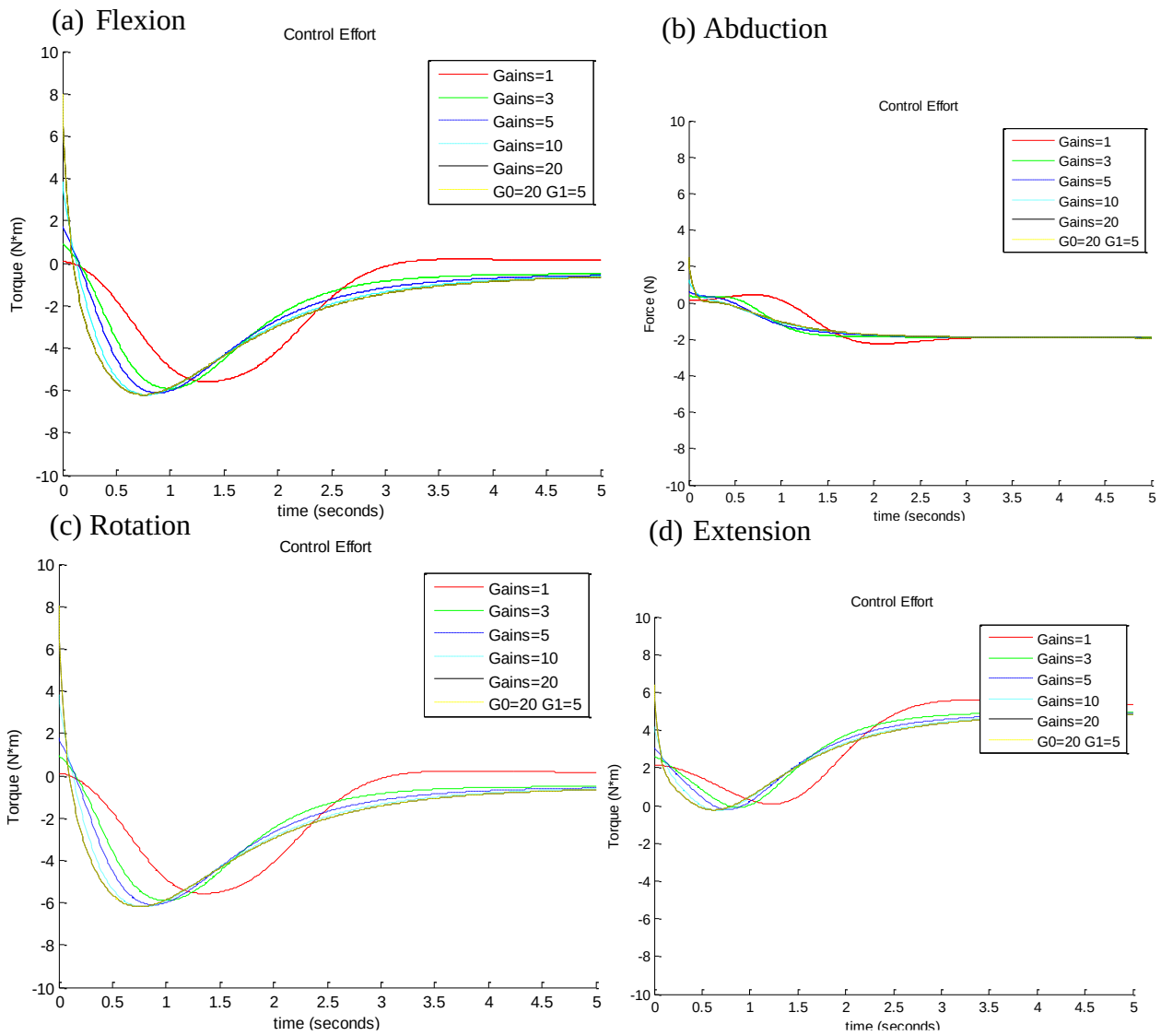

Figure 5.8 The control effort for (a) Flexion of the shoulder, (b) Abduction of the shoulder, (c) Rotation of the shoulder, and (d) the extension of the elbow. Each graph is shown with the outputs for gains 1-20. The higher the gains the less time it takes to settle but the more intital control effort it takes in terms of power. Notice again how there is little difference between the black and yellow plot.

After additional tuning, ideal gain values were selected that best fit the overall system. The G0 was set to 18 and the G1 value was set to 6. This allowed the system to converge quickly with minimum overshoot and decent control effort. Figure 5.9 (a) and (b) show the resulting plots.

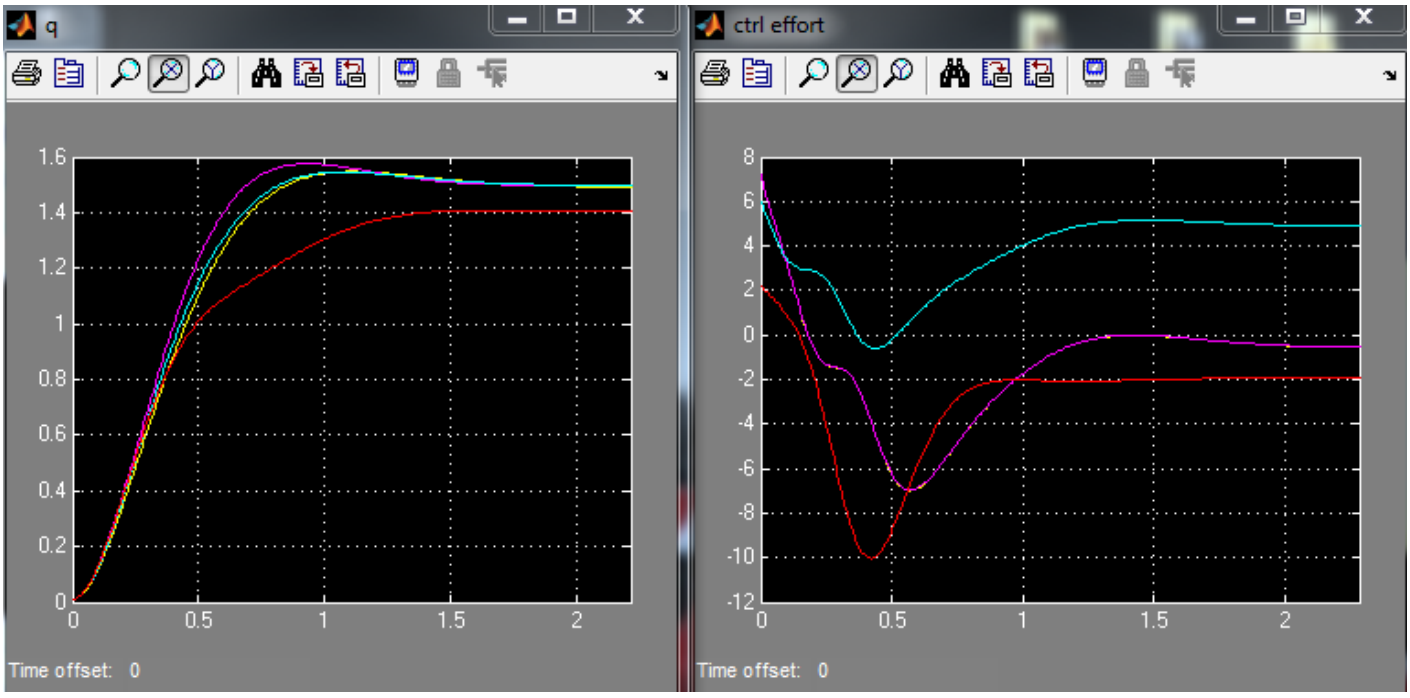

Figure 5.9 (a) Position output of dynamic inversion with initial conditions of 0.01 and a desired location of 1.5 with 10% parameter error. The error affects the elbow extension joint the most shown in red. The Flexion (yellow), Abduction (purple) and Extension (blue) all converge to the desired location of 1.5. (b) The control effort of the system shows different spikes of torque that will be discussed later.

The smooth switching controller was based on the dynamic inversion of the past tests. The inputs of epsilon and K had to be tuned to provide the optimal performance. The K constant of the new control input for U was the first to be tuned in order to be determine the best value for a parameter error of 10%. The new controller with the U input, dynamic inversion and open loop is shown in Figure 5.10. The position for each link and control effort for the system can be seen in Figure 5.11 and Figure 5.12

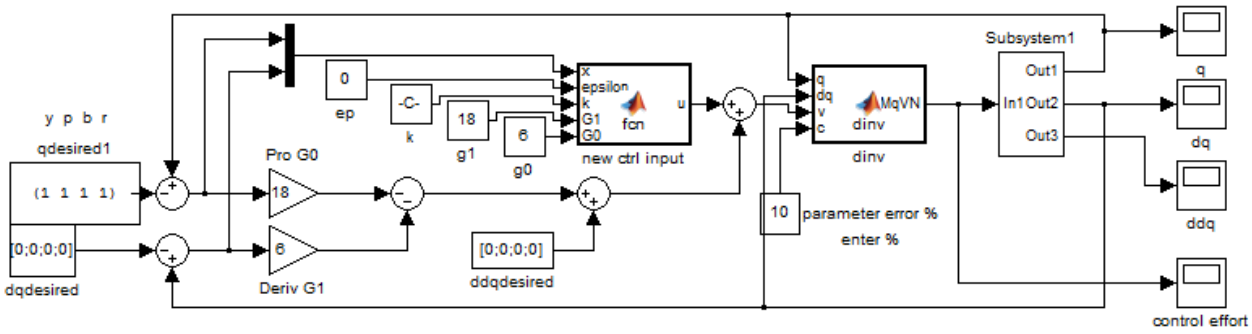

Figure 5.10 Switching control with U as the new control input to the dynamic inversion for the outer loop. The gain values stayed constant at G0=18 and G1=6 as well as the initial conditions of 0 for position and velocity. K was varied from .001 to 30.

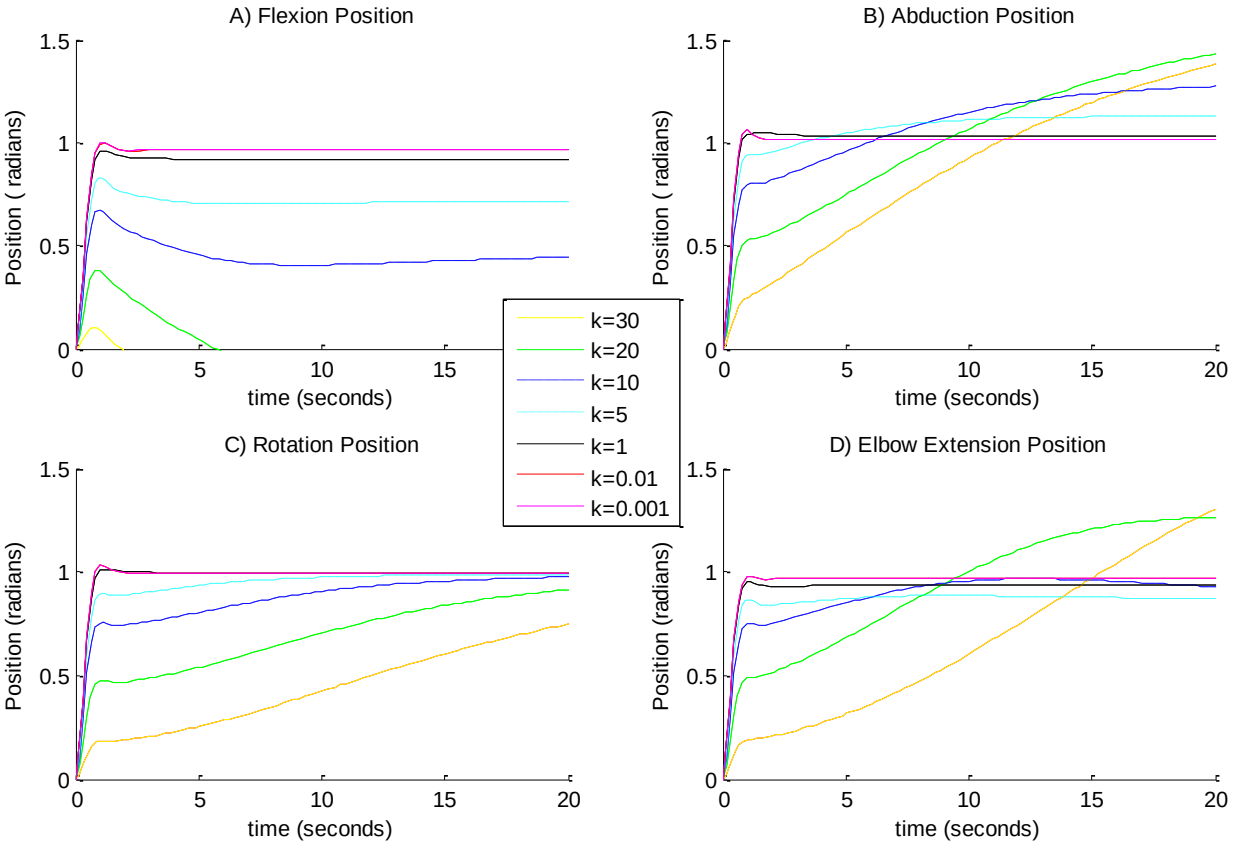

Figure 5.11 Position for (a) flexion, (b) abduction, (c) rotation, (d) elbow extension for switching controller with an epsilon value of zero and K values from 30 to 0.001. The best performance came from when the K value was the lowest. For the values higher then 1, the system took too long to settle or overshot the target value.

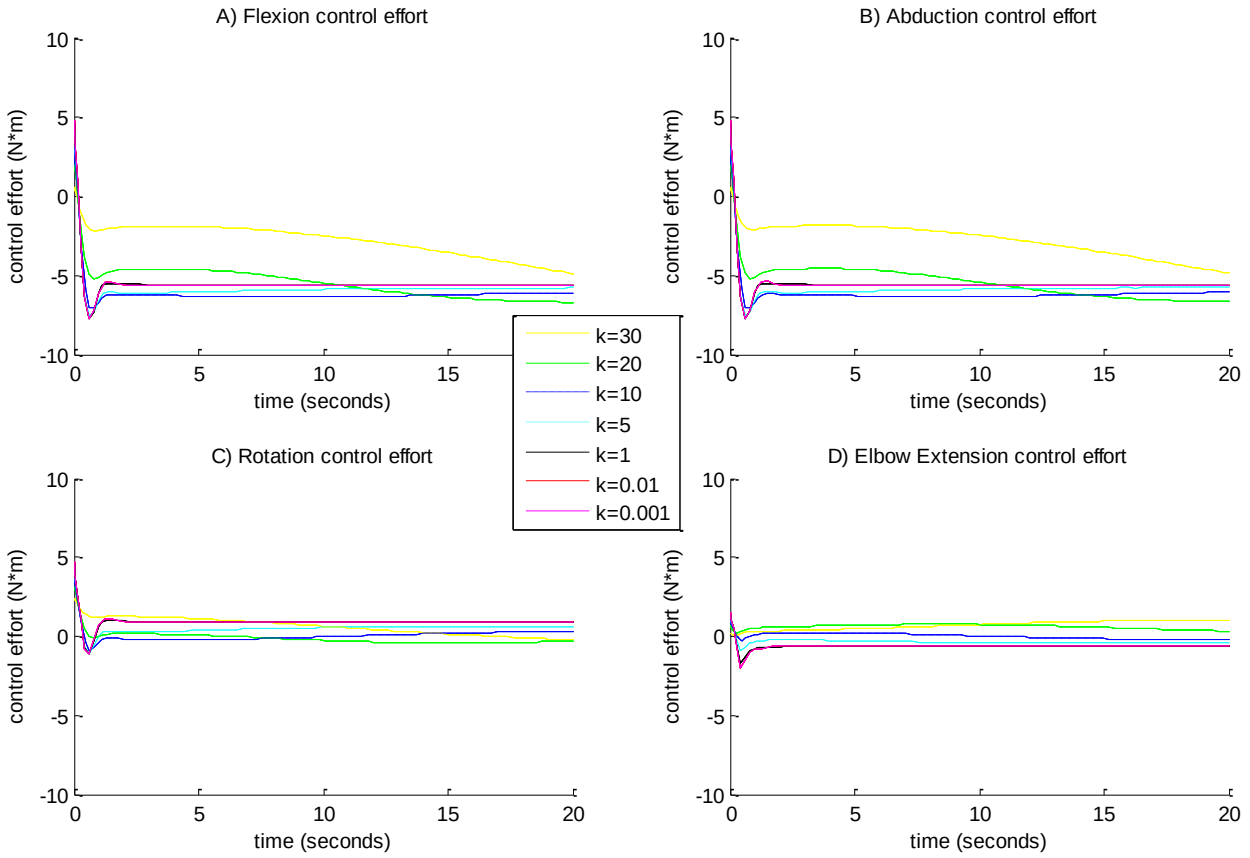

Figure 5.12 Control Effort for a) flexion, (b) abduction, (c) rotation, (d) elbow extension for switching controller with an epsilon value of zero and K values from 30 to 0.001. The least amount of control effort came when the system was using larger K values but the control effort meets the minimum specs of our motors so this is not a big issue.

The next logical step was to tune the epsilon value. After running the simulation from 100 to -100, there was no perceived effect from the epsilon value. Even with increasing the parameter error to 100, the system stayed static in terms of the various epsilon values that were utilized. A switching controller was created with values that make it close to ideal dynamic inversion. Since the system does not generate any chatter, there is no need for the smooth switching controller at this time. Once real world implementation occurs, tuning the epsilon value for the system will most likely be required.

Finally, the system was tested with a sinusoidal input to measure the performance overtime due to the fact that the system was given new points to track to continuously. With a 10% parameter error and a *k* value of .001 we experiences a continuous convergence of our system parameters.

The sin input for the four states had an amplitude of 1 and a frequency of 1 rad/s. The results are shown in Figure 5.13 a and b for position and control effort respectively. The control effort required for all are motors was less than the lowest continuous output generated from the stepper motor of the linear actuator.

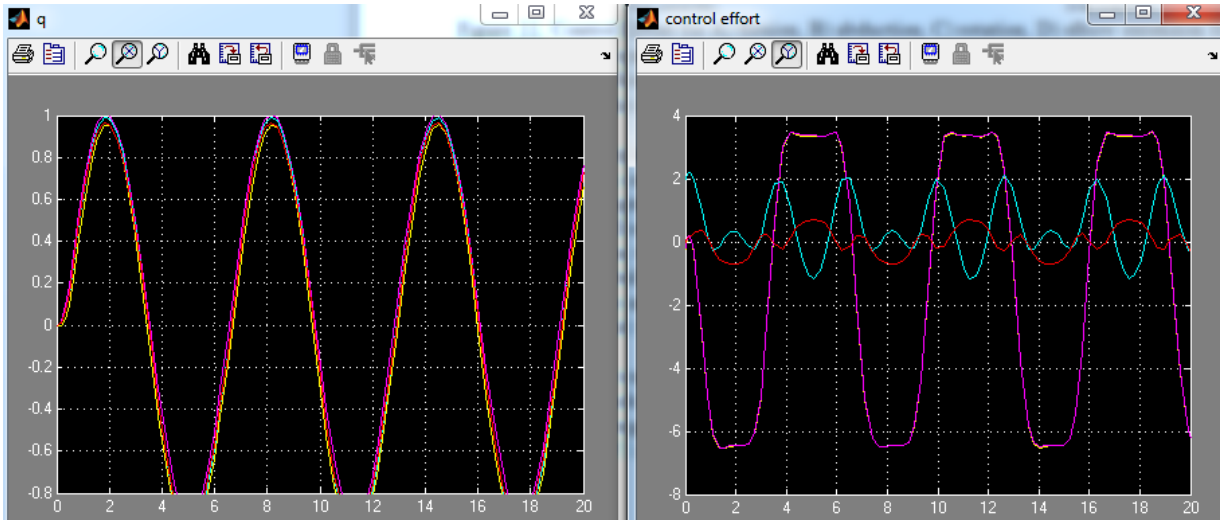

*Figure 5.13 (a) Error tracking of switching controller for a sin input of 1 with a frequency of 1 rad/s, and a 10% parameter error. The Flexion (yellow), Abduction (purple), Extension (blue), and Elbow Extension (red) all converge to the sin input. The minute deviation from 1 was due to the parameter error of 10% (b) The control effort of the system shows that the flexion and abduction motors (yellow and purple) take the most control effort which makes sense as they have to move the entire arm. The rotation of the shoulder takes less effort at 2 N*m and the elbow extension has the least amount of control effort at 1 N*m because it is the end effector. The reason that the control effort is not a mirror image around 0 is because the effects of gravity reduce some of the needed torque in certain positions.*

Results

After analyzing the different methods for controlling the system, it was observed that setting the epsilon value to 0 and *k* value to .001 gave excellent control of the system, even when applying a 10% parameter error on estimated masses and lengths. A sine input was used to visualize the effectiveness of the proposed system in tracking basic motion similar to near normal performance during implementation. In addition, the system maintained an acceptable control effort, requiring less than 5 N-m of control effort to accomplish all of the tracking and movement tasks. The motor with the lowest rated torque was the shoulder rotation, which has a maximum

continuous torque of 8.3 N-m, which is well above the simulated requirement. It should be noted that the linear actuator (dt) is limited to moving at 0.127 m/s, which would not match the simulated maximum speed used to move the linear actuator up to 1.5 meters. However, this is acceptable because the assumptions addressed the lack of motor dynamics and the expected range of motion for the linear actuator was on the order of inches rather than meters.

While the initial results of this research were acceptable, this control scheme will require further developments in order to be implemented on the robotic system. In particular, actuator dynamics for all stepper motors and linear actuators should be included, account for the dynamics and mass of a forearm being rotated by the linear actuator, and observe how the system reacts to inputs from tracking software, such as the Microsoft Kinect. Additional simulations are necessary for performance testing before implementation of the control scheme into the physical robot in the near future.

Implemented Controller

Hardware

The control of the upper body was divided into segments to help modularize the overall approach of controlling the system. The entire control was processed on the embedded PC running a LabVIEW VI. A diagram of the entire low level control can be seen in Figure 5.14. Each of the stepper motors in the chest was driven with a UIRobot CAN motor controller capable of outputting 4 amps to each motor. The linear actuator in the elbow was also driven with the same CAN motor controller. The measurements for the joint positions were taken by potentiometer values which were sampled by a Teensy 3.0 microcontroller at 96 Hz. The DC motor in the bicep was controlled with a Pololu High Voltage Simple Motor Controller. This controller had the ability to sample two analog inputs which were the potentiometer of the DC motor and linear actuator respectively. The information communicated between LabVIEW and the Simple Motor Controller was unreliable and a different approach had to be used. The analog measurements were re-routed to the chest and sampled with the same Teensy microcontroller that was responsible for the chest stepper motor

measurements. The modular approach was sacrificed for a more robust method of positional feedback. Each of the DC and stepper motors were powered by 24V supplied by the onboard power supply in the chest.

The hand had a Pololu 18ch Servo motor controller that was used for the motors in the forearm, wrist and hand. The joint measurements were done with bend sensors that were sampled via another Teensy 3.0 located in the palm. The servo motors were operating at 6V which was supplied by a step down converter that was sourced from the 24V power supply. LabVIEW 2011 was the main interface between each of the subcomponents and the teleoperation of the robot. An embedded PC on the robot was responsible for all the low level controls of the entire system.

Control of each of the stepper motors was driven by the network of the UIRobot CAN motor controllers. Each controller was capable of operating at 24V and 4amps to the stepper motors and was using a $1/8^{th}$ stepping resolution. Based on the resolution, the maximum operating speed was roughly 63,500 steps/s or 0.53 rad/s. A serial to CAN converter was used to relay the desired speed, position, number of steps and any other information to each of the controllers from the embedded PC. Each controller had a specific number that directs the communications to the desired motor. The system also had global variables for turning all the motors off simultaneously, if necessary.

The control of the steppers was done in a way that treats them like a DC motor. Each of the steppers sent an enable command when a new position was desired. Instead of receiving the number of steps necessary to move to the desired position, the control sends the error between the actual and desired values causing the motor to constantly step until the error was satisfied in a range of 10 microsteps. This allowed for constant control that was not dependent on the speed of built in stepper counter on the microcontroller.

Potentiometers were used to measure the joint position at each of the locations. The Bournus 10 k$\boldsymbol{\Omega}$ potentiometers send the absolute angle of each degree of freedom to the Teensy microcontroller in the chest which was then relayed to the embedded PC for direct processing. Interference was a main concern with the stepper motors and signal processing. Shielded cable was used to mitigate interference but did not fully correct the issue. Spikes in potentiometer data are still prevalent in the low level control of the system. The velocity of the controller was

proportional to the difference in the error so any spike in the desired vs. actual causes the motors to increase in velocity for a brief second before the controller compensates for the position. In order to rectify this issue, a threshold was checked to filter out the spikes in the actual data from the potentiometers.

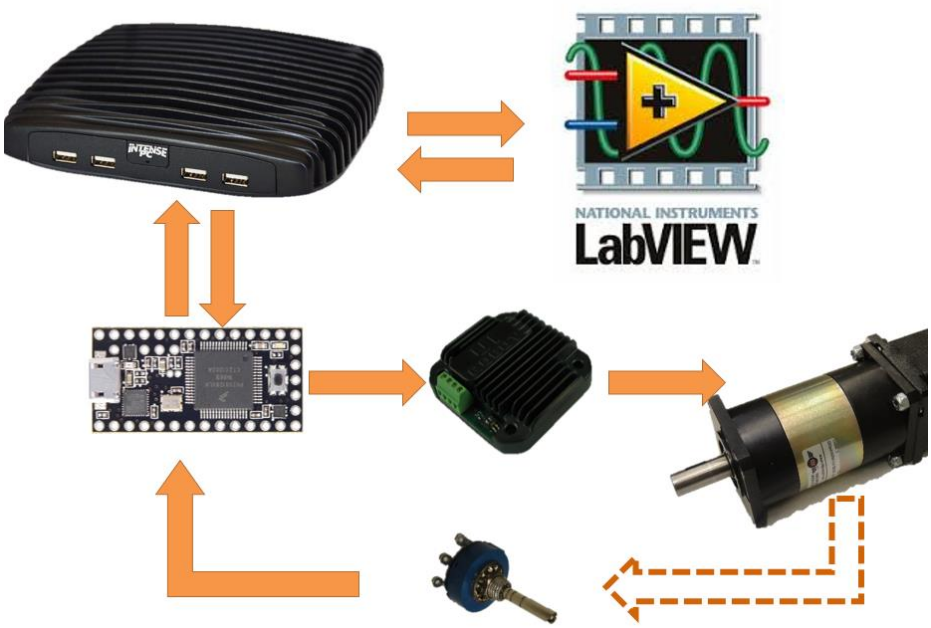

Figure 5.14 Low level control of system hardware. Labview running on the Intense PC was responsible for sending and receiving commands from the microcontrollers which communicate the desired positional commands to the motor drivers. The motors move at the desired velocity and position which was measured by the potentiometers that feed the information back to the microcontroller to complete the feedback loop.

Proportional Control

A proportional controller was implemented for each of the motors in the system to produce the desired controlled movements with the feedback loop provided from the potentiometers. Proportional gain values of 5 and 20 were used for the DC and Stepper motors respectively. The desired skeletal values from the Kinect were sent to the LabVIEW VI where it was compared to the actual position sensed by the potentiometer data from the microcontroller. The aggregate between these two data sets were compared to a threshold value. If the error was outside the range,

then the product of the error and proportional gain was sent to the velocity command in LabVIEW which is translated to the motor controller.

In order to make the controllers for the DC and Stepper motors more robust to errors, other limits were set inside the VI. For example, the desired position was set to a specific range that would not allow the motor to turn the arm into the body no matter what is the orientation. These limits effectively make the range of motion similar to the human range of motion described in Chapter 3. The velocity sent to the motor controller was also limited to a defined range. Issues arose when the controller received a value higher than 95% for the velocity scale, so the range was capped at 95% if the proportional gain multiplication exceeded this value. In case, the connection between the host and client computer is lost, a backup command will be sent to the motors to return them to the home position and then send a velocity = 0 command to the motor controllers.

The controllers can complete a desired range of motion in a reasonable time of 1.7 sec. The example shoulder rotation of the proportional controller is shown in Figure 5.15. The time being displayed is approximately 15.6 seconds. Between movements, the arm was held constant for 1 second before returning to the neutral position. Overall there is minimal overshoot in the controllers with consistent results for the motors of both DC and Stepper.

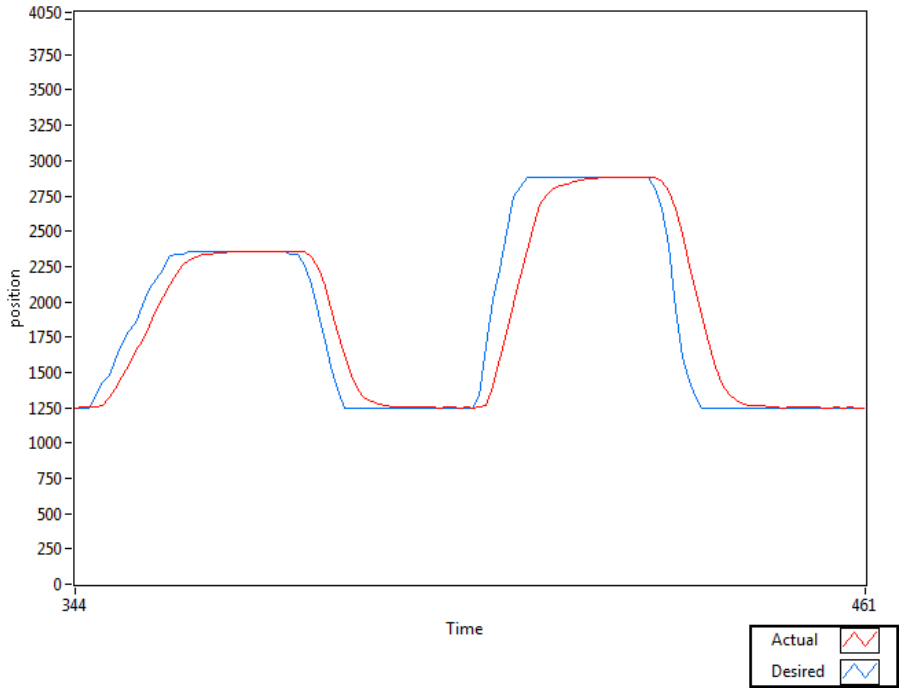

Figure 5.15 Positional graph with a time scale showing 15.6 seconds. The first desired position was set at 60° from the neutral location and the second desired position was set at 90°. Each position was held for one second before returning back to 0°. The blue line segment represents the desired position that is tracked by the Kinect and the red line segment represents the actual position being sensed by the potentiometer.

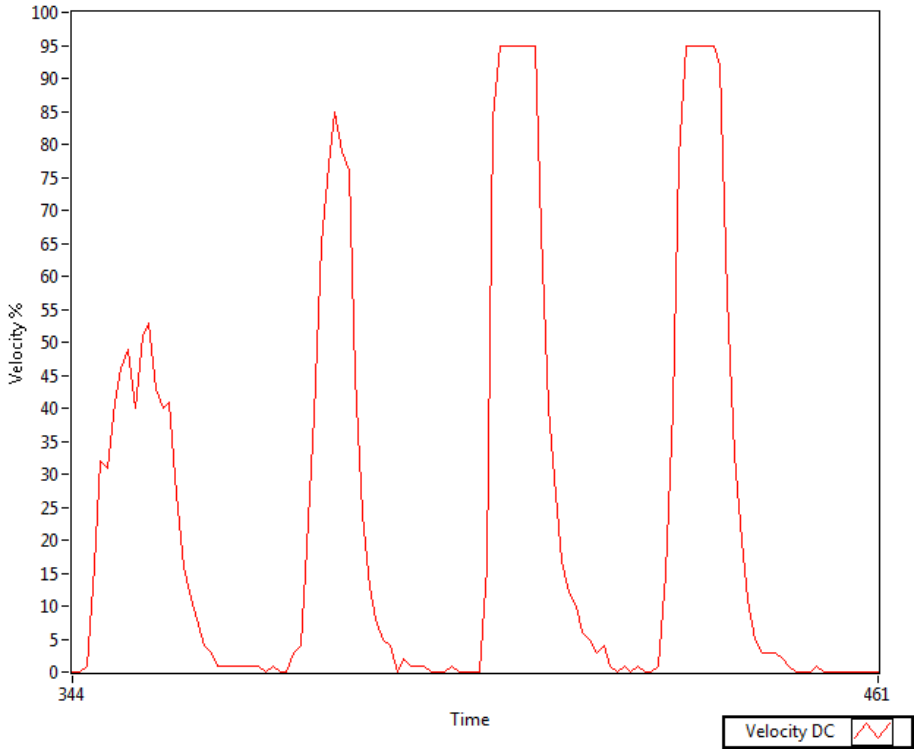

Figure 5.16 Velocity time graph showing the percentage change in velocity sent to the motor controller based on the proportional error shown in Figure 5.15. Notice how the spikes of the second movement are capped at 95% to avoid errors being sent to the motor controller.

LabVIEW interface

LabVIEW 2011 was the main interface used to network the skeletal data from the Kinect to the low level controls of the upper body. The Kinect was interfaced through a pre-built wrapper that allowed for the sampling of the 3D data points. These points were converted to vectors in order to find the relative angle between each link for the respective joint shown in Figure 5.17. The system outputs the angles as network shared variables which were sent to the embedded PC. The embedded PC running a separate VI takes these angles and converts them to a desired position

for each motion. The SISO low level operations take the desired position converted from the Kinect skeletal points and compare them to the actual position reported by the potentiometer sensors. The error between the actual and desired values is the exogenous input used to control the velocity of the stepper motors. The larger the error in the values, the faster the system responds to shift the actual to the desired position.

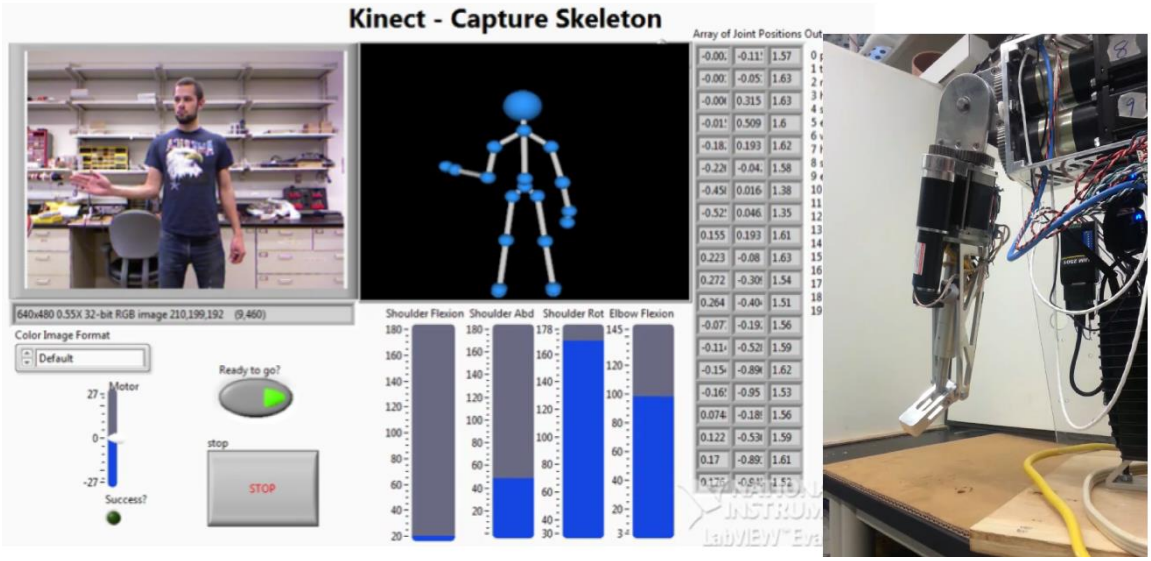

Figure 5.17 LabVIEW front panel VI of the Kinect capture system with respective joint angles shown in the blue bars and the actual position of the upper arm shown to the right.

Conclusion

Initial results for the setup with proportional control proved reliable as a SISO system, however much more work is necessary for implementing the theoretical nonlinear controller. The system was successfully proven to be teleoperated over the internet with a human virtually manipulating the joints of the robot with the Kinect skeletal points. The proportional controllers in the arm were tuned such that the motor for each joint has a fast response time with minimal overshoot in the system. Concatenating multiple motions will produce the nonlinear effects that will require the use of the switching controller as discussed earlier. Due to the method of controlling the stepper motor as a DC motor, modifications to the nonlinear switching controller will be necessary. Further testing will be necessary to validate the effectiveness of the nonlinear controller once implemented.

Chapter 6: Conclusion

Summary

The research investigated in this thesis lead to the development of technologies that can find use in teleoperative robotics for applications such as lab assistant and landmine clearance. The DASH Hand was inspired by biology providing the human-like form and function with 16 degrees of freedom. The hand design is unique because it is the first humanoid hand to feature intrinsic and extrinsic motors. Bend sensors were implemented in the joints for precise position control. The entire system was 3D printed to reduce the cost of manufacturing and simplify the maintenance. Each of the finger design was modular and can be easily replaced if necessary. The upper body was also inspired by human morphology and was designed to provide 3 degrees of freedom in the shoulder and one degree of freedom in the elbow. Positional sensors were located at the joint to provide direct feedback for each range of motion. Stepper motors were chosen for their low cost relative to DC motors and planetary gear heads were used to increase the torque to meet the requirement based on the design specifications of an IED disposal robot or laboratory assistant. Inherently there are backlash issues with using planetary gear heads and bevel gears which reduces the accuracy of the overall system to ±1.5° of resolution. Some of these issues were mitigated with tighter tolerance gear heads and software.

The controls of the system were evaluated in multiple iterations. The first test was focused on coordinating the Kinect skeletal points with a basic system. An exogenous input was used to control the experimental setup and proved to be efficient with a lag time of less than 0.25 s. Teleoperation of the system was accomplished with Wi-Fi 802.11n networking and shared variables to send the data from the host to client embedded PC. This increased the delay to approximately 0.5 seconds between the human that was tracked to the robot mimicking the movement and performing the desired dynamics. The Kinect was capable of tracking 20 joint positions of a human skeleton. The human was tracked with four depth points to produce the joint angles for flexion, abduction and rotation of the shoulder and elbow flexion. This allows for a direct user control over a robotic assistive upper body that was designed to be biomimetic in dimensions to a 6ft tall male. The cost of the system was much lower than other comparable robots

by a factor of at least 10. By utilizing off-the-shelf stepper motors, planetary gears and microcontrollers the system cost of the entire humanoid upper body including two DASH hands was in the range of $11,000. The breakdown of the cost is shown in Table 6.1 with each of the prices rounded to the nearest $100. This of course does not include the man hours required to fabricate the system nor the expenses normally attributed with bringing a system to market. Aside from these details the overall cost was an order of magnitude lower than the professional upper body systems currently on the market.

Product Description	Cost ($)
Stepper Motors with gearheads	$3,000
DC Motors with gearheads	$1,500
Hardware (material, metal, screws, bits, etc.)	$1,800
Embedded PC	$600
Kinect	$100
Microcontrollers and other electronic	$800
DASH Hand x 2 (material, motors, sensors, microcontrollers)	$3,000
Total	$10,700

Table 6.1 Cost breakdown of upper body design.

Recommendations

In future, robotic upper body system will be accessible to a wide variety of markets. As advances in microcontrollers, computers and controllers continue to occur, the price associated with these technologies will decrease. The major cost and limitation in design are the motors. Stepper motors were more cost-effective solution but in retrospect, using all DC brushed motors would have been more favorable. Low level control would have been smoother and the complexity

of communication between different motor drivers would have been reduced. Also, the electromagnetic interference issues would not have been problematic for the analog sensors.

Reducing the backlash in the gear systems would be another recommendation moving forward. A new design could be implemented for the flexion motion that would eliminate the coupling of the two stepper motors in the chest. Even though these issues were resolved within the controller of the system and by positional measurements in the joints instead of that at the motors, it might be of interest to develop a design that incorporated harmonic drives to reduce the backlash issues. This of course increases the price of the overall system and negates the anatomical geometry of the humanoid robot but would be more applicable for different applications that require the precision.

One of the major issues addressed with the entire system was using LabVIEW to communicate the commands between the low level electronics and the software controllers. The UIROBOT CAN converter, for example, causes multiple crashes when interfaced through LabVIEW. Investigation into the Robotic Operating System (ROS) is necessary for future applications. ROS provides open source software and multiple repositories of code that are currently being implemented on different systems including multi-DOF arm systems. The main advantages are the communication protocol along with vision and navigation packages. The learning curve is steep compared to LabVIEW but the robust communication protocol makes for a more reliable system.

Future work

The technologies developed in this thesis will be utilized in future designs iterations but some additional modifications will be necessary for better control and more robustness of the assistive humanoid upper body and DASH hands. Finger tracking was not available due to the limitations in the Kinect hardware. A separate system to track the position of the fingers is necessary to implement a full arm and hand control to grasp and manipulate objects. Pressure sensors at the finger tips are currently being investigated to give the user a sense of how much force is being applied to the objects being gripped by the hand. This will require redesign of the finger tips and additional coding to the microcontroller in the palm. The theoretical nonlinear

controller is currently being modified to operate on the upper body. Inverse kinematics are necessary to take the 3D points from the Kinect and build proper rotation angles in each of the relative frames to produce the desired MIMO system. The DASH hand will be integrated into the upper body via a new custom built slot joint for the elbow. Testing will be necessary for the new controller with regards to the full arm system being incorporated.

Bibliography

AIST. (2011, January). *Development of humanoid robot research and development platform for HRP-4 working.* Retrieved from National Institute of Advanced Industrial Science and Technology: http://www.aist.go.jp/aist_j/press_release/pr2010/pr20100915/pr20100915.html

Alexander, L. (2011, March 9). *Microsoft: Kinect Hits 10 Million Units, 10 Million Games* . Retrieved from gamasutra: http://www.gamasutra.com/view/news/33430/Microsoft_Kinect_Hits_10_Million_Units_10_Million_Games.php

Annear, S. (2013, April 24). *Waltham-Based Robotics Company Lends 'Arm' During Bomb Searches*. Retrieved from www.bostonmagazine.com/: http://www.bostonmagazine.com/news/blog/2013/04/24/qinetiq-waltham-robots-talon-marathon/

ANSolutions. (n.d.). *Standards & Feature Comparison*. Retrieved from Adaptive network solutions: http://www.an-solutions.de/images/standarts.html

APL. (2009, January). *DARPA Revolutionizing Prosthetics 2009 PowerPoint.* Retrieved from dtic.mil: http://www.dtic.mil/cgi-bin/GetTRDoc?Location=U2&doc=GetTRDoc.pdf&AD=ADA519193

ArmyMedical. (n.d.). *Range-of-motion exercises or the shoulder.* Retrieved from tpub.com: http://armymedical.tpub.com/MD0556/MD05560061.htm

AZOM. (2013). *AISI 1075 Carbon Steel (UNS G10750)*. Retrieved from Azom.com: http://www.azom.com/article.aspx?ArticleID=6559

BioDigital. (n.d.). *A Better Way to Understand Health and the Human Body*. Retrieved from BioDigital Human: Anatomy and Health Conditions in Interactive 3D: https://www.biodigitalhuman.com

Brooks, R. (n.d.). *Robots Everywhere!* Retrieved from The Computing Research Association: http://cra.org/ccc/docs/locslides/pdf/S4_Brooks.pdf

CARMODY, T. (2010, November 3). *How Motion Detection Works in Xbox Kinect*. Retrieved from Wired: http://www.wired.com/gadgetlab/2010/11/tonights-release-xbox-kinect-how-does-it-work/

Deyle, T. (2012, September 17). *Baxter Robot from Rethink Robotics Finally Unveiled!* Retrieved from www.hizook.com/: http://www.hizook.com/files/users/3/Baxter_Robot_from_RethinkRobotics_8.jpg

Engadget. (2013, March 17). *Live from Expand: Robopocalypse: Now with Willow Garage*. Retrieved from Viddler: Live from Expand: Robopocalypse: Now with Willow Garage

Garage, W. (2012). *Overview.* Retrieved from www.willowgarage.com: http://www.willowgarage.com/pages/pr2/overview

Guizzo, E. (2012, May 22). *How Robonaut's Compliant Arms Work*. Retrieved from Spectrum.ieee.org: http://spectrum.ieee.org/automaton/robotics/humanoids/how-robonaut-arms-work

H. Liu, K. Wu, P. Meusel, N. Seitz, G. Hirzinger. (2008). Multisensory Five-Finger Dexterous Hand: The DLR/HIT Hand II. *IEEE/RSJ International Conference on Intelligent Robots and Systems*, 3692-3697.

Hobby, S. (2012, August 15). *Lifelike, cost-effective robotic Sandia Hand can disable IEDs.* Retrieved from Sandia Labs News Releases: https://share.sandia.gov/news/resources/news_releases/robotic_hand/

IEEE. (2009). Telecommunications and information exchange between systems Local and metropolitan area networks: Wireless LAN Medium Access Control (MAC) and Physical Layer (PHY) Spec. *IEEE Standard for Information technology*.

Jordan Kuehn and Kevin Horecka. (n.d.). *LabVIEW Kinect Interface*. Retrieved from LabVIEW Hacker: http://www.labviewhacker.com/doku.php?id=projects:lv_kinect_interface:lv_kinect_interface

Kinea. (2009). *portfolio: DARPA Revolutionizing Prosthetics 2009.* Retrieved from Kineadesign.com: http://www.kineadesign.com/portfolio/prosthetics/

Landry, M. (2012, 9 18). *Rethink Robotics Revolutionizes Manufacturing with Humanoid Robot*. Retrieved from Rethink Robotics: http://www.rethinkrobotics.com/index.php/about/news-and-events/press-releases/rethink-robotics-revolutionizes-manufacturing-with-humanoid-robot/

Laura Inverarity, D. (2010, 11 12). *The Rotator Cuff*. Retrieved from physicaltherapy.about.com: http://physicaltherapy.about.com/od/humananatomy/p/RotatorCuff.htm

Loughran, H. (2011). Retrieved from www.aviano.af.mil: http://www.aviano.af.mil/shared/media/photodb/photos/070127-F-0000A-001.jpg

M.R. Cutkosky, R. H. (1990). Human grasp choice and robotic grasp analysis. In T. I. S.T. Venkatamaran, *Dextrous robot hands* (pp. 5-31). New York: Springer.

Magnuson, S. (2012, January). *Mini-Flail Robots Readied for Afghanistan Bomb Clearing Operations .* Retrieved from www.nationaldefensemagazine.org: http://www.nationaldefensemagazine.org/archive/2012/January/Pages/Mini-FlailRobotsReadiedforAfghanistanBombClearingOperations.aspx

Markus Grebenstein and Alin Albu-Schaffer. (2011). The DLR Hand Arm System. *IEEE International Conference on Robotics and Automation*, 3175-3182.

Meka. (2009, 10). *H2 Compliant Hand.* Retrieved from mekabot.com: http://mekabot.com/product_sheets/meka_H2_hand_product_sheet_10_2009.pdf

Microsoft. (n.d.). *Kinect Sensors*. Retrieved from Microsoft Developer Network: http://i.msdn.microsoft.com/dynimg/IC584396.png

NASA, J. (2000). *ANTHROPOMETRY AND BIOMECHANICS*. Retrieved from Man-System Integration Standards : http://msis.jsc.nasa.gov/sections/section03.htm

NI. (2012, March 4). *Using the LabVIEW Shared Variable*. Retrieved from National Instruments: http://www.ni.com/white-paper/4679/en

Priya, N. T. (2011). Design and implementation of a dexterous anthropomorphic robotic typing (DART) hand. *SMART MATERIALS AND STRUCTURES*, 1-12.

RBR. (2013, March 7). *DoD Places $27.3M Robot Order*. Retrieved from Robotics Business Review: http://www.roboticsbusinessreview.com/article/dod_places_27.3m_robot_order

RIA. (2013, 02 05). *North American Robotics Market Sets New Records in 2012*. Retrieved from Robotic Industries Association: http://www.robotics.org/content-detail.cfm/Industrial-Robotics-News/North-American-Robotics-Market-Sets-New-Records-in-2012/content_id/3906

RoborRealm. (2013). *Microsoft Kinect*. Retrieved from roborealm: http://www.roborealm.com/help/Microsoft_Kinect.php

Schmeder, A. (2008, August 08). *Optimizing the voltage divider pullup / pulldown circuit for resistive analog sensing.* Retrieved from http://cnmat.berkeley.edu/: http://cnmat.berkeley.edu/user/andy_schmeder/blog/2008/08/08/optimizing_voltage_divider_circuit_resistive_analog_sensing

Shadow. (2013, 01 01). *Shadow Dexterous Hand Technical Specification.* Retrieved from shadowrobot.com: http://www.shadowrobot.com/wp-content/uploads/shadow_dexterous_hand_technical_specification_E1_20130101.pdf

Shukla, M. (2012). Growth of Robotics Industry Early in 21st Century. *International Journal Of Computational Engineering Research (ijceronline.com) Vol. 2 Issue. 5*, 1554-1558.

Smith, T. (2011, 8 10). *Willow Garage Announces Availability of New PR2 Robot for $200,000*. Retrieved from Business Wire: http://www.businesswire.com/news/home/20110810006422/en/Willow-Garage-Announces-Availability-PR2-Robot-200000

T. Asfour, et al. (2006). ARMAR-III: An Integrated Humanoid Platform for. *IEEE*, 169-175.

Whitlock, C. (2011, Janurary 25). Number of U.S. casualties from roadside bombs in Afghanistan skyrocketed from 2009 to 2010. *The Washington Post*, p. 2.

Wikipedia. (2013, March 2). *Bombsuit*. Retrieved from Wikipedia, The Free Encyclopedia: http://en.wikipedia.org/wiki/Bombsuit

Winter, D. A. (1979). *Biomechanics of Human Movement.* New York: Wiley and Sons.